A Study of Photon Structure with Special Attention to the Low-x Region

J. Jason Ward

Department of Physics and Astronomy

University College London

Submitted for the degree of

Doctor of Philosophy

May 1996

Abstract

Singly–tagged two–photon collisions are studied in the OPAL detector at LEP using 45.9 pb^{-1} of data taken during the years 1990–1992 at and near a beam energy of 45.6 GeV. The energy and angle of the scattered electron or positron are measured by the OPAL Forward Detector, resulting in a Q^2 range of 4–30 GeV^2. The data distributions are compared with Monte Carlo distributions from F2GEN and HERWIG. Distributions of energy flow relative to the tag demonstrate that F2GEN and HERWIG do not model the hadronic final state well. Unfolded results for the photon structure function $F_2^\gamma(x)$ on a $\log_{10} x$ scale are presented for two Q^2 ranges, with mean values of 6.4 GeV^2 and 15.1 GeV^2. The measurement of $F_2^\gamma(x)$ is shown to be dominated by systematic errors in the low-x region.

Acknowledgements

First and foremost I would like to thank David Miller for his supervision and support throughout this work. I am indebted to Bruce Kennedy and Mark Lehto who both helped to get me going with the analysis.

The OPAL Collaboration are gratefully acknowledged for their hard work in building and running the detector which provides the data for this thesis. Special thanks to Jim Conboy, Allan Skillman, Ed McKigney, Tony Rooke, Joerg Bechtluft, Bernd Wilkens, Steve Hillier, Richard Nisius, Volker Blobel and Peter Hobson who have all been fine collaborators. My understanding of the theory of two–photon physics is much better after discussions with Jeff Forshaw, and Mike Seymour has been excellent with answering my HERWIG questions.

Thanks to David Munday, Tara Shears, Bill Allison and Guy Pooley, who all helped me when I was applying to various places to do a Ph.D. – all of the support and encouragement that I got made a big difference.

For financial support I would like to thank the Particle Physics and Astronomy Research Council and University College London. Also the University of London's award of the 1994 Valerie Myerscough Prize made a trip to a NATO Advanced Study Institute possible.

During the Ph.D., and because of it, I was fortunate enough to become involved in two new activities that have shown ways towards having a quiet mind. A bow to Dennis Ngo for being an excellent teacher of Tai' Chi (Suan Yang of the Tiger–Crane combination) and an enormous thankyou to Paul Phillips and Christine Beeston for getting me into mountain walking.

Special thanks to Jan Lauber, Warren Matthews, Mark Lehto (again!), Mark Pearce, Kwasi Ametewee, Nick Feast, Harvey Maycock, Katrijn Raaijmakers and Philippe Persiaux, who have all provided alot of support on various occasions.

Finally, thanks to my parents, Margaret and John Ward, and my sisters, Hayley and Michelle Ward, for their continuing Love and support.

This thesis is dedicated to all of the people named above. It could not have been produced without them.

Jason Ward

May 1996

Contents

List of Figures

List of Tables

Chapter 1

Introduction

This thesis is a study of singly–tagged two–photon collisions using data from the OPAL (Omni–Purpose Apparatus for LEP) detector [1] at the LEP (Large Electron–Positron) collider [2] at CERN near Geneva. The aim of such a study is to obtain a measurement of the hadronic photon structure function, $F_2^\gamma(x, Q^2)$.

The data used in this analysis were taken in the years 1990–1992 and correspond to 45.93 pb^{-1} of $\mathrm{e}^+\mathrm{e}^-$ integrated luminosity.

As an introduction it is acknowledged that the photon has a hadronic structure. A simple picture for this structure is presented, followed by the method used to study this structure at an $\mathrm{e}^+\mathrm{e}^-$ collider. The photon structure function is then introduced and the motivation for measuring it is given.

Chapter 2 is a theoretical presentation of the photon structure function. An outline of the OPAL detector follows, in Chapter 3, and an account of the selection of singly–tagged two–photon events is given in Chapter 4. The Monte Carlo simulation in this analysis is described in Chapter 5 and a comparison of Monte Carlo with data is presented in Chapter 6. In Chapter 7, the unfolding procedure is described and tested. The data are then unfolded. Chapter 8 is the summary and conclusion to this thesis.

1.1 Two-Photon Interactions

In classical electrodynamics the photon is described by the linear Maxwell equations. However, in quantum mechanics, the photon is not a photon all of the time. A photon of energy E_γ can fluctuate into a virtual state of a charged particle pair, by the uncertainty principle. If m_{pair} is the mass of the charged particle pair, then the lifetime of the state is given by

$$\Delta t \simeq \frac{2E_\gamma}{m_{pair}^2} \tag{1.1}$$

assuming $m_{pair}^2 \ll E_\gamma^2$ and $\hbar = c = 1$. This time increases as the photon energy increases. Therefore, an interaction of two photons becomes possible because one photon can interact with one of the charged particles in the state the other photon has fluctuated into.

1.2 The Photon Picture

The virtual state of the charged particle pair can be either a charged lepton-antilepton pair (l^+l^-), a quark-antiquark pair ($q\overline{q}$) or a massive pair (e.g. W^+W^-). A cut-off parameter p_0 may be introduced to separate the range of $\gamma \to q\overline{q}$ fluctuations into low- and high-virtuality states. Such a separation is necessary because the low-virtuality state is in the regime of non-perturbative QCD physics. The vector meson dominance (VMD) model approximates the range of $\gamma \to q\overline{q}$ fluctuations below p_0 by a sum over low–mass vector meson states. Each meson state can be written as $|V\rangle$. p_0 sets the minimum transverse momentum of the $q\overline{q}$ pair in the high-virtuality perturbative part of $\gamma \to q\overline{q}$ fluctuations (the so–called 'point–like' component). This state can be written as $|q\overline{q}\rangle$. The complete photon wave-function for low–mass states [3] is then

$$|\gamma\rangle = c_{bare}|\gamma_{bare}\rangle + \sum_{V=\rho^0,\omega,\phi\ldots} c_V|V\rangle + \sum_q c_q|q\overline{q}\rangle + \sum_l c_l|l^+l^-\rangle. \tag{1.2}$$

1.3 The eγ Vertex

By the uncertainty principle an electron of energy E_b can fluctuate into a virtual electron-photon state. This is illustrated in the top vertex of Figure 1.1. If the electron is scattered with energy E_1' into a solid angle element $d\Omega$, at angle θ_1 to the initial electron direction, after producing a photon of energy zE_b then the flux for such a process is given by [4]

$$\Gamma_t(z, Q^2) = \frac{\alpha_{em}}{2\pi^2} \frac{E_1'}{Q^2} \frac{1 + (1-z)^2}{z} \,. \tag{1.3}$$

α_{em} is the electromagnetic coupling constant and Q^2, which is by definition the negative of the four-momentum squared of the photon, is given by

$$Q^2 \equiv -q^2 \simeq 4E_b E_1' \sin^2\left(\frac{\theta_1}{2}\right) \tag{1.4}$$

where the mass of the electron has been neglected. It should be noted that the above flux factor peaks at small values of Q^2 and small photon energies.

1.4 $\gamma\gamma$ Collisions at an e$^+$e$^-$ Collider

The only way of studying photon structure at current e$^+$e$^-$ colliders is to use an eγ vertex from one electron (positron) to produce a nearly-real photon that will display the structure described in Section 1.2. A second photon of high virtuality from the eγ vertex of the opposing positron (electron) can be used to probe the structure of the nearly-real photon. The multi-peripheral two-photon process is illustrated in Figure 1.1. It is customary to label the four-vector of the virtual probe photon as q and the four-vector of the nearly-real photon as p. The invariant kinematic variables

$$x = \frac{Q^2}{2p \cdot q} = \frac{Q^2}{Q^2 + P^2 + W^2} \tag{1.5}$$

and

$$y = \frac{p \cdot q}{p \cdot p_1} \tag{1.6}$$

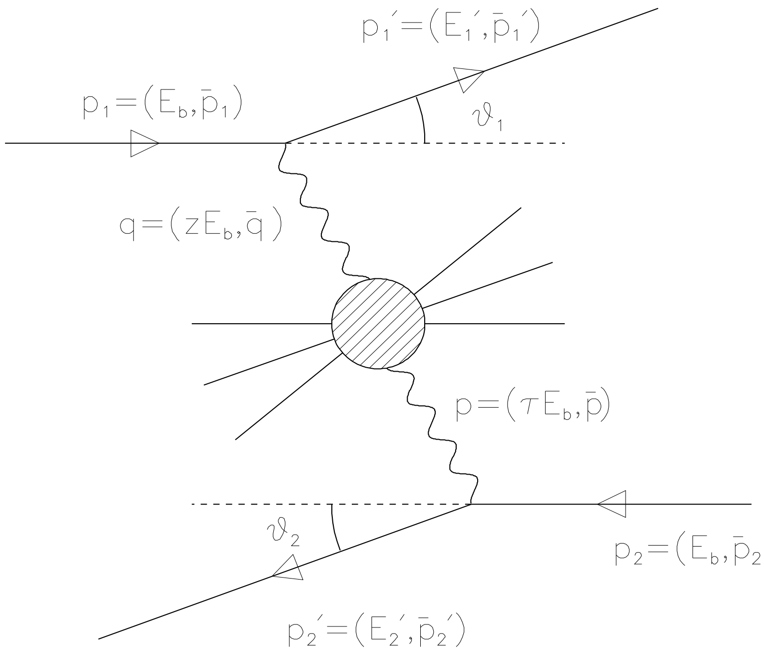

Figure 1.1: The multi-peripheral two-photon process labelled with four–vectors. z and τ are the energies of the probing and probed photon respectively, expressed as a fraction of the beam energy.

can be defined with reference to the four-vectors in Figure 1.1. W is the invariant mass of the two-photon system. Two–photon collisions where one photon is virtual and one is real will be called '$\gamma^*\gamma$ collisions'. The * marks the highly virtual photon.

1.5 Deep Inelastic eγ Scattering

When $Q^2 \gg 4$ GeV^2 and $P^2 \simeq 0$ the two-photon collision can be regarded as deep-inelastic electron-photon scattering, where the bare probe photon couples to a quark inside the nearly-real photon resulting in an hadronic final state. Experimentally, deep inelastic eγ scattering is observed with singly-tagged events, where the probe photon has its Q^2 determined from the energy (E_1') and angle (θ_1) of the scattered electron (called the 'tag') and $P^2 \simeq 0$ is ensured by requiring that the positron is not seen in the detector (called the 'anti-tag' condition). Therefore, from now on, E_1' and θ_1 will be called E_{tag} and θ_{tag} respectively.

In the single–tag regime, Equation 1.5 simplifies to

$$x = \frac{Q^2}{Q^2 + W^2} \tag{1.7}$$

and x, called 'Bjorken x' or 'x_{Bj}' to differentiate it from the Feynman x variable, can be interpreted as the fraction of the four–momentum of the nearly-real photon carried by the struck quark. From the anti–tag condition, the nearly-real photon is approximately collinear with the beam ($p \cdot p_1 \simeq 2E_b^2\tau$ where τ is the energy of the probed photon as a fraction of the beam energy) and

$$y = 1 - \frac{E_{tag}}{E_b}\cos^2\left(\frac{\theta_{tag}}{2}\right). \tag{1.8}$$

Total Differential Cross–Section

The amplitude for $e^+e^- \to e^+e^- X$ shown in Figure 1.1 can be written as

$$T = \frac{e^2}{q^2p^2}\, j_\mu\, j_\alpha\, R^{\mu\alpha}. \tag{1.9}$$

The j's are the electromagnetic currents of the leptons. The $R^{\mu\alpha}$ term relates to the coupling of the two photons to the final state X. For leptonic final states the cross–section can be obtained from Equation 1.9 by an exact QED calculation. The cross–section for a hadronic final state cannot be calculated so exactly because it involves the theory of QCD which is not as predictively powerful as QED.

The photons radiated from the incoming leptons are in either a transverse (T) or longitudinal (L) polarisation state. The total differential cross–section will therefore contain four sub cross–sections σ_{TT}, σ_{LT}, σ_{TL}, σ_{LL} and two interference terms, τ_{TT} and τ_{TL}. The subscripts refer to the polarisations of the first and second photon respectively. The total differential cross–section for unpolarised lepton beams is [5]

$$\begin{aligned}\frac{d\sigma}{d\Gamma} &= L_{TT}\left\{\sigma_{TT} + \epsilon_1\ \sigma_{LT} + \epsilon_2\ \sigma_{TL} + \epsilon_1\epsilon_2\ \sigma_{LL}\right.\\ &\left. + \frac{1}{2}\epsilon_1\epsilon_2\ \tau_{TT}\ \ \cos 2\phi\ + 2\sqrt{\epsilon_1(1+\epsilon_1)}\sqrt{\epsilon_2(1+\epsilon_2)}\ \tau_{TL}\ \ \cos\phi\right\}, \quad (1.10)\end{aligned}$$

where

$$d\Gamma = \frac{dp_1' dp_2'}{E_1' E_2'}. \quad (1.11)$$

which uses the variables defined in Figure 1.1. ϕ is the angle between the scattering planes of the electron and positron in the $\gamma\gamma$ centre–of–mass frame. The terms L_{TT}, ϵ_1 and ϵ_2 are calculable in QED. The interference terms vanish after integration over ϕ. In the limit when the second photon is real ($P^2 = -p^2 = 0$) the only cross–section terms to survive are σ_{TT} and σ_{LT}. One can now relate these terms to the usual construction of the cross–section in terms of structure functions.

Structure Functions

The transverse and longitudinal photon structure functions are defined as

$$F_T^\gamma(x, Q^2) = \frac{Q^2}{4\pi^2\alpha_{em}}\ \frac{1}{2x}\ \sigma_{TT} \quad (1.12)$$

and

$$F_L^\gamma(x, Q^2) = \frac{Q^2}{4\pi^2\alpha_{em}}\sigma_{LT}. \quad (1.13)$$

The more commonly used structure functions are $F_1^\gamma(x,Q^2)$ and $F_2^\gamma(x,Q^2)$ which are defined as

$$F_1^\gamma(x,Q^2) = F_T^\gamma(x,Q^2) \tag{1.14}$$

and

$$F_2^\gamma(x,Q^2) = 2xF_T^\gamma(x,Q^2) + F_L^\gamma(x,Q^2). \tag{1.15}$$

The eγ cross-section can now be written as

$$\frac{d\sigma_{e\gamma}}{dxdy} = \frac{16\pi\alpha_{em}^2 E_b^2 \tau}{Q^4}\left[(1-y)F_2^\gamma(x,Q^2) + xy^2 F_1^\gamma(x,Q^2)\right]. \tag{1.16}$$

Events are strongly peaked towards small tag angles and high tag energies, as was discussed in Section 1.3. Therefore y is small (see Equation 1.8) and $y^2 \ll (1-y)$. It can be seen from Equations 1.15 and 1.12 that $F_2^\gamma(x,Q^2) > xF_1^\gamma(x,Q^2)$ so that $(1-y)F_2^\gamma(x,Q^2) \gg xy^2F_1^\gamma(x,Q^2)$ and

$$\frac{d\sigma_{e\gamma}}{dxdy} \simeq \frac{16\pi\alpha_{em}^2 E_b^2 \tau}{Q^4}(1-y)F_2^\gamma(x,Q^2). \tag{1.17}$$

The structure functions defined above can either be QED structure functions, from reactions of the type $\gamma\gamma \to l^+l^-$, or hadronic structure functions from reactions of the type $\gamma\gamma \to$ hadrons . The muonic $F_2^\gamma(x,Q^2)$ has been measured by OPAL [6], CELLO [7] and DELPHI [8]. All of these measurements agree well with QED predictions. This work is only concerned with the *hadronic* photon structure function.

1.6 Interest in F_2^γ

The theory behind the photon structure function will be given in more detail in Chapter 2. To motivate the measurement of the hadronic photon structure function, its interesting features are summarised below.

High Q^2

As a consequence of the running coupling constant in QCD, F_2^γ rises linearly with $\log Q^2$ in leading order of α_s. The slope of this rise is predicted by QCD. Looking for this behaviour in F_2^γ is therefore a test of perturbative QCD. If the coupling constant is frozen at an initial value of Q^2 then F_2^γ bends asymptotically to a constant that is independent of Q^2 [9]. This is illustrated in Figure 1.2, which has been adapted from [10]. The difference between a fixed coupling and a running coupling becomes greater at larger Q^2 .

Low Q^2

The evolution of the photon structure function from $Q^2 \simeq 1$ GeV^2 to $Q^2 \simeq 5$ GeV^2 is not well understood. There is no apparent need for a point–like component of F_2^γ for Q^2 smaller than ~ 1 GeV^2, but the transition between the hadronic shape and the point–like shape of F_2^γ appears to be complete at $Q^2 \simeq 5$ GeV^2. This transition region contains a significant non–perturbative component and is therefore difficult to calculate. Some theorists argue that one can start evolving F_2^γ from Q^2 values of less than 1 GeV^2 [11, 12] and correctly predict F_2^γ for Q^2 > 5 GeV^2. Others argue that this is not possible [13]. Some data do exist, but there is controversy on the validity of this data. Clearly, new measurements in this region are valuable.

Low x

Photon and proton structure function models based on the BFKL equation [14, 15] predict that $F_2(x)$ rises approximately as $x^{-\frac{1}{2}}$ for $x < 0.1$. This is not a unique prediction since the DGLAP [16, 17, 18, 19, 20] evolution of parton distributions (eg GRV [11]) predicts a similar rise. The process that might be associated with such a rise is illustrated in Figure 1.3. The fact that the *proton* structure function has been observed to rise as x decreases [21, 22] (see Figure 1.4) adds weight to the question of whether or not the hadronic photon structure function does the same. This is unknown because photon structure function data do not extend to as low an x as proton structure function data, due to the kinematical differences between electron–photon and electron–proton deep inelastic scattering experiments.

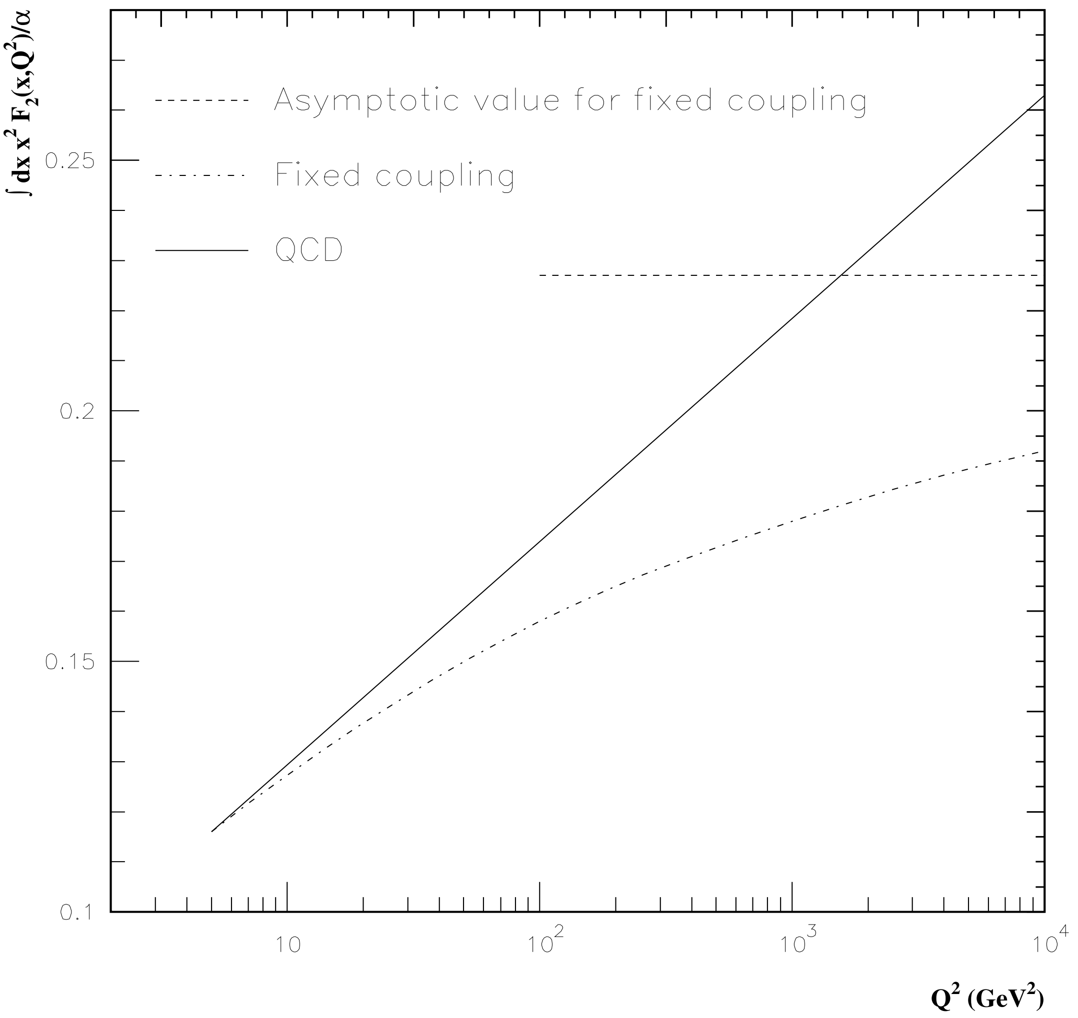

Figure 1.2: Comparison of Q^2 evolution of the second moment of F_2^γ in QCD (solid line) with a theory in which the coupling constant is frozen at an initial value of $Q_0^2 = 5\ \mathrm{GeV}^2$ (dot–dashed line).

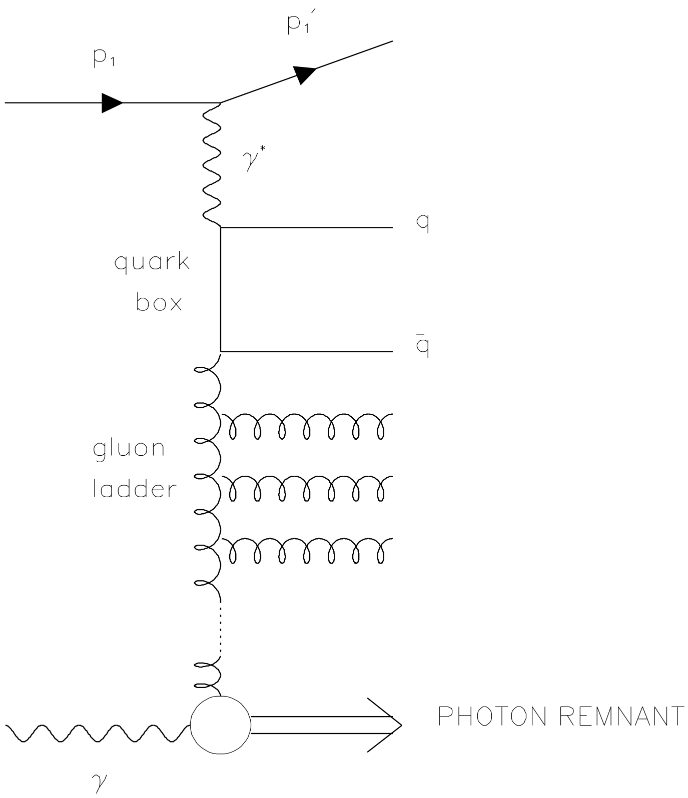

Figure 1.3: Feynman diagram used in some QCD models of the low–x part of the photon structure function.

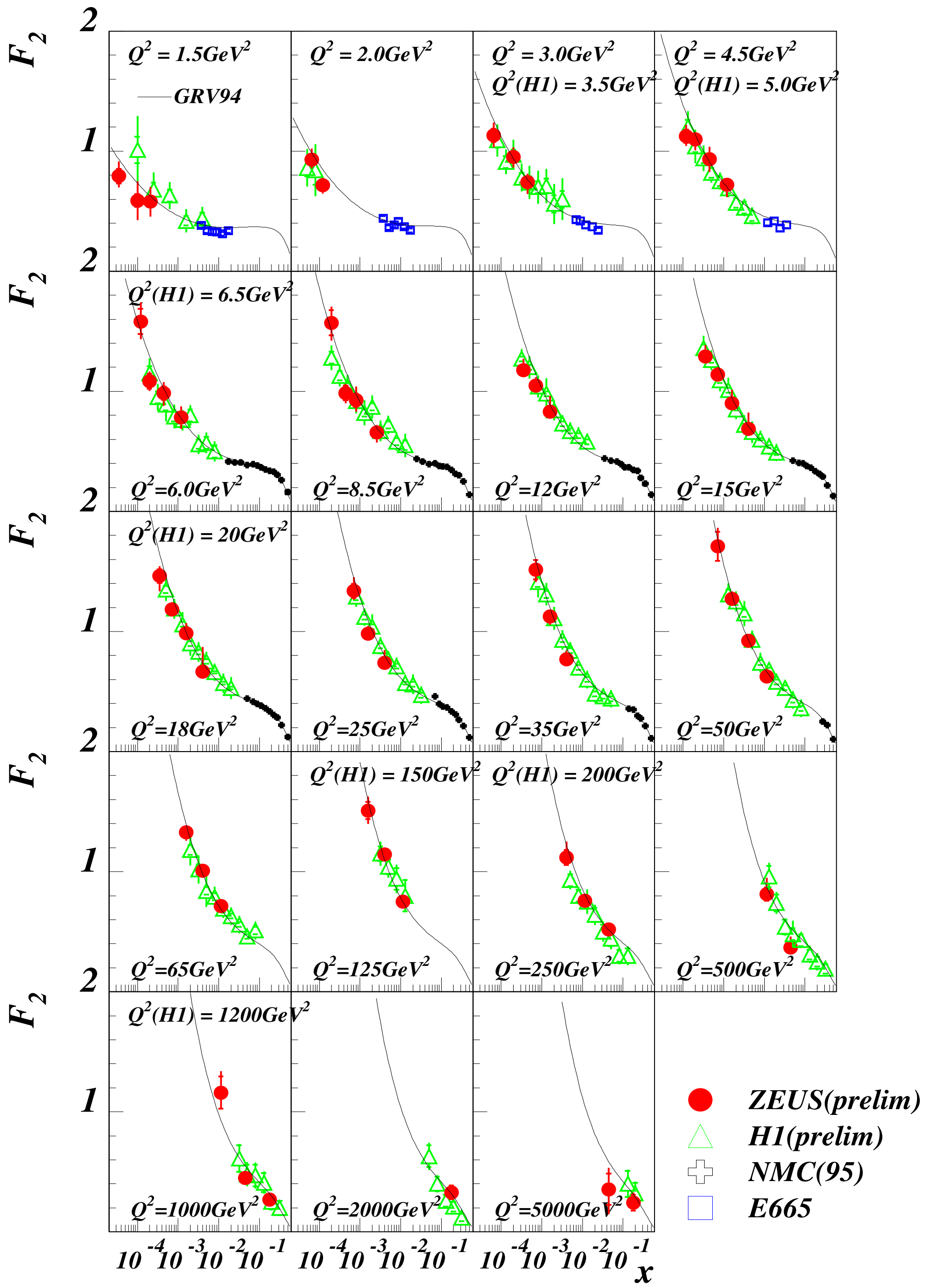

Figure 1.4: Rise in the proton structure function measured by the ZEUS Collaboration (circles) and the H1 Collaboration (triangles).

1.7 F_2^γ Measurements at LEP

As the beam energy of an e^+e^- collider increases, greater values of W can be reached, so the minimum value of x for a given Q^2 decreases (see Equation 1.7). Although the event rate for a given tagging range would decrease with increasing beam energy, the accessible Q^2 values within that tagging range increases (see Equations 1.3 and 1.4).

Table 1.1 shows mean Q^2 values and x–ranges of singly–tagged hadronic two–

Collider	Coll.	$\langle Q^2 \rangle$(GeV^2) (and Q^2 range)	x–range (and No. bins)	Ref.
PETRA	PLUTO	2.4 (1.5–3)	0.016–0.700 (3)	[24]
		4.3 (3–6)	0.03–0.80 (3)	[24]
		9.2 (6–16)	0.06–0.90 (3)	[24]
		5.3 (1.5–16)	0.035–0.840 (6)	[24]
		45.0 (10–100)	0.1–0.9 (4)	[25]
	TASSO	23.0 (7–70)	0.02–0.98 (5)	[26]
	JADE	24.0 (10–55)	0.10–0.90 (4)	[27]
		100.0 (30–220)	0.1–0.9 (3)	[27]
PEP	TPC/2γ	0.7 (0.5–1.0)	(4)	[28]
		1.3 (1.0–1.6)	(4)	[28]
		5.1 (4–7)	0.02–0.74 (3)	[28]
		20.0	0.196–0.963 (3)	[29]
TRISTAN	AMY	73.0 (30.0–110.0)	0.125–0.875 (3)	[30]
	TOPAZ	5.1 (3–10)	0.010–0.20 (2)	[31]
		16.0 (10–30)	0.20–0.78 (3)	[31]
		80.0 (45–130)	0.06–0.98 (3)	[31]
	VENUS	40.0 (20–75)	0.09–0.81 (4)	[32]
		90.0 (45–240)	0.19–0.91 (4)	[32]
LEP	OPAL	5.9 (4–8)	0.001–0.649 (3)	[33, 34]
		14.7 (8–30)	0.006–0.836 (4)	[33, 34, 35]
	DELPHI	12.0 (4–30)	0.001–0.847 (4)	[36]
			0.001–0.350 (3)	[36]

Table 1.1: Published hadronic F_2^γ data as a function of x.

photon events at various e^+e^- centre–of–mass energies. LEP1, having a beam energy of 45.6 GeV, can clearly access the interesting high Q^2 and low-x regions that lower energy experiments cannot reach. LEP2 ($E_{beam} \simeq 90$ GeV) and a future linear e^+e^- collider ($E_{beam} = 250$ GeV) will achieve even lower-x and higher Q^2 values [23].

An x–Q^2 kinematic plot of Monte Carlo tagged two–photon events at LEP1 is shown in Figure 1.5. It clearly shows the effect of certain necessary cuts, such as minimum $\gamma\gamma$ mass, minimum tag energy and minimum tag angle, on the distribution of events.

It will become clear in the next chapter that there are theoretical uncertainties in the low-x behaviour of the photon structure function. Since a measurement of F_2^γ at LEP extends to lower x than any previous F_2^γ measurement, this thesis concentrates on the low-x region.

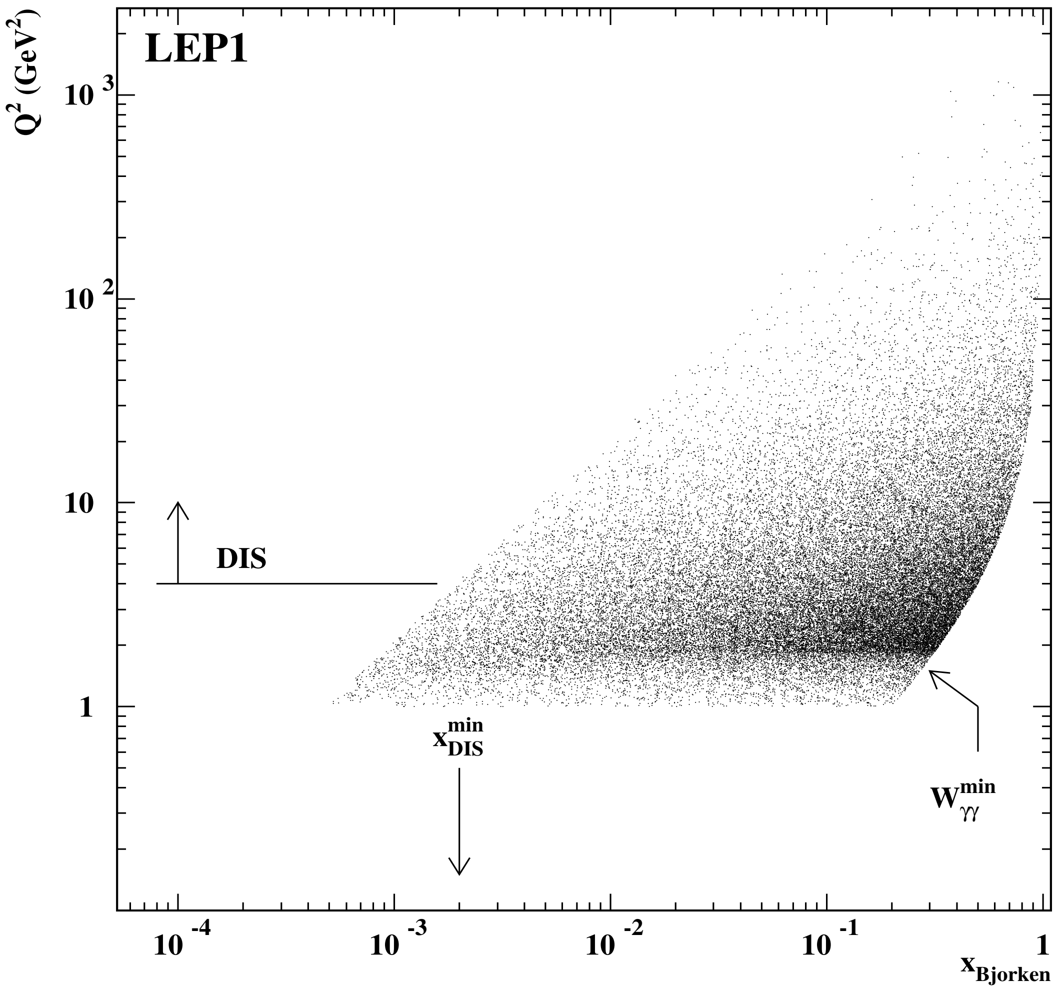

Figure 1.5: Scatter plot of Monte Carlo tagged two–photon events from the F2GEN generator (see Section 5.3) at $E_{beam} = 45.6$ GeV. The minimum $\gamma\gamma$ mass is 2 GeV, the minimum tag angle is 30 mrad and the minimum tag energy is 20 GeV. The photonic parton distribution functions from GRV (see Section 2.7.1) have been used in the event generation.

Chapter 2

Theory of the Photon Structure Function

This chapter begins by considering how F_2^γ can be constructed from parton distribution functions. Various forms of these distributions will be presented. The determination of the hadronic and point-like components of F_2^γ , using Vector Meson Dominance (VMD), the Quark Parton Model (QPM) and quantum-chromodynamics (QCD) calculations will then be discussed. Both DGLAP and BFKL evolution are considered. The charm quark contribution to F_2^γ is considered, followed by a review of all of the available F_2^γ parameterisations and models.

2.1 Parton Distributions of the Photon

In the introduction the photon structure function was presented as part of the $e\gamma$ cross-section, which is related to the multi-peripheral $e^+e^- \rightarrow e^+e^-$ + hadrons cross-section by a simple flux-factor. We know, however, that the photon sometimes consists of partons, so it is natural to consider F_2^γ as a sum of distributions of partons in the photon. This is central to the theory that follows. In Leading Order (LO),

$$F_2^\gamma(x,Q^2) = x\sum_{i=1}^{n_f} e_i^2\left[q_i^\gamma(x,Q^2) + \overline{q}_i^\gamma(x,Q^2)\right]. \tag{2.1}$$

The $q_i^\gamma(x,Q^2) = \overline{q}_i^\gamma(x,Q^2)$ condition is assumed to hold and so Equation 2.1 simplifies to

$$F_2^\gamma(x,Q^2) = 2x\sum_{i=1}^{n_f} e_i^2 q_i^\gamma(x,Q^2). \tag{2.2}$$

It is often more convenient to work with the singlet and non-singlet quark distributions, $q_S^\gamma(x,Q^2)$ and $q_{NS}^\gamma(x,Q^2)$ respectively. These are the quark distributions that are used to determine F_2^γ parameterisations (see Section 2.7).

$$q_S^\gamma(x,Q^2) = 2\sum_{i=1}^{n_f} q_i^\gamma \tag{2.3}$$

$$q_{NS}^\gamma(x,Q^2) = 2\sum_{i=1}^{n_f}\left[e_i^2 - \langle e^2\rangle\right] q_i^\gamma \tag{2.4}$$

where

$$\langle e^k\rangle \equiv \frac{1}{n_f}\sum_{i=1}^{n_f} e_i^k. \tag{2.5}$$

The construction of F_2^γ in next-to-leading order (NLO) [37, 11] from the photonic parton distribution functions is more complicated. It involves the gluon distribution, $g^\gamma(x,Q^2)$, of the photon, unlike the LO case.

2.2 The Components of F_2^γ

It is usual to separate the photon structure function into a hadronic and a point-like part

$$F_2^\gamma(x,Q^2) = F_2^{PL}(x,Q^2) + F_2^{HAD}(x,Q^2). \tag{2.6}$$

Such a division is well supported by the experimental data (see e.g. TASSO [38]). The hadronic part, which is assumed to be approximated by VMD, appears to be dominant at low–x and low Q^2 . The point-like component, which is most simply described by the QPM, plays a more important part for approximately $x \geq 0.1$ and $Q^2 \geq 4$ GeV^2 . VMD and the QPM are discussed in the next two sections.

2.3 Vector Meson Dominance

Photons are known to behave like hadrons when interacting with other hadrons [39]. In the Vector Meson Dominance (VMD) picture, at low 4–momentum–squared transfers, the interaction of a photon with hadrons is dominated by the exchange of vector mesons which have the same quantum numbers as the photon. Therefore, the hadronic part of F_2^γ is usually chosen according to VMD. The photon couples to the vector mesons ρ, ω, ϕ and J/ψ resulting in

$$F_2^{HAD} = F_2^{VMD} = \sum_V \left(\frac{4\pi\alpha_{em}}{f_V^2}\right) F_2^V \tag{2.7}$$

where $f_V^2/4\pi$ are determined from data to be 2.20 for ρ^0, 23.6 for ω, 18.4 for ϕ and 11.5 for J/ψ [39]. f_V from Equation 2.7 is related to c_V from Equation 1.2 by $c_V^2 = 4\pi\alpha_{em}/f_V^2$. This hadronic part is completely analogous to hadron behaviour, as there is no increase with log Q^2 (it exhibits Bjorken scaling) and the x-shape is not calculable in perturbation theory.

The parton distributions in the ρ meson are experimentally unknown, so it is assumed that the ρ distributions are the same as those in the pion. The pion structure function for approximately $x \geq 0.2$ is known from experimental results from the Drell-Yan [40] production of μ-pairs in pion-nucleon scattering.

The simplest VMD estimate [5, 9] that can be derived from pion structure function measurements is

$$F_2^{VMD} = 0.2\ \alpha_{em}(1-x). \tag{2.8}$$

One might alternatively construct the photonic parton distributions as

$$f^\gamma(x,\mu^2) = \kappa \left(\frac{4\pi\alpha_{em}}{f_\rho^2}\right) f_\pi(x,\mu^2) \tag{2.9}$$

where $f^\gamma = q^\gamma(=\overline{q}^\gamma)$ or g^γ, $1 \leq \kappa \leq 2$ and μ^2 is a very low resolution scale (~ 0.3 GeV^2). The κ parameter is introduced [5] to deal with theoretical ambiguities, especially higher order gluonic corrections.

Alternatively, one can fit to the low–Q^2 data. TPC/2γ fitted their data at $Q^2 =$ 1GeV^2 [28] with

$$F_2^{VMD}(x) = \alpha A x^a (1-x)^{0.95} + B(1-x)^b \tag{2.10}$$

and obtained $A = 0.22$, $B = 0.06$, $a = 0.31$ and $b = 2.5$. This is illustrated on a linear-x scale in Figure 2.1, with the simple VMD estimate of Equation 2.8, and on a $\log_{10} x$ scale in Figure 2.2.

2.4 The Quark Parton Model

Before QCD was developed, attempts at trying to determine the properties of F_2^γ and F_L^γ came from calculations based on the free quark-parton model and light-cone algebra. In the quark-parton model (QPM) the structure functions are calculated by treating the quarks as free particles without strong interactions. In the limit of light quark masses ($m_i^2/Q^2 \ll 1$) the structure functions can be written [41, 42]

$$\begin{aligned} F_2^{QPM}(x, Q^2, P^2, m_i^2) &= \frac{3\alpha}{\pi}\sum_{i=1}^{n_f} e_i^4 \; x\left[(x^2+(1-x)^2)\log\left(\frac{Q^2(\frac{1-x}{x})}{(m_i^2+P^2x(1-x))}\right)\right. \\ &\left. - 2(1-3x+3x^2) + \frac{m_i^2(1+2x-2x^2)}{(m_i^2-P^2(x^2-x))}\right], \end{aligned} \tag{2.11}$$

$$F_L^{QPM}(x, Q^2, P^2, m_i^2) = \frac{12\alpha}{\pi}\sum_{i=1}^{n_f} e_i^4 \; x^2(1-x). \tag{2.12}$$

When $P^2 = 0$, Equation 2.11 reduces to the P^2 independent formula

$$\begin{aligned} F_2^{QPM}(x, Q^2, m_i^2) &= \frac{3\alpha}{\pi}\sum_{i=1}^{n_f} e_i^4 \; x\left[(x^2+(1-x)^2)\log\left(\frac{Q^2}{m_i^2}\left(\frac{1-x}{x}\right)\right)\right. \\ &\left. + 8x(1-x) - 1\right]. \end{aligned} \tag{2.13}$$

The presence of the $\log Q^2$ term in Equation 2.13 breaks the scaling of F_2^{QPM}, but F_L^{QPM} is scale invariant. This P^2 independent formula is illustrated in Figure 2.1. One should note that the x and Q^2 behaviour of the QPM is rather different from that of the VMD model. The quark-parton model is not a complete model for a description of F_2^γ because we know that quarks are not free objects. They can couple to gluons. To improve the calculation of F_2^γ quantum chromodynamics must be used.

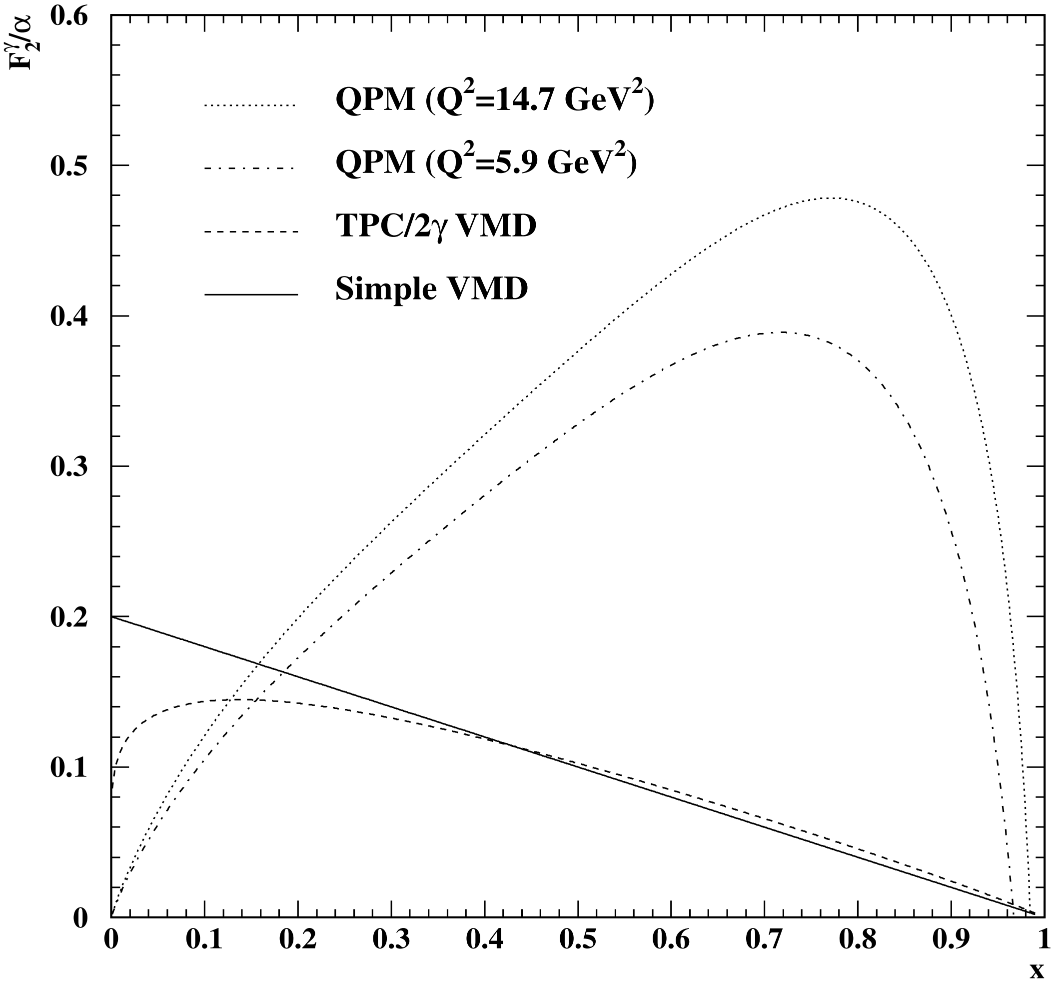

Figure 2.1: QPM and VMD predictions for F_2^γ . The simple VMD and TPC/2γ VMD predictions are from Equations 2.8 and 2.10 respectively. The QPM prediction (Equation 2.13) are for 3 flavours, with $m_u = m_d = m_s = 300$ MeV.

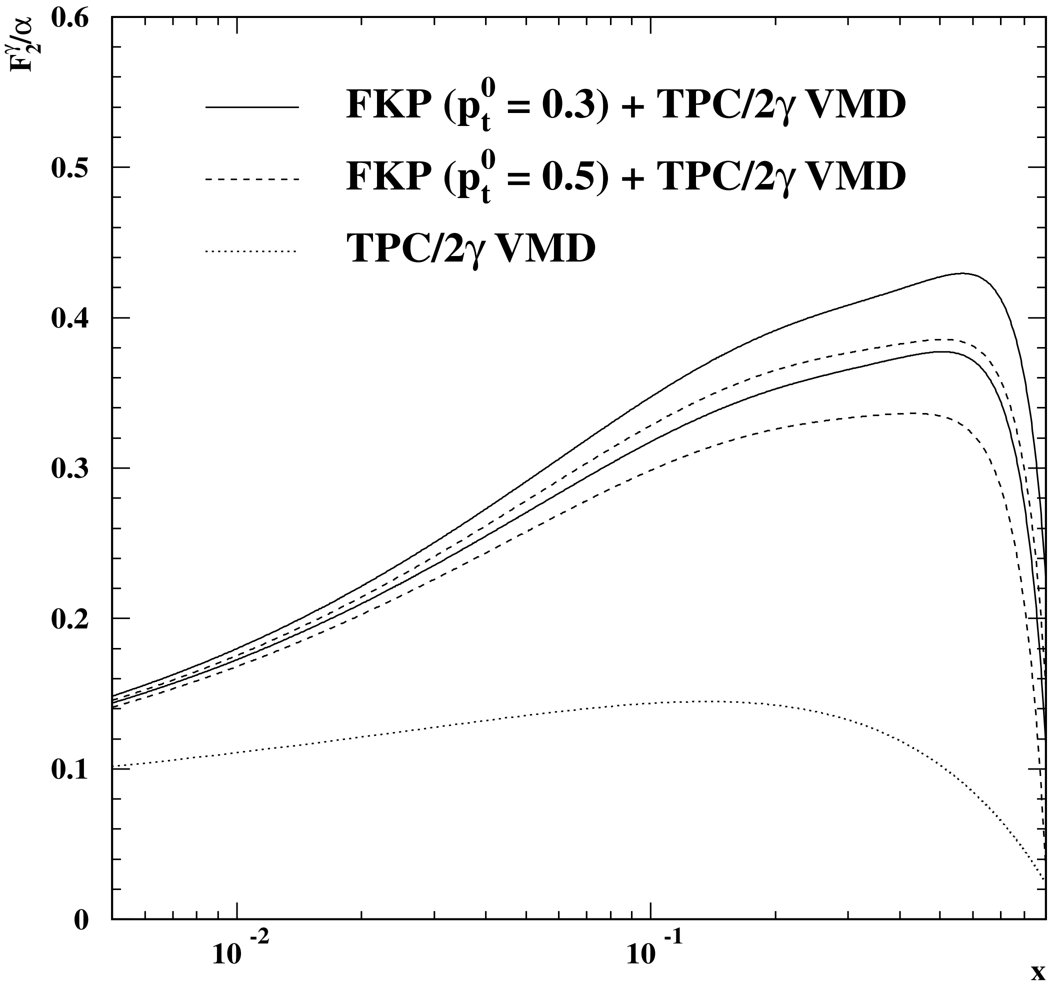

Figure 2.2: The TPC/2γ VMD prediction is shown by the dotted line. The solid lines represent the FKP(p_t^0 = 0.3 GeV)+VMD curves for Q^2=5.9 GeV^2 (lower solid line) and Q^2=14.7 GeV^2 (upper solid line). The dashed lines represent the FKP(p_t^0 = 0.5 GeV)+VMD curves for Q^2=5.9 GeV^2 (lower dashed line) and Q^2=14.7 GeV^2 (upper dashed line).

2.5 QCD Calculations

Quarks can radiate gluons and gluons can produce quark–antiquark pairs, so the QPM calculation must be modified. If a valence quark (one of the quarks from the $\gamma \to q\overline{q}$ vertex) is struck and it has not radiated a gluon then the kinematics of the hard scattering are not affected. When one or more gluons are radiated from the valence quark, they carry away some of the four–momentum from that quark. If the valence quark is still struck it will then be seen to have a smaller four–momentum than it had initially. If a sea quark (one of the quarks from a gluon $\to q\overline{q}$ vertex) has been struck it will be seen to have a smaller four–momentum than the gluon it was produced from.

QCD predictions for F_2^γ can take several different approaches. One can proceed by using the operator product expansion and renormalisation group equations (OPE–RGE) [43, 44], evolution equations [45] or Feynman diagrams in the leading log approximation [46, 47, 48, 49].

2.5.1 The DGLAP Evolution Equations

The cross–section for the hard scattering process will depend on the scale Q^2 of the virtual probe photon and on the momentum fraction distribution, $D(x, Q^2)$, of the partons in the real photon at this scale. The evolution equation for the parton density $D(x, t)$ may be written as

$$t\frac{\partial}{\partial t}D(x,t) = \frac{\alpha_s}{2\pi}\; P(x) \otimes D(x,t). \tag{2.14}$$

The convolution integral is defined as

$$a(x) \otimes b(x) = \int_x^1 \frac{dy}{y} a\left(\frac{x}{y}\right) b(y). \tag{2.15}$$

t is equal to (minus) the virtual mass–squared of the parton after the branching and $P(x)$ is the relevant parton splitting function. Equation 2.14 is called the Dokshitzer–Gribov–Lipatov–Altarelli–Parisi (DGLAP) equation [16, 17, 18, 19, 20]. $D(x, t)$ represents the distribution of parton momentum fractions inside the incoming hadron probed at scale t. When there are several different types of partons in the branching process, Equation 2.14 has to be generalised to a coupled set of evolution equations of the form

$$t\frac{\partial}{\partial t}D_i(x,t) = \frac{\alpha_s}{2\pi}\sum_j P_{ij}(x) \otimes D_j(x,t). \tag{2.16}$$

The parton splitting functions $P_{ij}(x)$ have the physical interpretation, to first order in α_s, of being the probability of finding parton i in a parton j with a fraction x of the momentum of the parent parton. The lowest order approximation to the splitting functions [16] are

$$\begin{aligned}
P_{qq}(z) &= C_F\left[\frac{1+z^2}{(1-z)_+} + \frac{3}{2}\delta(1-z)\right] \\
P_{qg}(z) &= C_F\left[z^2 + (1-z)^2\right] \\
P_{gq}(z) &= T_R\left[\frac{1+(1-z)^2}{z}\right] \\
P_{gg}(z,n_f) &= 2C_A\left[\frac{z}{(1-z)_+} + \frac{(1-z)}{z} + z(1-z)\right] + \frac{1}{6}\left(11C_A - 4n_fT_R\right)\delta(1-z)
\end{aligned} \tag{2.17}$$

where $C_F = 4/3$, $T_R = 1/2$ and $C_A = 3$. The plus prescription on the singular parts of these splitting functions is defined under the integral sign as

$$\int_0^1 dx\ f(x)\ [g(x)]_+ \ = \int_0^1 dx\ \left(f(x) - f(1)\right)g(x). \tag{2.18}$$

This removes the singularity of the integrand in the evolution equations at $z = 1$, corresponding to the emission of a soft gluon. The remaining singularities at $z = 0$ are outside the range of the integration, so all of the integrals are finite.

2.5.2 Parton Distributions at Low-x

The HERA data [21, 22] show that the proton structure function increases as $x \to 0$, implying that the sea quark distribution grows rapidly with decreasing x. For the parameterisations of the parton distributions at low Q^2 , an increase in the sea quark density is driven by the much larger and increasing gluon density at small x ($P_{gg}(z) \sim 6/z$ as $z \to 0$). For the $\gamma^*\gamma$ low-x region, one would expect the gluon ladder diagram, illustrated in Figure 1.3, to be the dominant process.

The DGLAP equations are derived keeping only the leading log terms in Q^2. The $\log(1/x)$ terms are neglected. In the $x \to 0$ limit the $\log(1/x)$ terms become important. One can still use the DGLAP evolution equations for low-x, provided $\log Q^2 \gg \log(1/x)$. The treatment of the low-x region corresponds to a resummation of terms proportional to $\alpha_s \log Q^2$ to all orders in perturbation theory. Considering the gluon distribution only, $G(x,t)$, such a scenario yields [50]

$$G(x,t) \sim exp\sqrt{\frac{4C_A}{\pi b}\log\frac{\log(t/\Lambda^2)}{\log(t_0/\Lambda^2)}\log\frac{1}{x}} \tag{2.19}$$

where

$$b = \frac{11C_A - 2n_f}{12\pi}. \tag{2.20}$$

However, the Q^2 values may not be large (especially at low-x), so it is more useful to resum terms proportional to $\alpha_s \log(1/x)$ to all orders. This is done by the Balitsky–Fadin–Kuraev–Lipatov (BFKL) equation [14, 15]. A simple derivation of the BFKL equation and the low-x behaviour is given by Mueller [51]. Mueller actually calculates the low-x behaviour of the wave function of a hadron rather than in terms of structure functions. The inclusive gluon distribution g at small-x in a quarkonium wave function is

$$g(x,b^2) \propto bx^{-\lambda} \tag{2.21}$$

where $\lambda = 4 \log 2\, N\alpha_s/\pi$. N is the number of colours. The λ number is about 0.5 for $\alpha_s \simeq 0.2$, leading to an approximate $x^{-1/2}$ divergence at low-x. The parameter b is related to the scale Q^2 by a Fourier transformation.

2.6 Charm–Quark Contributions

It is important to consider how the charm quark contribution to F_2^γ can be theoretically dealt with, since it cannot be incorporated into the massless DGLAP equations in the moderate Q^2 region ($Q^2 \leq 100$ GeV^2). This is, however, the region with the most data. The effect of quark mass is accounted for by using the massive quark DGLAP equations [52] or even more accurately by incorporating the full next–to–leading order corrections [53]. It has been found [54] that a good approximation to the charm quark contribution to the photon structure function for $Q^2 \leq 100$ GeV^2 is made by summing the contributions from the QPM processes of $\gamma^*\gamma \to c\bar{c}$ (direct) and $\gamma^* g \to c\bar{c}$ (resolved).

Direct QPM process

Since the QPM direct process is commonly used when including charm in F_2^γ parameterisations (see Section 2.7), it is briefly described. It is calculated via the lowest order Bethe–Heitler process [55, 56] and is given by

$$F_{2,c}^{\gamma}(x, Q^2)|_{direct} = 3\frac{\alpha}{\pi} e_c^4 \; w\left(x, \frac{m_c^2}{Q^2}\right) \tag{2.22}$$

where e_c=2/3 is the charm–quark electric charge and

$$\begin{aligned} w(z,r) &= z\,[\beta\{-1+8z(1-z)-4rz(1-z)\} \\ &\quad +\{z^2+(1-z)^2+4rz(1-3z)-8r^2z^2\}\log\frac{1+\beta}{1-\beta}\Big] \end{aligned} \tag{2.23}$$

with

$$\beta = \sqrt{1-\frac{4rz}{(1-z)}}. \tag{2.24}$$

The charm contribution is added for $\beta > 0$ ($W^2 > 4m_c^2$) and is zero for $\beta < 0$ ($W^2 < 4m_c^2$), and therefore incorporates the charm mass threshold. The effect of adding in this charm contribution to $F_2^\gamma(x)$ is visible in Figure 2.3.

Resolved QPM process

The expression for the QPM contribution to F_2^γ from the resolved process $\gamma^* g \to c\bar{c}$ is given by [54]

$$F_{2,c}^{\gamma}(x, Q^2)|_{resolved} = \frac{\alpha_s(Q^2)}{2\pi} e_c^2 \int_{ax}^{1} dy \; w\left(\frac{x}{y}, \frac{m_c^2}{Q^2}\right) g(y, Q^2), \tag{2.25}$$

where $a = 1 + 4m_c^2/Q^2$ and the gluon distribution $g(x, Q^2)$ is given by solving the massless $n_f = 3$ DGLAP equations.

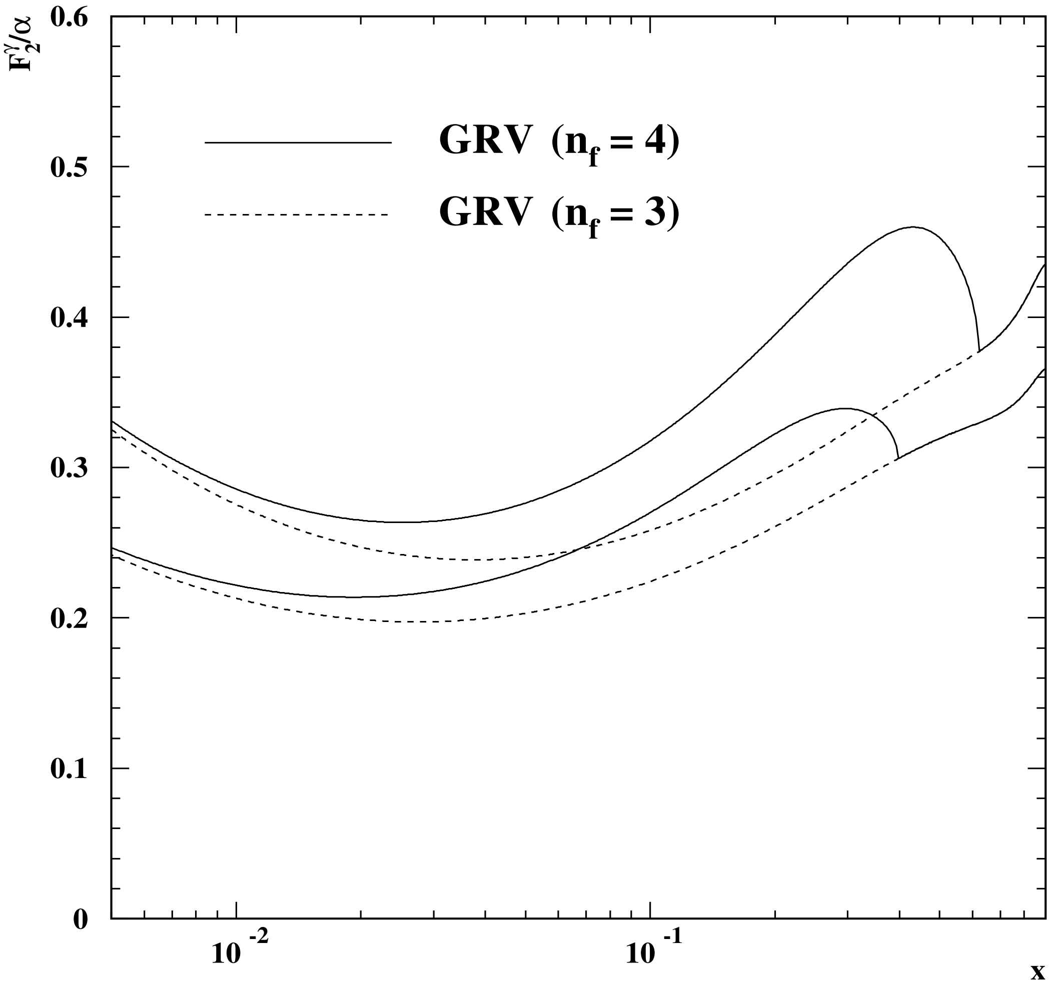

Figure 2.3: The GRV Leading Order parameterisation for four flavours (solid lines) and three flavours (dashed lines). The lower curve of each pair is calculated at Q^2=5.9 GeV^2 and the upper curve of each pair is calculated at Q^2=14.7 GeV^2.

2.7 F_2^γ Parameterisations and Models

The formulation of the DGLAP equations is convenient for obtaining analytical solutions [54] for the Q^2 *evolution* of parton distributions. No prediction is made for the size and shape of the functions themselves. A common method of making a theoretical prediction of the photon structure function is to choose a reference scale Q_0^2 , parameterise the parton distributions at that scale and then evolve those distributions numerically using the DGLAP equations. $F_2^\gamma(x, Q^2)$ can then be constructed at a given Q^2 and a global numerical fit to the data performed to determine the best values for parameters.

This section presents some of the basic features of the available theoretical predictions of F_2^γ .

2.7.1 Glück, Reya and Vogt (GRV)

These authors have produced parton distributions of the proton [57] and the pion [58] that have been generated from a valence–like structure at a common, very low resolution scale. The deep–inelastic scattering data have been reproduced, in particular the HERA results on F_2^p [21, 22] are in excellent agreement with the GRV prediction. This success provides motivation for using a low starting scale in the case of the photon.

The GRV photonic parton distributions [11] are in LO and NLO (DIS_γ factorisation scheme). The evolution starts at $Q_0^2 = 0.25$ GeV^2 (LO) and $Q_0^2 = 0.3$ GeV^2 (NLO). The photonic input distributions are purely from VMD. They are taken to be those from Equation 2.9, with $xf_\pi(x, \mu^2) \sim x^a(1-x)^b$ being the valence–like (i.e. $a > 0$) inputs from [58] and [5]. Only one parameter, κ, is left to be fixed from a least squares fit to the F_2^γ data [24, 25, 26, 27, 28, 30]. The best κ values were found to be $\kappa_{LO} = 2$ and $\kappa_{NLO} = 1.6$, with good agreement of the resulting parameterisations with the data.

The charm contribution has been calculated by the direct QPM process, with $m_c = 1.5$ GeV. The controversial [59] low–Q^2 large–x TPC/2γ data points [28], which are close to the resonance region, were not used in the determination of κ.

This parameterisation is used to generate some of the Monte Carlo samples used in this thesis (see Chapter 5). The three and four flavour parameterisations are illustrated in Figure 2.3 for two different Q^2 values.

2.7.2 Hagiwara et al. (WHIT)

These are a set of six LO photonic parton distributions (WHIT1 to WHIT6) [54] which have systematically different gluon contents. The evolution starts at $Q_0^2 =$ 4 GeV^2. The F_2^γ data [24, 25, 26, 27, 28, 29, 30, 31, 32, 34] at $4 \leq Q^2 \leq 100$ GeV^2 are fitted to determine the free parameters. Not all of the experimental data points are used. Firstly, the data at $\langle Q^2 \rangle$ lower than 4 GeV^2 are omited. Secondly, bins are accepted only if

$$x_{lower\ bin\ edge} > \frac{\langle Q^2 \rangle}{\langle Q^2 \rangle + (W_{vis}^{max})^2}, \tag{2.26}$$

where W_{vis}^{max} is the experimental cut on the visible invariant mass of the hadronic final state. This is on the grounds that the bins that fail this condition might suffer from large systematic uncertainties in the unfolding procedure (see Chapter 7).

The charm quark contributions to F_2^γ are calculated by the QPM (with $m_c =$ 1.5 GeV) at $Q^2 \leq 100$ GeV^2, with contributions from both the direct and resolved processes (see Section 2.6).

2.7.3 Gordon and Storrow (GS)

These are LO and NLO ($\overline{MS}$ factorisation scheme) parameterisations [37]. The evolution starts at $Q_0^2 = 5.3$ GeV^2, which is the average of the low-Q^2 PLUTO data [24]. The F_2^γ data [24, 25, 26, 27, 30, 60] are partially used to fit the 5 free parameters given below. The high Q^2 data [30, 27, 60] were fitted for $n_f = 4$ flavours. Two sets of parameterisations are given, corresponding to two different assumptions on g^γ. The parametric form of the LO distributions are

$$q_i^\gamma(x, Q_0^2) = q_i^{PL}(x, m_u, m_s) + q_i^{HAD}(x, \kappa, B, C) \tag{2.27}$$

for the singlet and non-singlet sectors and

$$g^{\gamma}(x,Q_0^2) = g(x,\kappa,C) \tag{2.28}$$

or

$$g^{\gamma}(x,Q_0^2) = g(x,\kappa,C) + \frac{2}{\beta_0} P_{gq}(x) \otimes \Sigma^{PL}(x,m_u,m_s). \tag{2.29}$$

The quark masses $m_u (= m_d)$ and m_s are treated as bounded free parameters. The VMD part is treated as in Equation 2.9 and hence incorporates a κ factor. The parameters B and C are associated with the sea and gluon sectors of the pion respectively, which are of the form given by [61]. For the PL part, the lowest order Bethe–Heitler form [55, 56] is used. Charm is treated with the same way as for light flavours, with $m_c = 1.5$ GeV. The second term in Equation 2.29 represents a component to the gluon distribution estimated from Bremsstrahlung off the singlet quarks.

The NLO distributions have been constructed without a new fit to the data by enforcing the same $F_2^{\gamma}(x,Q_0^2)$ as in the LO case, together with assumptions on flavour decomposition.

2.7.4 Drees and Grassie (DG)

This is a LO parameterisation [62] that avoids the two-component decomposition of Equation 2.6. Parameterisations for the singlet, non-singlet and gluon distributions are obtained using the full solution of the LO inhomogeneous evolution equations [45] which are free of divergences [63]. The input distributions are chosen at $Q_0^2 = 1$ GeV^2 such that the only data that was available at the time [64], at $Q^2 = 5.9$ GeV^2 , are reproduced. The weakness of this parameterisation is that only 7 data points were available at one Q^2 value, so they were a poor constraint to the assumed 13 free parameters. $\Lambda = 0.4$ GeV throughout.

A 3–flavour evolution is used to evolve the input distributions up to $Q^2 = 50$ GeV^2. A charm contribution can be determined from the direct QPM process. To obtain the parton distribution functions for 4 and 5 flavours the 3–flavour input at Q_0^2= 1 GeV^2 is used to evolve up to Q^2= 500 GeV^2 and Q^2= 10000 GeV^2 with a 4– and 5–flavour evolution respectively. The 13 parameters are determined for each of the three evolutions.

2.7.5 Levy, Abramowicz and Charcula (LAC)

The aim of these LO parameterisations [65] was to apply the approach of Drees and Grassie to further available measurements of the photon structure function. The evolution starts at $Q_0^2 = 4$ GeV^2 for sets 1 and 2 and $Q_0^2 = 1$ GeV^2 for set 3. The evolution was carried out for 4 flavours, but the charm contribution to the photon structure function was only taken into account when $W^2 \geq 4m_c^2$, with $m_c = 1.5$ GeV. This threshold appears as a discontinuity in the $F_2^\gamma(x)$ distributions (see Figure 2.4). The x dependence of the input quark distributions at Q_0^2 is assumed to be

$$xq(x) = Ae_q^2 x \frac{x^2 + (1-x)^2}{1 - B\log(1-x)} + Cx^D(1-x)^E \tag{2.30}$$

for each of the four flavours and the gluon distribution at Q_0^2 is assumed to have the form

$$xG(x) = C_g x^{D_g}(1-x)^{E_g}. \tag{2.31}$$

There are a total of 12 free parameters. No attempt is made to fit the QCD scale parameter Λ which is assumed to be $\Lambda = 0.2$ GeV. The two terms in the quark distributions are intended to reflect the point–like and hadronic parts of photon structure. This was the first attempt to determine the gluon distribution in the photon. No physical constraints are placed on the quark flavour decomposition and on the gluon density. Vogt points out [66] how this approach leads to unphysical results (e.g. $s(x,Q^2) > d(x,Q^2)$ in some regions) and wild reactions of the fitted gluon density on fluctuations and offsets in the data. This demonstrates how the present F_2^γ data do not provide useful constraints on g^γ.

This parameterisation is used to generate some of the Monte Carlo samples used in this thesis (see Chapter 5).

2.7.6 Aurenche et al. (ACFGP)

These distributions are only in NLO [67] (with the $\overline{MS}$ factorisation scheme). A pure VMD input was used at $Q_0^2 = 0.25$ GeV^2. The parameterisation of the parton distributions in the vector mesons at Q_0^2 are chosen such that after an

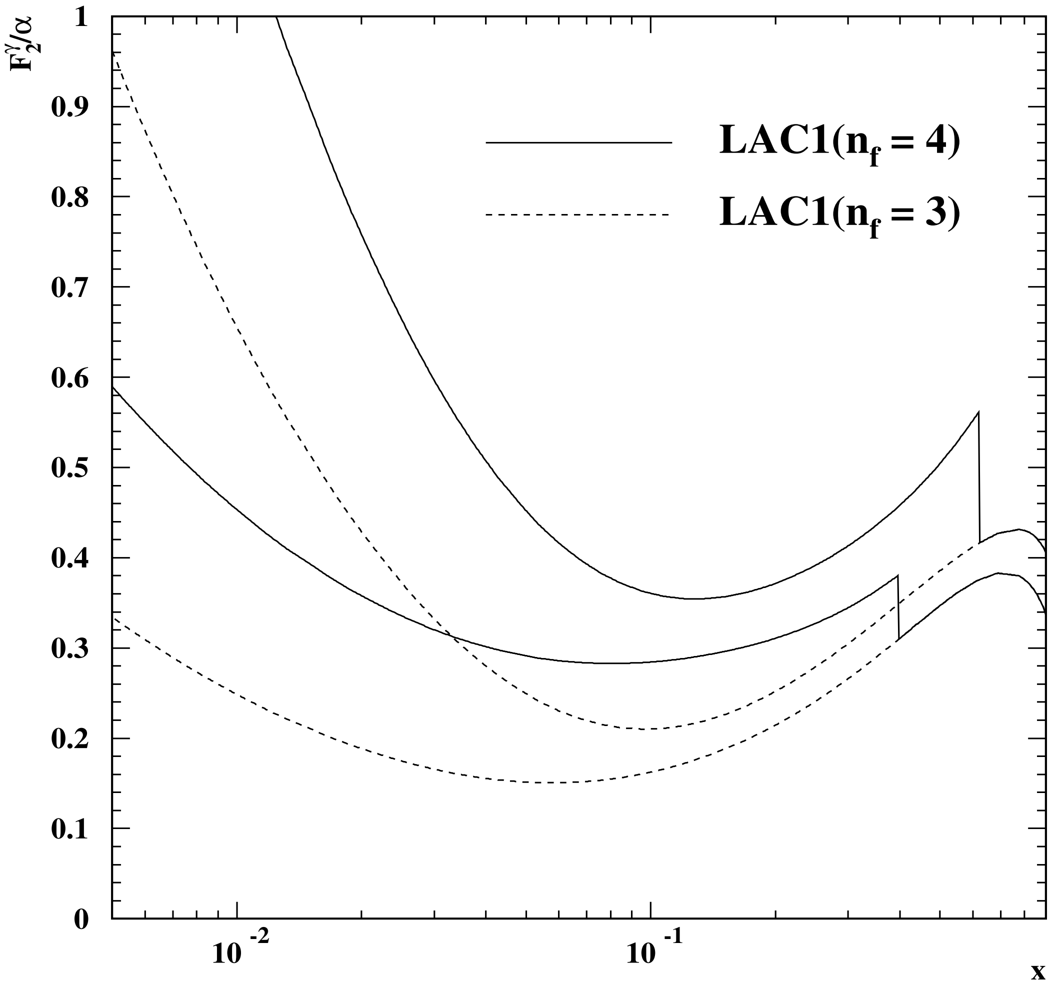

Figure 2.4: The LAC1 parameterisation for four flavours (solid lines) and three flavours (dashed lines). The lower curve of each pair is calculated at Q^2=5.9 GeV^2 and the upper curve of each pair is calculated at Q^2=14.7 GeV^2.

evolution between $Q_0^2 = 0.25$ GeV^2 and $Q_0^2 = 2$ GeV^2, they exactly correspond to the distributions in the pion determined [68] at Q^2= 2 GeV^2. No fit to the F_2^γ data is performed, and no attempt is made to explain the data at $Q^2 \simeq 1$ GeV^2, where higher twist contributions may be non negligible.

At $Q^2 = 2$ GeV^2 an $n_f = 4$ evolution begins which generates a charm distribution, but in the calculation of F_2^γ this distribution is not used. Instead the expression of [69] is used which correctly accounts for the charm mass threshold. $\Lambda_{\overline{MS}}(n_f = 4)$ is fixed to 200 MeV.

2.7.7 Field, Kapusta and Poggioli (FKP)

A different approach to calculating F_2^γ is by the direct summation of Feynman diagrams [46, 47], where leading log ladder diagrams are summed to all orders in $\alpha_s(Q^2)$. FKP used this method [48, 49] to calculate F_2^γ and they introduced a phenomenological cut–off (p_t^0) in the p_t of the quarks at the $\gamma \to q\bar{q}$ vertex. This separates the hadronic and point–like components of the photon structure function. Furthermore, Kapusta [70] detailed a derivation of various contributions to the photon structure function in the perturbative region. This all–order QCD approach by FKP was parameterised in an AMY paper [30] and is assumed to apply for all $p_t > p_t^0$. A separate part for the hadronic component must be added to the cross–section for $p_t < p_t^0$, which is not provided in the FKP model. The hadronic component is usually assumed to be parameterised by the TPC/2γ formula of Equation 2.10. The 'FKP + TPC/2γ VMD' construction is illustrated in Figure 2.2, for two values of Q^2 and two values of p_t^0.

The FKP model has been shown to have limitations [71]. In particular, it has been pointed out that the FKP result does not reproduce the correct small-x behaviour of F_2^γ (for $x < 0.5$). Also, the 'FKP + TPC/2γ VMD' construction has been shown to be inconsistent, since the FKP F_2^γ is already large at $Q^2 = 0.71$ GeV^2, where the TPC/2γ parameterisation alone is supposed to describe the data.

2.7.8 Schuler and Sjöstrand (SaS)

This is the most recent set of parameterisations of the photonic parton distribution functions [71]. Schuler and Sjöstrand point out the problems of the FKP model and then provide a solution to these problems with their own parton distribution functions.

The photon structure function is separated into perturbative ('anomolous') and non–perturbative (hadronic) contributions. The anomolous part is fully calculable and depends on x, Q^2, Q_0, Λ and P^2.

The shapes of the hadronic distributions are obtained by fitting to the available $F_2^\gamma(x, Q^2)$ data. This is to be contrasted with the GRV and ACFGP parameterisations which approximate the hadronic input distributions by using distributions in the pion. The charm contribution to F_2^γ uses the leading order Bethe–Heitler cross–section, with $m_c = 1.3$ GeV. Four different sets of hadronic parton distribution functions are provided, corresponding to different starting scales and different factorisation schemes. These are SaS1D (DIS, $Q_0 = 0.6$ GeV), SaS1M ($\overline{MS}$, $Q_0 = 0.6$ GeV), SaS2D (DIS, $Q_0 = 2.0$ GeV) and SaS2M ($\overline{MS}$, $Q_0 = 2.0$ GeV).

A selection of 3–flavour $F_2^\gamma(x)$ parameterisations are shown in Figure 2.5. The figure highlights that much of the theoretical uncertainty in $F_2^\gamma(x)$ lies in the $x < 0.1$ region. The rest of this thesis is now concerned with the low-x data from OPAL, which extend into this region.

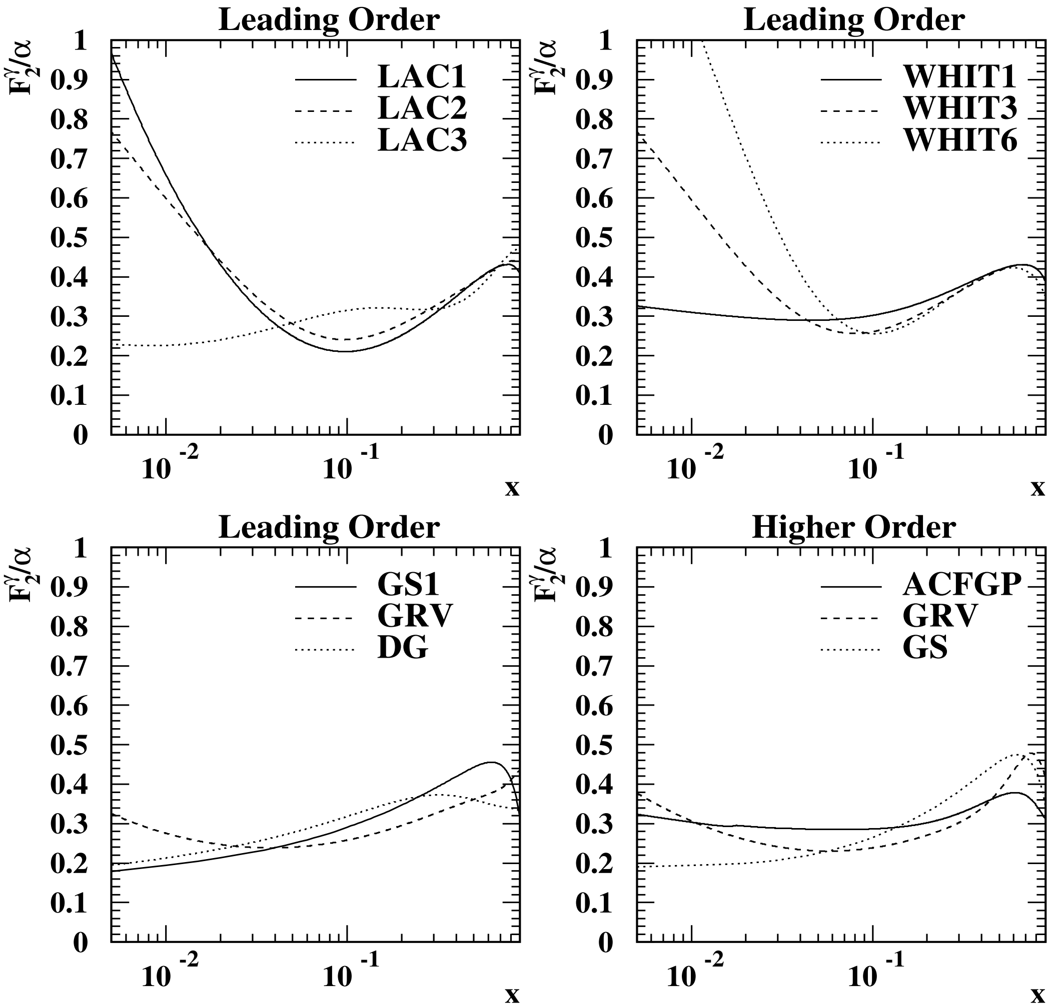

Figure 2.5: A selection of three–flavour $F_2^\gamma(x)$ parameterisations from Section 2.7. All of these curves are calculated at Q^2=14.7 GeV^2.

Chapter 3

LEP and the OPAL Detector

A brief description of LEP is given, followed by a more detailed account of the OPAL detector. Particular attention is given to the Forward Detector, where the two-photon collisions are tagged.

3.1 LEP

The LEP collider, at CERN near Geneva, is almost 27 km in circumference and 100 m below the surface. Since July 1989 it has accelerated electrons and positrons in opposite directions around the ring, bringing them into collision at the centre of mass energy of the Z° resonance (approximately 91 GeV). This was the LEP1 phase of LEP operation. In October 1995 the centre of mass energy was increased to 130 GeV and 136 GeV, as a first step towards reaching the $W^{+}W^{-}$ pair threshold of 160 GeV.

The data analysed in this thesis are taken from the OPAL [1] detector, which is one of four large detectors built around LEP (the other three are ALEPH, L3 and DELPHI).

3.2 The OPAL Detector

OPAL is a multipurpose apparatus designed to have efficient detection, with accurate and unambiguous event reconstruction of all possible interactions occuring in e^+e^- collisions. The general layout of the detector is shown in Figures 3.1 and 3.2. The main features of OPAL are:

- Tracking of the trajectories of charged particles in the central region of a magnetic field with measurements of their direction and momentum, particle identification using dE/dx, and reconstruction of primary and secondary vertices using the central tracking detectors.
- Measurement of energy and direction of photons and electrons using electromagnetic calorimeters.
- Measurement of hadronic energy by total absorption in the instrumented magnetic return yoke (the hadron calorimeter).
- Identification of muons by measuring, with the muon chambers, the position and direction of particles which have passed through the hadron calorimeter.
- Measurement of the absolute machine luminosity using Bhabha scattering events in the forward direction with respect to the beam line using the forward detector or the silicon-tungsten luminometer. The forward detector also measures the energy and angle of the tagged electrons for events used in the two–photon analysis.

The OPAL Coordinate System

The z–direction is along the beam direction and in OPAL this coincides with the direction of the electrons (which is anti–clockwise when LEP is viewed from above). The x–direction points towards the centre of the LEP ring. The y–direction is normal to the x–z plane, such that the three directions form a right–handed coordinate system. The z–direction is inclined by $1.39°$ with respect to the horizontal and therefore the y–direction is inclined by $1.39°$ with respect to the vertical. It is common for a mixture of cylindrical and spherical coordinates to be used, where the z–direction is the same as defined above, the θ–direction

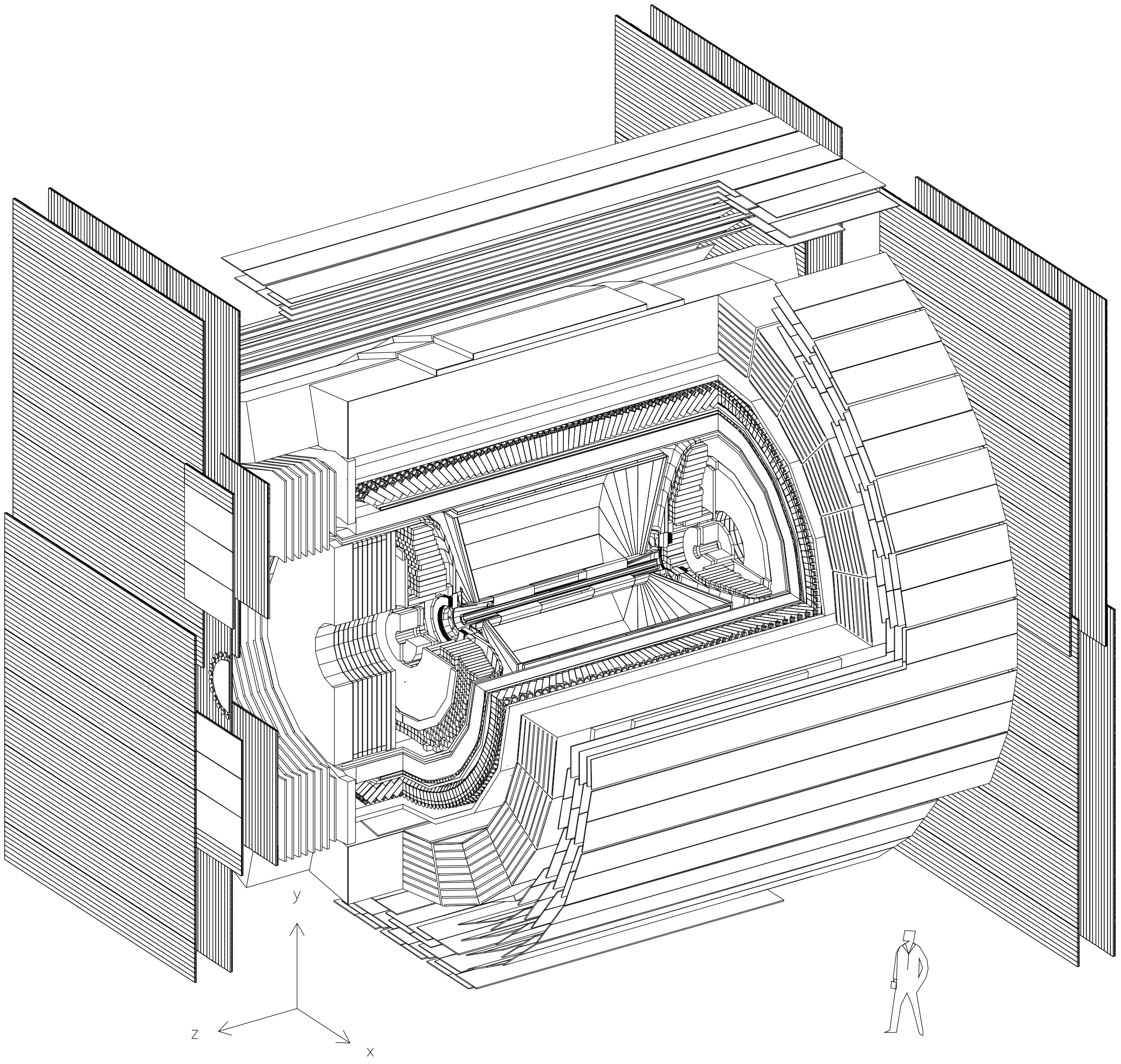

Figure 3.1: A cut-away view of the OPAL detector.

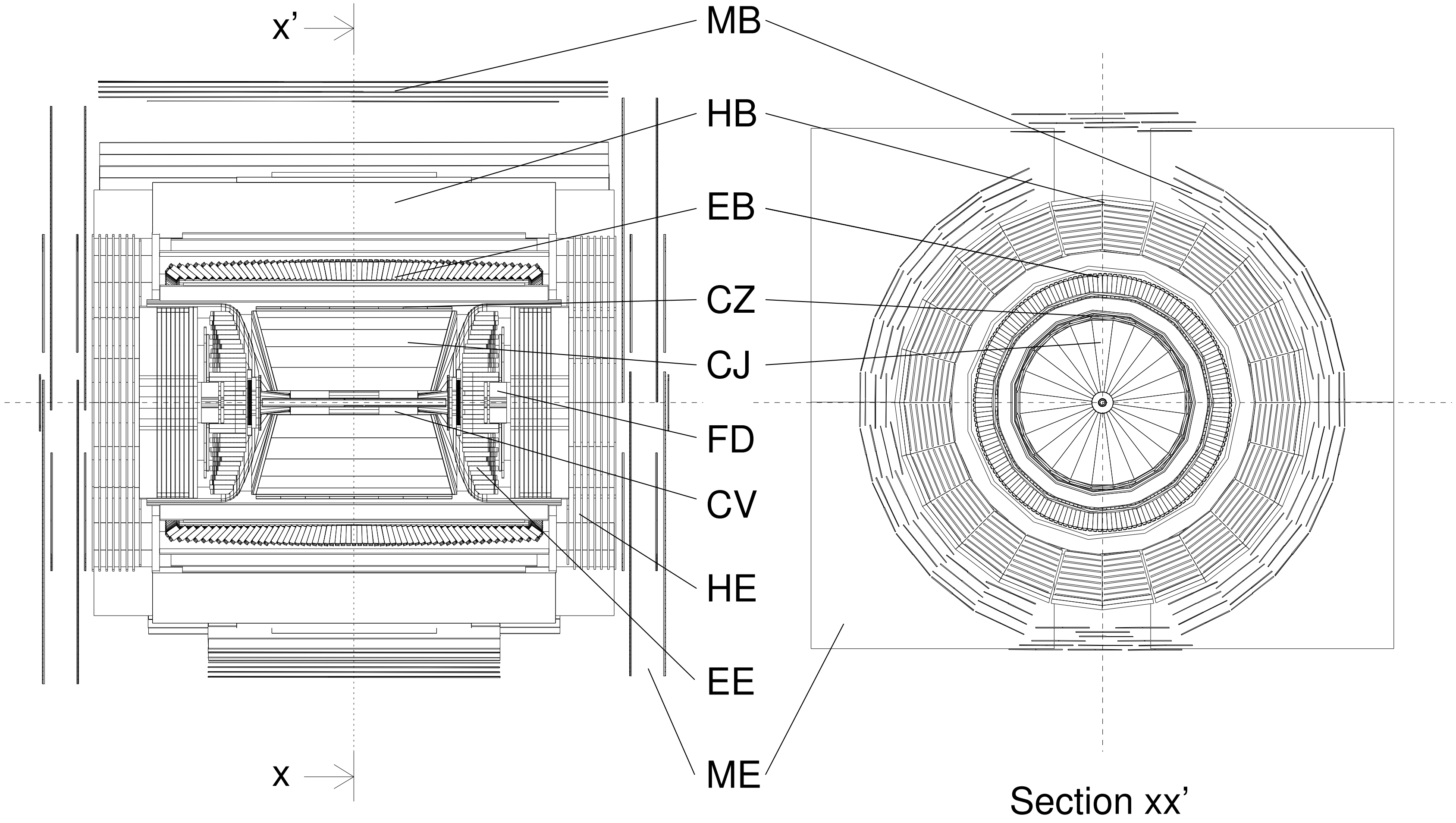

Figure 3.2: Side and end views of the OPAL detector, sectioned to show the main subdetector systems: central vertex chamber, jet chamber and z-chambers (CV, CJ and CZ), electromagnetic calorimeters (EB and EE), hadron calorimeters (HB and HE) and muon chambers (MB and ME). The forward detector modules (FD) can also be seen.

is the polar angle with respect to the positive z–direction and ϕ is the azimuthal angle which is 0 rad along the x–direction and $\pi/2$ rad along the y–direction.

The OPAL Magnet

The magnet consists of a solenoidal coil and an iron return yoke. The yoke is made of soft steel plates and can be split into five parts; a central part, two 'C'–shaped parts and two poletips. In the central cylindrical volume, which is used for tracking, the magnetic field is approximately 0.435 Tesla.

3.2.1 Central Tracking Detectors

The OPAL central tracking system consists of a silicon microvertex detector (μv), a vertex detector, a large volume jet chamber, and Z-chambers. The gas used in the central tracking detectors is common to CJ, CV and CZ and is under a pressure of 4 bar. The tracking system is within the solenoid of the magnet. The inner wall of the pressure vessel is at a radius of 7.8 cm from the interaction point. This formed the original beampipe, which consists of 0.13 cm thick carbon fibre with a 100 μm aluminium inner lining. The silicon microvertex detector was added to OPAL in the 1991/92 winter shutdown, inbetween the original beampipe and a new 0.11 cm thick beryllium beam pipe at a radius of 5.35 cm.

Silicon Microvertex Detector

This is a solid-state detector which was designed to measure and identify particles with small decay lengths ($\leq$ 1 cm) such as heavy hadrons and the τ-lepton. It is also used to search for new particles with similar decay lengths.

The detector was constructed from rectangular shaped ladders which form a two-layer cylindrical configuration with an intrinsic resolution of 5 μm in r-ϕ. In the 1992 shutdown the ladders were replaced with orthogonal pairs of single sided silicon detectors to give z information. This sub-detector is not used in this analysis.

Vertex Detector (CV)

The vertex detector is a 1 m long and 0.47 m diameter cylindrical drift chamber that is located between the outer beampipe and the jet chamber. It is used to determine the position of decay vertices of short-lived particles and to improve momentum resolution. It is segmented radially and has an inner layer of 36 axial cells with axial wires and an outer layer of 36 stereo cells with wires strung at a stereo angle of 4°.

Each axial cell contains 12 anode wires with a radial spacing of 5.3 mm and the stereo cells have 6 anode wires with a 5 mm spacing. These anode wires are staggered by ± 41 μm to resolve left right ambiguities. The axial cells provide a precise measurement of position in the $r-\phi$ plane with a resolution of about 50 μm. An approximate z-coordinate of a wire hit is found by measuring the time difference of the signal from each end of anode wire. This coarse measurement is used in the fast track trigger and for offline track finding. The combination of the stereo and axial cell information gives a more precise z-coordinate measurement for charged particles close to interaction region.

Jet Chamber (CJ)

The jet chamber records the tracks of charged particles and determines their momenta by measuring their curvature in the magnetic field. It assists in the particle identification by measuring dE/dx.

The sensitive volume of the jet chamber is cylindrical with a length of about 4 m, inner diameter 0.5 m and outer diameter 3.7 m. It surrounds the beampipe and the vertex detector. The chamber is divided in ϕ into 24 identical sectors each containing a plane of 159 sense wires, all of which are parallel to the beam direction. The wire planes are radial. Cathode wire planes form the boundaries between adjacent sectors. The maximum drift distance varies from 3 cm at the innermost sense wire to 25 cm at the outermost wire. 159 points are measured in the polar angle range $43° < \theta < 137°$ and at least 20 points on a track are obtained over 98% of the 4π solid angle. The average resolution in $r-\phi$ is 135 μm and the average z resolution is 6 cm. The momentum in the $r-\phi$ plane (p_t in GeV) is measured with a resolution given by

$$\frac{\sigma(p_t)}{p_t} = [0.02^2 + (0.0015p_t)^2]^{\frac{1}{2}}. \quad (3.1)$$

Z-Chambers (CZ)

The Z-chambers make precise measurements of the z–coordinates of charged particles as they leave the jet chamber, thus improving polar angle resolutions. They are arranged to form a barrel layer around the jet chamber and have a polar angle acceptance of $44° < \theta < 136°$. They consist of 24 drift chambers, 4 m long, 50 cm wide and 59 mm deep. Each chamber is divided across z into eight 50 cm$\times$50 cm cells so that the maximum drift distance is 25 cm in the z direction. Each cell has 6 anode wires strung along the ϕ direction, with 4 mm spacing and a $\pm$ 250 μm staggering to resolve the left-right ambiguity. The z resolution is around 300 μm and the $r - \phi$ resolution, from charge division, is about 1.5 cm.

3.2.2 Time-of-Flight

The time-of-flight (TOF) system covers $|\cos\theta| < 0.82$. It generates trigger signals, helps in particle identification and aids in the rejection of background particles such as cosmic rays. The TOF system consists of 160 scintillation counters, each 6.84 m long, forming a barrel of mean radius 2.36 m.

3.2.3 Electromagnetic Calorimetry

The electromagnetic calorimeter system measures the energies and positions of electrons, positrons and photons, ranging from tens of MeV up to beam energy. It is a total absorption calorimeter for electromagnetic showers and is mounted between the coil and the return yoke of the magnet. It consists of three large assemblies of lead-glass blocks, the barrel and two endcaps. These cover 98% of the solid angle. Particles must traverse about $2X_\circ$ of material, mostly due to the magnet coil and pressure vessel, before reaching the calorimeters. Therefore, most electromagnetic showers are initiated before the lead glass itself. Presampling devices are installed in both the barrel and endcap regions, immediately in front of the lead glass, to measure the position and sample the energy of these showers. The lead-glass system coupled with the presampler system provides some π°-photon discrimination and, in conjunction with the central tracking system, electron-hadron discrimination. Lead-glass was chosen for its excellent intrinsic energy resolution ($\sigma_E/E \sim 5\%/\sqrt{E}$ where E is the electromagnetic energy in GeV). The angular resolution of electromagnetic clusters is $\sim$4 mrad both in θ and ϕ for energies above 10 GeV.

Barrel Presampler (PB)

The barrel presampler consists of a cylinder of limited streamer mode wire chambers between the time-of-flight system and the barrel lead-glass calorimeter. There are 16 chambers covering the surface of a cylinder of radius 2.4 m and length 6.62 m. Each chamber is 3 cm thick and consists of two layers of limited streamer mode tubes with sense wires running axially. Readout is obtained from 1 cm wide cathode strips located on both sides of each layer of tubes and oriented at 45° to the wire direction. The strips on opposite sides of a layer are orthogonal. In addition, the charge collected on each wire is measured at both ends to provide a z position.

The resolution for the position of electromagnetic showers, in the plane perpendicular to the shower direction, varies from about 6 to 4 mm as the energy changes from 6 to 50 GeV. This corresponds to an angular resolution for photon trajectories of $\sim$2 mrad. The resolution in z from current division is $\sim$10 cm for a single charged particle.

Endcap Presampler (PE)

The endcap presampler is an umbrella shaped arrangement of 32 chambers in 16 sectors located between the pressure bell of the central tracking system and the endcap calorimeter. They cover the full azimuthal angle and the polar angular region defined by $0.83<|\cos\theta|<0.95$. The endcap presampler has an angular resolution of $\sigma_{PE} \sim 4.6$ mrad.

Barrel Lead-Glass Calorimeter (EB)

The barrel lead glass calorimeter consists of a cylindrical array of 9440 lead-glass blocks of 24.6 $X_\circ$, located at a radius of 2455 mm, outside the magnet coil, covering the full azimuthal angle and the polar angular region defined by $|\cos\theta|<0.82$. The longitudinal axes of the blocks are arranged such that each block points not at, but near to ($\sim$30 mm) the interaction point. This prevents neutral particles from escaping through the gaps between the blocks. In the z direction the calorimeter is segmented into 59 blocks. In the ϕ direction the calorimeter is segmented equally into 160 blocks.

The blocks are instrumented with magnetic field tolerant phototubes. Each lead-glass block is $\sim$10 cm$\times$10 cm in cross-section and 37 cm in depth. For optical isolation each is wrapped in a black sheet of vinyl fluoride, the inner surface of which is coated with aluminium for efficient light reflection.

The typical energy resolution of the combined presampler and lead–glass system, without any material in front, was found to be $\sigma_E/E \simeq 0.2\% + 6.3\%/\sqrt{E}$.

Endcap Lead-Glass Calorimeter

The endcap electromagnetic calorimeter (EE) consists of two dome-shaped arrays, each of 1132 lead glass blocks, located between the pressure bell of the central tracking system and the pole tip hadron calorimeter. It covers the full azimuthal angle and the polar angular range of $0.81<|\cos\theta|<0.98$. The lead-glass blocks are mounted with their axes coaxial with the beam line, because of tight geometrical constraints, and the phototubes were developed to operate in the full axial field of the magnet. The detector follows the curve of the pressure bell, and thus the blocks come in three lengths, typically of 22 $X_\circ$.

The spatial resolution was found to be 8–14 mm for a 6 GeV electron beam incident at 15° to the longitudinal block axes.

3.2.4 Hadron Calorimeter

The hadron calorimeter measures the energy of hadrons that emerge from the electromagnetic calorimeter and assists in muon identification. The iron of the return yoke provides at least 4 interaction lengths of absorber over 97% of the 4π solid angle. The yoke is segmented into layers, with planes of wire chambers between each layer, and forms a cylindrical sampling calorimeter about 1 m thick. To achieve the high solid angle coverage, the hadron calorimeter is constructed in three sections: the barrel, the endcap and the poletip. Most hadronic interactions are initiated in the 2.2 interaction lengths of material before the hadron calorimeter, so the total hadronic energy is determined by combining signals from both the electromagnetic and hadron calorimeters. The hadron calorimeters are not used in this analysis.

3.2.5 Muon Detector

The muon detector is a system of large-area drift chambers constructed as a barrel and two endcaps. It covers the iron yoke almost completely. 93% of the 4π solid angle is covered by at least one layer of detector. The amount of material that a particle has to traverse before reaching the muon detector exceeds the equivalent of 1.4 m of iron (over 7 interaction lengths for pions). This reduces the probability of a pion not interacting, thus faking a muon, to less than 0.001. The efficiency for detecting isolated muons above 3 GeV is essentially 100%.

The barrel part of the detector covers $|\cos\theta| < 0.68$ with four layers of drift chambers and $|\cos\theta| < 0.72$ with one or more layers. The endcap part of the detector covers the range $0.67 < |\cos\theta| < 0.98$ with four layers of limited streamer tubes that are perpendicular to the beam axis.

Muon identification relies on extrapolating the track seen in the central tracking system through the iron absorber, allowing for energy loss and multiple coulomb scattering, and looking for a track in the muon detector which matches in position and angle in two views. The positional and angular accuracies required for the track measurement are determined by the multiple scattering of the highest energy muons of interest and are about 2 mm and 3 mrad respectively.

3.3 OPAL Forward Detectors

These detectors are essential to the present analysis. They are used to measure the luminosity of LEP by detecting small-angle Bhabha scattering events and to measure the energy and position of tags from photon-photon interactions. The forward region consists of the forward detector system and, from 1993 onwards, the silicon-tungsten calorimeter. The outer physical edge of the forward calorimeter was 165 mrad before 1993 and 154 mrad from 1993 onwards. The pre–1993 geometry of the forward region is illustrated in Figure 3.3.

3.3.1 Silicon Tungsten Calorimeter (SW)

The silicon-tungsten detector consists of two cylindrical small-angle calorimeters encircling the beampipe at ± 2389 mm in z from the interaction point. They have an angular acceptance of 25 mrad to 59 mrad. The radial position resolution on electron showers is approximately 10 μm and the energy resolution is $\sigma_E/E \sim 28\%/\sqrt{E}$. Each calorimeter is built up from 19 layers of silicon sampling wafers and 18 layers of tungsten, corresponding to a total of 22 radiation lengths.

A silicon layer consists of 16 wedge shaped detectors, where each wedge covers $22.5°$ in ϕ with an inner radius of 62 mm and an outer radius of 142 mm. A wedge is divided into 64 pads, 32 in r and 2 in ϕ, so in the entire system there are 38912 channels that are read out individually. Adjacent wedges in a layer are offset by 800 μm in z and positioned in such a way that there is no gap in the active area of the silicon. Consecutive layers in the detector are offset in ϕ by half a wedge ($11.25°$). This sub-detector is not used in this analysis, since this data sample is taken from 1990-1992 LEP running.

3.3.2 Forward Detector (FD)

Before the SW detector was installed in 1993, there was a clean acceptance for particles from the intersection region between 47 and 120 mrad from the beam line. In this range the only obstructions were 2 mm of carbon fibre in the beam pipe (traversed obliquely, so up to 0.2 $X_\circ$ thick) and 2 mm of aluminium in the thin

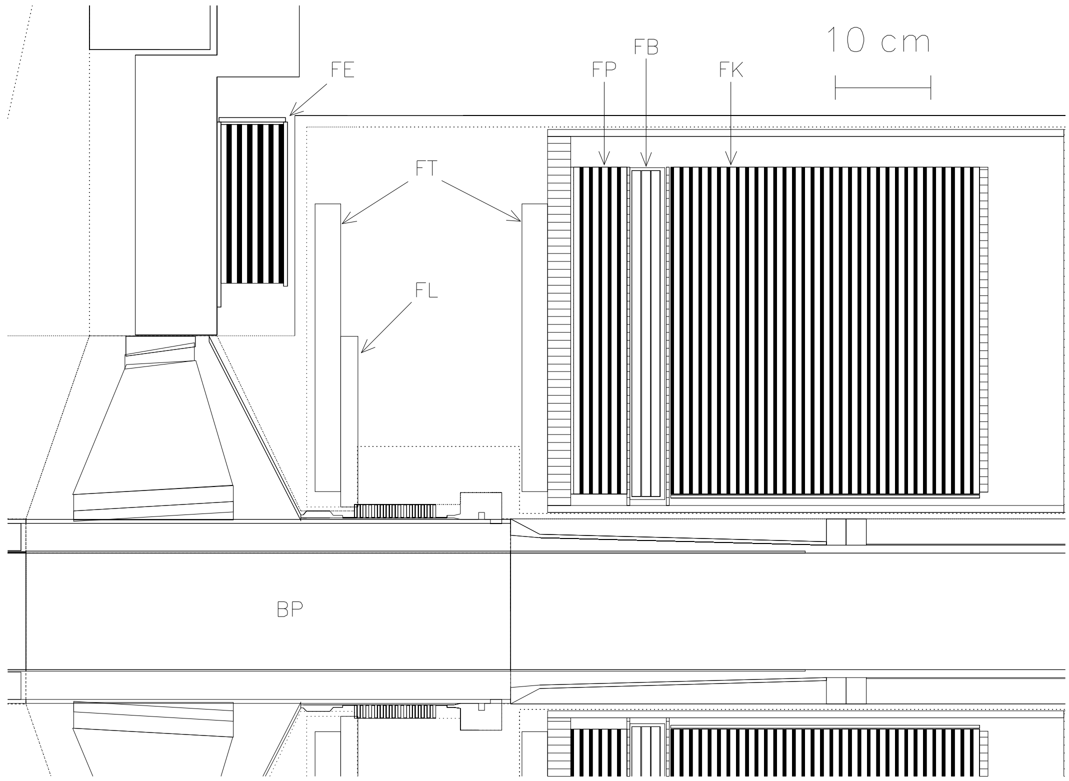

Figure 3.3: Cross section through the forward region (pre–1993) between 2 and 3 metres from the intersection region (which is to the left of this diagram). BP = Beam Pipe, FT = Drift Chambers, FL = Fine Luminosity Monitor, FE = Gamma Catcher, FP = Presampler Calorimeter, FB = Tube Chambers and FK = Main Calorimeter.

window of the central tracking system pressure vessel, with aluminium webs in the horizontal and vertical planes to support the beam pipe. The front drift chambers and the "acceptance" counters of the fine luminosity monitor were mounted on the front of a light stiff honeycomb plate which has a thickness equivalent to 1 mm of aluminium. The inner part of the acceptance of the calorimeter, down to 39 mrad, was obstructed by a thick aluminium ring and by the bellows and flanges joining the beam pipe to the pressure window. Beyond 120 mrad there are obstructions inside the pressure vessel, including optics for the laser beams used to calibrate the jet chamber. The space which they occupy between the forward calorimeter and the endcap lead glass causes a gap in the calorimetric acceptance in the polar angle region 142–200 mrad which is covered by the gamma catcher.

Calorimeter (FK)

The forward calorimeter has 35 sampling layers of lead-scintillator sandwich (24 $X_\circ$), read out with wavelength shifter to vacuum phototetrodes. It is divided into a presampler of 4 $X_\circ$ and the main calorimeter of 20 $X_\circ$. The presampler has wavelength shifter at the outside only, but the main calorimeter is read out on both the inner and outer edges to provide a θ measurement. There are sixteen azimuthal segments. The energy resolution has been measured as $\sigma_E/E \sim 18\%/\sqrt{E}$. The polar angle resolution on electron showers is ± 4 mrad near the inner edge, but degrades to ± 10 mrad at the outer edge. The azimuthal resolution, from the ratios of signals in adjacent segments, is approximately $\pm 2°$.

Tube Chambers (FB)

Between the presampler and main sections of the calorimeter there are three planes of brass-walled proportional tube chambers [72]. Individual shower positions have a polar angle resolution of $\pm$ 2 mrad. Within the tube chamber acceptance the tube chambers and the calorimeter provide combined cluster information. The energy measurement comes from the calorimeter which also provides θ and ϕ for showers falling outside the tube chamber acceptance.

Drift Chambers (FT)

The drift chambers [73] were used up until the end of 1994. Each has two gas gaps with two sense wires per gap. Drift directions are approximately radial. The ambiguity between inward and outward drifts is resolved by displacing the sense wires in the first gap of each chamber outwards by 2 mm from those in the second gap. The position of a hit along a wire is measured by charge division and by a pattern of intersecting diamond pads on the faces close to the wires. These have been used to accurately survey the positions of the tubes within the calorimeter. In 1992 the small-angle reference chambers (SARCs) were inserted.

Fine Luminosity Monitor (FL)

The fine luminosity monitor consisted of four pairs of precisely positioned 6 mm thick scintillators at each end, on the 45° diagonals to avoid showers from the beam pipe support webs. They covered the angular region 50–109 mrad from the beam axis, with an azimuthal coverage of about 36%. The front “acceptance” counters were 10 mm smaller on all sides than the rear “coincidence” counters. They provided a luminosity measurement used to check the main calorimeter/tube based measurement. The monitor was removed when the SARCs were inserted.

Gamma Catcher (FE)

The gamma catcher is a small electromagnetic calorimeter physically extending in θ from 143 mrad to 193 mrad. It thus covers the annular region between the outer physical edge of the forward calorimeter and the inner EE lead-glass calorimeter. It comprises eight independent azimuthal segments at each end, which provide a coarse determination of the ϕ angle. Each segment consists of a lead-scintillator sandwich which is read out along the outer edge with a wavelength shifter bar and two 1 cm^2 silicon photodiodes. The calorimeter is non-containing, with approximately 7 $X_\circ$ of active material and 3 $X_\circ$ of material in front of it. A high energy electromagnetic shower will thus be shared either with the forward calorimeter or the inner EE blocks depending on the θ angle of the interacting particle. The energy resolution for Bhabhas is $\simeq$ 20%. More technical details on FE can be found in [74].

Far Forward Monitor (FF)

The far forward luminosity monitor counters are small lead-scintillator calorimeters (50 mm $\times$ 150 mm $\times$ 20 $X_\circ$) mounted on either side of the beam pipe 7.85 m from the intersection region, beyond the low-beta quadrupoles. They are used for a high statistics "online" luminosity and to monitor beam backgrounds. They may in the future be used for double-tags of $\gamma\gamma$ events with $0.1 \leq P^2 \leq 1.0$.

3.4 OPAL Triggers and Data Stream

OPAL only records events if they satisfy certain trigger conditions. These conditions allow us to separate interesting physics processes from uninteresting background processes, detector noise and beam-crossings where no interactions occur.

It must be ensured that the trigger can respond to tagged two-photon events. This section describes the trigger with emphasis on the tagging triggers. The flow of information away from the detector is followed to the point where a selection of events for analysis can be made. A general description of the OPAL trigger system can be found in [75].

Triggers

Subdetector trigger signals are of two types, 'stand-alone' signals (high thresholds) and signals from a θ-ϕ binning (low thresholds). The high threshold trigger signals are typically multiplicity counts or energy sums. The low threshold trigger signals are formed from one of the $6(\theta) \times 24(\phi)$ overlapping bins that cover the 4π solid angle of the detector. The trigger processor makes a decision, which is programmable, by forming spatial correlations between subdetectors in θ-ϕ and stand-alone signals.

Tagging Triggers

A list of relevant OPAL triggers used for tagged two-photon events and their descriptions are given in Table 3.1. A 'coincidence' is where a track hit coincides with an energy deposit in a calorimeter in the same θ-ϕ bin. A TOF hit is a hit in the Time Of Flight counter.

A tagged two-photon event will be read out by OPAL if one of the stand-alone trigger conditions (from *either* tag *or* hadronic activity) in Table 3.1 is satisfied, or if one of the programmable conditions (combining both tag and hadronic information) in Table 3.2 is satisfied. All such conditions are chosen to ensure that the tagging trigger efficiency is high and does not include too much background.

Data Stream

The central trigger logic is installed in a dedicated Eurocrate with a special 'trigger bus' in addition to the standard VME/VSB bus. Logical combinations of signals on the trigger bus (i.e. subdetector stand–alone signals and θ-ϕ matrix outputs) are formed by the 'pattern arrangement module' (PAM), which uses look–up memories to derive the trigger decision from the 120 possible outputs.

The global trigger unit (GTU) sends its trigger decision to the local trigger units (LTUs) of each sub-detector. If the trigger decision is negative a reset pulse is distributed 6 μs before the next bunch crossing. If the decision is positive the GTU transfers a central event number and other information to the LTUs. Each LTU inhibits further triggers when sub-detector readout is in progress. The amount of time during the readout when no new triggers can be taken is called deadtime.

Each sub-detector is read out separately by its own front-end electronics to the local system crate (LSC). This digitised information is collected and merged into a single data structure by the event builder (EVB) VME system. Each complete event is passed to the filter where events are checked, analysed, monitored and compressed before being written to disk. Obvious background events are rejected at this stage. Information generated from each event is copied from the filter disk to the ROPE farm, where the full OPAL reconstruction code ROPE [76] is run and where the calibration constants are applied.

Trigger Name	Description
For tags:	
L(R)CALLO	$>$ 15 GeV deposited in left(right) FK
FDHIOR^S	$>$ 35 GeV deposited in either end of FK
FDGCL(R)T	$>$ 20 GeV in left(right) Gamma Catchers
SWHIOR	$>$ 34 GeV deposited in either end of SW
SWSEGL(R)	Left(right) segment trigger (9 GeV)
For particles from $\gamma^*\gamma$ collision:	
TBM1^C	$\geq$ 1 barrel track
TBM2^S	$\geq$ 2 barrel tracks
TM2	$\geq$ 2 tracks in the central detector
TM3^{SC}	$\geq$ 3 tracks in the central detector
EBTOTLO^C	$\geq$ 1.8 GeV in the electromagnetic barrel (EB)
EBWEDGE	Sum 'wedge' of EB $\geq$ 2 GeV
EEL(R)LO^C	$\geq$ 1.6 GeV in EE
EBTPHI^S	$\geq$ 1.8 GeV in one EB θ-ϕ bin
EEL(R)TPH^S	$\geq$ 1.6 GeV in one EE θ-ϕ bin
TPTTTO^{SC}	TOF hit and track coincidence
TPTTEM^{SC}	EB or EE deposit and track coincidence
TPTOEM^{SC}	EB or EE deposit and TOF hit coincidence

Table 3.1: Summary of triggers used in triggering tagged two-photon events, with typical threshold values. The superscript S indicates a standalone trigger and the superscript C indicates that the trigger forms part of the CENTRL trigger described in Section 4.3.2. The notation L(R) refers to the Left(Right) sides of OPAL.

All data	L(R)CALLO.AND.TBM1 L(R)CALLO.AND.EBTOTLO
Added in 1992 (Run 3566)	FDGCL(R)T.AND.TBM1 FDGCL(R)T.AND.EBTOTLO FDGCLT.AND.FDGCRT
Added in 1993 (Run 4210)	SWHIOR.AND.TBM1
Added in 1994 (Run 5128)	SWHIOR.AND.EBWEDGE SWHIOR.AND.TPEML(R) SWSEGL(R).AND.EBTOTLO L(R)CALLO.AND.EEL(R)LO FDGCL(R)T.AND.EEL(R)LO SWSEGL(R).AND.EEL(R)LO SWHIOR.AND.TM2

Table 3.2: Programmed trigger conditions combining triggers from tag and hadronic activity in tagged two-photon events.

Chapter 4

Event Selection

This chapter describes the three-stage selection of singly-tagged two-photon events. Once a final set of events has been chosen, the remaining backgrounds are estimated. The trigger efficiency is measured using the final data sample. As a consistency check, the data taken in each of the years 1990, 1991 and 1992 are compared to each other. The 1993–1995 data are not used in this thesis because the tagging acceptance had changed with the inclusion of the silicon–tungsten detector.

4.1 Event Selection

The aim of the following event selection is to obtain a final sample of singly-tagged two-photon events that has as little contamination of other event types as possible. This is a three-step process. A very loose selection of events, called the **preselection** is applied, followed by a **further selection** which is made from running the gamma-gamma analysis routine (GG106) on every preselected event. The **final selection** produces the final sample of events.

4.1.1 Preselection

ROPE (version 408) calls a very loose preselection routine called RTWOPH that is designed to flag events that might be tagged two-photon collisions. These events are subset of events that are written to disk on the SHIFT [77] processor farm where they can be accessed using the OPAL analysis framework called MAW [78, 79].

The RTWOPH preselection flags events that have a cluster energy greater than 20 GeV in either forward detector and a minimum of two good tracks. The cuts that are made on track quantities that identify a track as being 'good' are given in Table 4.1 and the track quantites are described in Section 4.1.2.

	Quantity	Condition in GG106
Tracks	N_{CJ}	≥ 20
	$\lvert\cos\theta_{trk}\rvert$	≤ 0.95
	p_{Ttrk}	≥ 0.1 GeV
	p_{trk}	≥ 0.3 GeV
	$\lvert d_0\rvert$	≤ 2.5 cm
	$\lvert z_0\rvert$	≤ 50.0 cm
	dE/dx and N_{CV}	$dE/dx > 0$ *and* $N_{CV} > 0$
All Neutral Clusters	E_{raw}	≥ 0.17 GeV
		Cluster is not "hot"
		Cluster not associated with a track
EE Clusters	N_{blocks}	≥ 2
	F_r^{max}	99 %
Track-Cluster matching	η	<0.1 rad

Table 4.1: Quality cuts applied to the tracks, neutral clusters and the track-cluster association cone. The quantities are described in Section 4.1.2.

4.1.2 Further Selection

Each pre–selected event is examined in greater detail to improve the selection of tagged two-photon collisions. This will be discussed in detail below. We begin by requiring that relevant subdetectors are working well. Cuts on track quantities and electromagnetic cluster quantities are then applied, followed by track-cluster matching. The analysis uses only good quality tracks and clusters. Once this selection has been made, useful quantites are calculated that can be used in the physics analysis package PAW for the final selection.

Subdetector Status

Each subdetector provides a status number for every recorded event. The status numbers provided, and their meanings, are listed in Table 4.2. For this analysis we require that the status numbers of FD, EB, EE and CJ are each at least 2, and the Track Trigger status number is 3.

Status	Interpretation
0	Detector is dead
1	Detector is unreliable
2	Detector has small problems
3	Detector is 100 %

Table 4.2: Detector status number and interpretation.

Track Quality

The values of the track quality cuts are shown in Table 4.1.

Only tracks which satisfy a quality selection are used in this analysis. Each track must be well measured to determine its energy and momentum. A minimum number of Jet Chamber hits (N_{CJ}) on each track is demanded and the track must have a minimum angle (corresponding to a maximum $|\cos\theta_{trk}|$), a minimum momentum (p_{trk}) and a minimum transverse momentum (p_{Ttrk}) with respect to the beam.

Each track should come from the interaction point. Those that appear not to come from the interaction point may be artefacts due to jet chamber sparking, or come from such sources as beam wall interactions, beam gas interactions or backscatter in the solenoid from particles that have already left the jet chamber. Therefore, cuts are made on z_0, the apparent z-coordinate from which the track originated, and d_0, the apparent perpendicular distance from the interaction point in the $x-y$ plane from which the track originated. Some falsely reconstructed tracks have zero dE/dx and no CV hits, so any track with $dE/dx = 0$ *and* $N_{CV} = 0$ is not accepted as a good quality track.

Electromagnetic Cluster Quality

The values of the electromagnetic cluster quality cuts are shown in Table 4.1.

Clusters used for this analysis should not be due to either badly calibrated blocks or noisy electronics. Each cluster is compared to a list of noisy ("hot") blocks. A cluster associated with a noisy block and which has an energy close to the estimated noise is not used in this analysis. The energy of a cluster has to be corrected to account for energy deposited in the material in front of the lead-glass. This is a large correction for clusters with a small deposited energy, E_{raw}, so a minimum cut is made on E_{raw}. For a cluster in the electromagnetic endcap, which has its blocks mounted with their axes coaxial with the beamline, a minimum number of blocks (N_{blocks}) in the cluster is required, with no single block having more than $F_r^{max}\%$ of the raw cluster energy.

Track-Cluster Matching

To avoid double-counting of energy from a good quality track that has produced a good quality cluster, track-cluster matching must be performed. If a good quality cluster is within a cone of half-angle η radians around the track then it is matched with the track. If there are two clusters within the cone, the cluster closest in angle to the track endpoint is chosen, so one track is associated with a maximum of one cluster. The track and cluster energies are not used in the matching.

Calculation of x and W.

To calculate x (Equation 1.7) we need to measure the invariant mass W of the photon pair, as well as Q^2. In the single–tagging case this must be measured from the detected particles from the $\gamma^*\gamma$ collision. Instead of measuring the true invariant mass, W_{true}, we measure the visible invariant mass of the charged tracks and *unassociated* electromagnetic clusters in the lead–glass barrel and endcap. W_{vis} is given by

$$W_{vis} = \sqrt{\left(\sum E_{vis}\right)^2 - \left(\sum \vec{p}_{vis}\right)^2}. \tag{4.1}$$

W_{vis} is different from W_{true} because some particles may be lost, their energy and momentum mismeasured, and some tracks may be incorrectly matched to neutral clusters. Charged tracks are assumed to have the pion mass and the unassociated clusters are assumed to be photons. x_{vis} is the x value calculated using Q^2 and W_{vis}. When x and W are calculated using only tracks in the selected event, the corresponding variables are called x_{trk} and W_{trk}.

Since the unassociated clusters have been included in the W_{vis} calculation, which were not in the W_{trk} calculation, the W_{vis} distribution tends to have higher W and should be closer to the true W. Correspondingly, x_{vis} shifts to lower values than x_{trk} and is closer to the true x. When Forward Detector calorimeter clusters other than the tag cluster are included in the calculation, the resulting x distribution is called x_{visFD}. No cluster energy correction is made to account for the FD response to hadrons. Such a correction [80] has little effect on x_{visFD}.

4.1.3 Final Selection

The final selection cuts are given in Table 4.3. The variables used for the cuts are described in the following text.

The highest energy cluster in the Forward Detector is taken to be the tag. The energy of this cluster is called E_{tag}. The polar angular range of this cluster is confined to the well–understood region of the Forward Detector. The minimum E_{tag} requirement is effective in removing backgrounds from off-momentum beam particles, Z^0 decays and untagged two-photon events.

Tag	50 mrad $< \theta_{tag} <$ 120 mrad $E_{tag}/E_{beam} > 0.75$
Antitag	$E_{antitag}/E_{beam} < 0.25$
Multiplicity	$N_{trk} \geq 3$ $(N_{trk} - N_e - N_\mu) \geq 1$
Kinematics	$\lvert {p_T}^{tag} + {p_T}^{Vin} \rvert \leq 6$ GeV ${p_T}^{Vout} \leq 4$ GeV $2.5 < W_{vis} < 40$ GeV
Mean Vertex	<10 cm from the interaction point

Table 4.3: Final selection cuts. The quantities are described in Section 4.1.3.

The value of Q^2 is determined from the measured tag energy and tag polar angle (Equation 1.4). Assuming a 45.6 GeV electron is tagged at 50 mrad, with resolution in energy of $\sigma_E/E \sim 18\%/\sqrt{E}$ and an angular resolution of 2 mrad, one obtains a Q^2 value of 5.2 ± 0.4 GeV^2.

To observe deep inelastic $e\gamma$ scattering we require singly–tagged events with no candidate for a second tag at the opposite end (the anti–tag condition). The highest energy electomagnetic cluster (including the Forward Detector calorimeter) in the hemisphere opposite to the tag is called $E_{antitag}$ and is required to be no greater than a quarter of the beam energy. This removes most of the double-tag events from the sample and reduces the background from radiative Bhabha scattering.

Cutting on the charged multiplicity (N_{trk}) of the event removes backgrounds from tagged $\gamma\gamma \rightarrow e^+e^-$ and $\gamma\gamma \rightarrow \mu^+\mu^-$ events. Tagged $\gamma\gamma \rightarrow \tau^+\tau^-$ events are not easily identified and many of them look like hadronic events. Their contribution is estimated from the Vermaseren Monte Carlo (see Chapter 5).

Since we are interested in hadronic events, at least one of the tracks is required to not be positively identified as a electron or muon. Electrons are identified by using dE/dx information from the jet chamber. Muons are identified by the track being associated with hits in the muon chambers. The number of positively identified electrons and muons are N_e and N_μ respectively.

To further reduce such backgrounds, cuts are made on the p_T of the events and on the maximum W_{vis}. p_T^{tag} is the transverse momentum of the tag and is defined such that it is always positive. The capital letter in the superscript of other transverse momentum variables calculated from the final state refers to what the p_T has been calculated from. 'K' refers to the charged trac**K**s only, 'V' refers to the central **V**isible system (tracks and unassociated neutral clusters from the electromagnetic endcap and barrel only), 'H' refers to the **H**ighest momentum track and 'FD' refers to **F**orward **D**etector calorimeter clusters only (excluding the tag). The subsequent lower case letters 'in' or 'out' in the superscript indicate that the component of p_T being examined is either in or out of the plane defined by the tag and the beam.

A minimum value of W_{vis} is required to ensure events are not in the poorly known low-mass resonance region. Remaining beam-gas background is reduced by demanding that the primary track vertex is reconstructed near the interaction point in the z direction.

4.2 Estimation of Backgrounds

4.2.1 $e^+e^- \to$ hadrons

This clearly could be a large background, since there are many more Z^0 events than tagged two–photon events. However, the activity from a Z^0 event is less peaked in the forward direction than a tagged two–photon event, and the chance of a Z^0 event producing a cluster in the Forward Detector that might be mistaken for a two–photon tag is small. The distribution of the highest energy cluster in the Forward Detector from Monte Carlo Z^0 events is shown in Figure 4.1(a). Clearly, the minimum tag energy requirement is very effective in reducing the multihadronic background.

4.2.2 $e^+e^- \to \tau^+\tau^-$

The possibility that tau pairs from Z^0 decays could fake tagged two-photon events has been investigated. 300000 on–peak events have been produced with the KORALZ generator [81] and 3 of these events have passed the selection cuts. Since the total cross–section for $e^+e^- \to \tau^+\tau^-$ is approximately 1.5 nb [82], the actual background is negligible.

4.2.3 Non–multiperipheral $e^+e^- \to e^+e^-$ + hadrons

Some processes other than the multiperipheral diagram of Figure 4.2(a) can give rise to the same final state. These background processes, illustrated in Figure 4.2(b–d), have been studied using the Monte Carlo generator FERMISV [83], which incorporates both Z^0/γ exchange diagrams and interference terms. The bremsstrahlung diagrams with a γ rather than a Z^0 exchange are often referred to as "inelastic Compton scattering"diagrams [84].

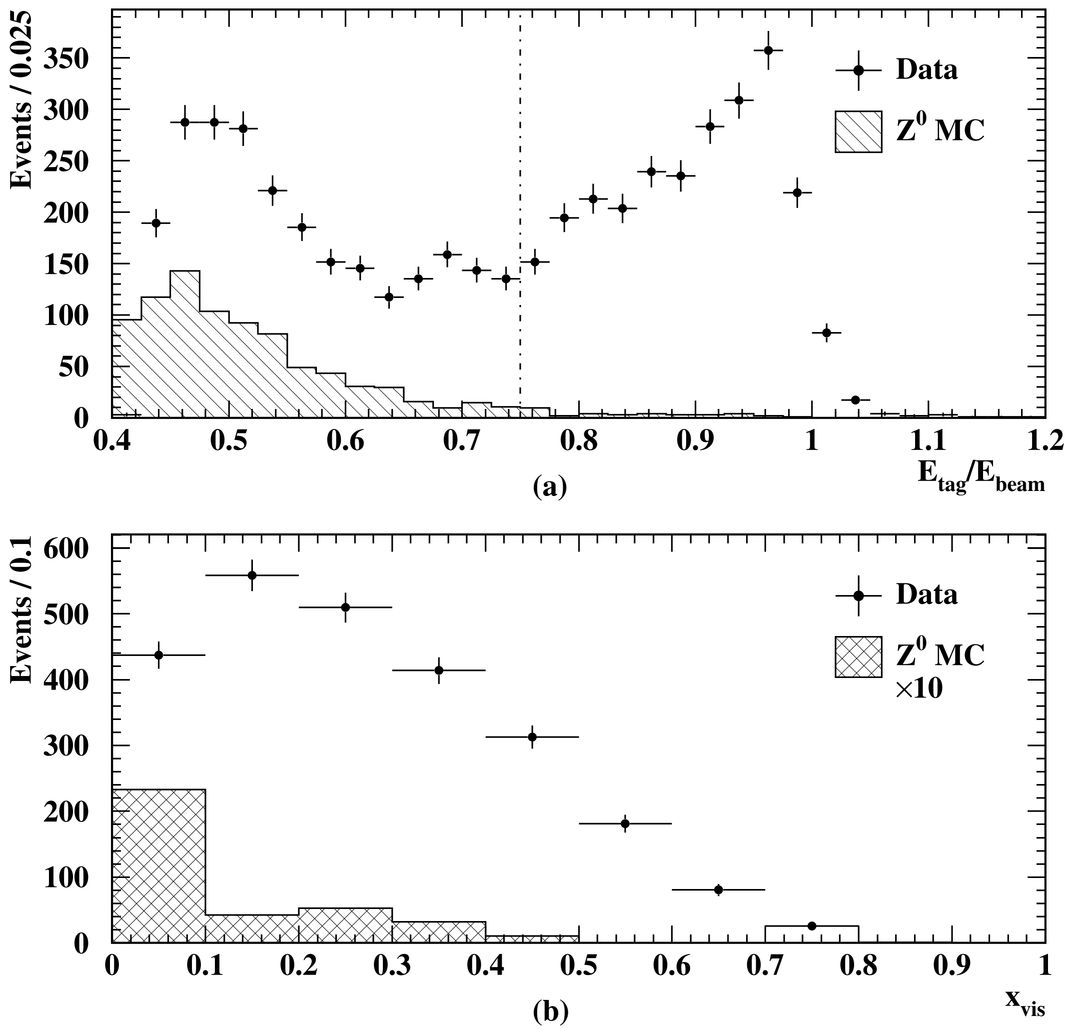

Figure 4.1: Estimate of Z^0 background events. (a) Distribution in E_{tag}/E_{beam}. The vertical dot–dashed line shows where the minimum tag energy cut is. (b) The distribution in x_{vis} after all of the selection cuts have been applied. The Z^0 background estimate in this histogram is enhanced by a factor of 10.

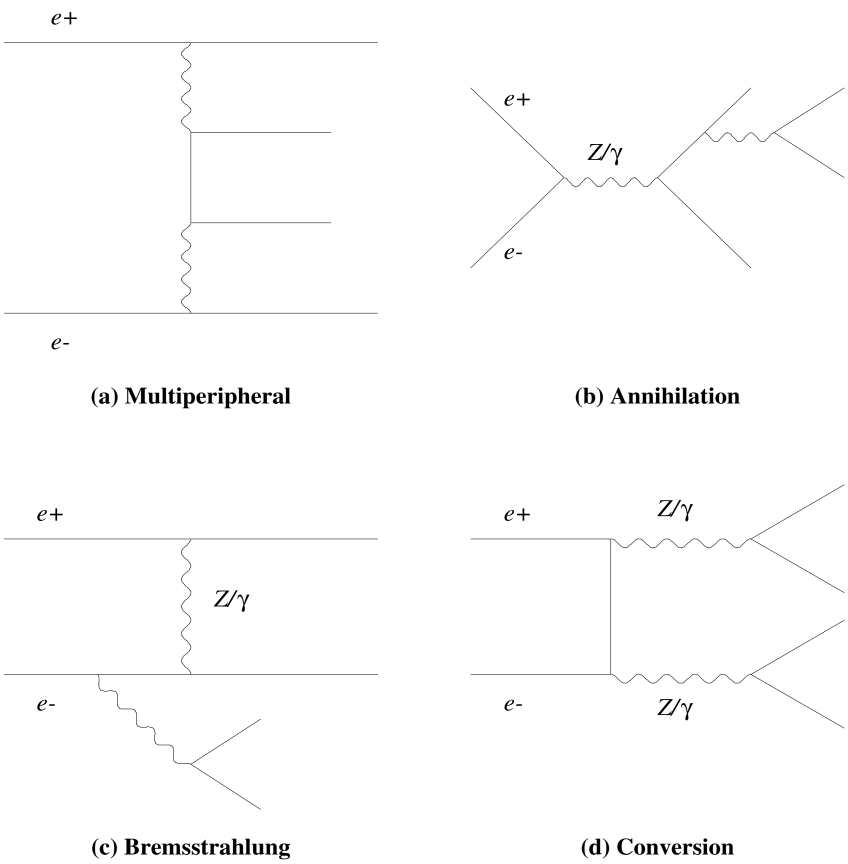

Figure 4.2: The four main diagrams contributing in the lowest order to the process $\gamma\gamma \to f^+f^-$. These processes are included in FERMISV. Unlabelled boson lines represent photons only.

The following background estimates are taken from [85]. The annihilation and conversion channels do not contribute more than 0.1% to the multiperipheral cross–section. The largest background contribution comes from the bremsstrahlung process. It has been estimated at $(0.4 \pm 0.2)\%$ of the multiperipheral cross–section. Nearly all of these events are uniformly distributed in x from 0.2 to 0.7.

The effect of interference between the multiperipheral and inelastic Compton scattering diagrams has been found to be negligibly small [85].

4.2.4 Beam–gas events

Background events that originate from interactions with residual gas in the beam pipe would have their vertex position uniformly distributed along the beam axis. By extending the primary vertex cut from ± 10 cm to ± 50 cm from the interaction point there are 24 more events in the sample. We therefore estimate that the final sample contains 6.0 ± 1.2 such events. Events where an off–momentum electron simulates a Forward Detector tag have been studied as part of the OPAL luminosity determination [82, 86, 87]. These events are clustered at low 'tag' energies and can be neglected, since a high tag energy cut is applied.

4.3 Trigger Efficiency

Before the data can be compared with itself (Section 4.4) or with the Monte Carlo (see Chapter 6) the trigger efficiency must be calculated. The relevant triggers for tagged two–photon events and their meanings have been given in Tables 3.2 and 3.1 respectively.

4.3.1 Calculation of Efficiency

The efficiency of a trigger is determined by comparing it to another independent trigger. Two independent triggers, F and C, are examined. Here, 'independent' means that the chance of F firing is unaffected by whether C has fired or not. There are four classes of events; neither trigger has fired, F only has fired, C

only has fired and both have fired. If F only has triggered N_F events, C only has triggered N_C events and both F and C have triggered N_{FC} events then the efficiency, ϵ_F, of trigger F is

$$\epsilon_F = \frac{N_{FC}}{N_{FC} + N_C}, \tag{4.2}$$

and the efficiency, ϵ_C, of trigger C is

$$\epsilon_C = \frac{N_{FC}}{N_{FC} + N_F}. \tag{4.3}$$

If every event fires at least one of the two triggers, and assuming that those events that fire neither are not recorded, then the total trigger efficiency is estimated to be

$$\epsilon_{total} = [1 - (1 - \epsilon_F)(1 - \epsilon_C)]\,. \tag{4.4}$$

4.3.2 Estimation of Efficiency from the Data

Year	N_{events}	N_C	N_{FC}	N_F	$\epsilon_C(\%)$	ϵ_F (%)	$\epsilon_{total}(\%)$
1990	368	306	48	5	90.6 ± 4.0	13.6 ± 1.8	91.8 ± 1.4
1991	764	155	576	32	94.7 ± 0.9	78.8 ± 1.5	98.9 ± 0.4
1992	1341	374	947	13	98.6 ± 0.4	71.7 ± 1.2	99.6 ± 0.2
Total	-	-	-	-	-	-	98.2 ± 0.3

Table 4.4: Measured trigger efficiencies.

Tagged two–photon collisions can be trigger–selected by

- an FDHIOR trigger from a tag in the Forward Detector,
- a central track and/or calorimeter trigger
  (such as the standalone triggers, see Table 3.1)
- a coincidence of triggers:
  (TBM1.OR.EBTOTLO).AND.(LCALLO.OR.RCALLO).

Independent triggers are required to calculate the trigger efficiency, so the logical .OR. of the central triggers is formed. This is called the CENTRL trigger. The logical .OR. is used because some of the central triggers are not necessarily physically independent. The triggers that contribute to this logical .OR. are listed in Table 3.1 and have the superscript ‘C’.

For each year the number of events that only fired the CENTRL trigger is called N_C, the number of events that fired the CENTRL and FDHIOR triggers is called N_{FC} and the number of events where only FDHIOR fired is called N_F. The resulting efficiencies are given in Table 4.4. The FDHIOR trigger was installed late in 1990 (run number 1839). Hence the estimated trigger efficiency for 1990 is lower than those efficiencies for 1991 and 1992.

4.4 Data Self Consistency

Distributions from 1990 (solid lines), 1991 (dashed lines) and 1992 (dotted lines) are shown in Figures 4.3 – 4.10. In each plot the data is normalised to the 1990 integrated luminosity. Each distribution has all of the analysis cuts applied except cuts on the quantites being plotted. In those cases, the cuts are represented by vertical dot–dashed lines.

Year	No. of Events	Luminosity (pb^{-1})	σ_{cuts} (pb) (Corrected)
1990	368 (220 + 148)	6.90 ± 0.06	58.1 ± 3.2
1991	764 (433 + 331)	14.34 ± 0.10	53.9 ± 2.0
1992	1341 (730 + 611)	24.69 ± 0.13	54.5 ± 1.5
Total	2473 (1383 + 1090)	45.93 ± 0.17	54.8 ± 1.1

Table 4.5: Comparison of number of events, integrated luminosities and cross–sections for the selection cuts in 1990, 1991 and 1992. The numbers in brackets indicate the numbers of events for the θ_{tag} regions of 50–70 mrad and 70–120 mrad respectively. The trigger efficiency is accounted for in the calculation of the cross–section for the cuts.

Figure 4.3 shows the tag distributions of E_{tag}/E_{beam}, θ_{tag}, Q^2 and E_{tag}/E_{beam} versus θ_{tag}. The three cuts on θ_{tag} in Figure 4.3(b) define the two θ_{tag} regions of

50–70 mrad and 70–120 mrad. The cuts on E_{tag}/E_{beam} and θ_{tag} limit a range in Q^2 to about 4–30 GeV^2 (see Figure 4.3(c)). The θ_{tag} cut at 70 mrad divides the data sample into two. For the θ_{tag} range of 50–70 mrad the mean Q^2 of the data is 6.4 GeV^2 and for the θ_{tag} range of 70–120 mrad the mean Q^2 of the data is 15.1 GeV^2.

The x and W distributions are shown in Figures 4.4 and 4.5. The calculation of x and W, with a description of the subscript labels, has been given in Section 4.1.2.

The distribution of $E_{antitag}/E_{beam}$ is shown in Figures 4.6 (a) and (b). The neutral energy distribution is shown in Figures 4.6 (c) and (d). The neutral energy is the sum of energies of the unassociated clusters in each event.

All transverse momenta are measured with respect to the beam. In each transverse momentum figure (Figures 4.7 – 4.9) the plots on the left are on a linear scale and the plots on the right are the same variable with a logarithmic scale.

The sum of p_T^{tag} and p_T^{Vin} is shown in Figure 4.7(c) and (d). Since the anti–tag condition limits the transverse momentum of the anti–tag and since the unobserved particles from the two–photon collision are forward going, then the total missing transverse momentum should be small. Therefore p_T^{Vin} should balance p_T^{tag} and adding these two variables should result in a distribution peaked close to zero. The fact that the peak is offset from zero indicates that the unmeasured system is carrying away some of the p_T. When only tracks are considered, as in Figure 4.7(a) and (b), the peak becomes more offset from zero since not all of the final state has been included in the p_T sum. The remaining p_T distributions of Figures 4.8 – 4.9 are taken normal to the plane of the tag and the beam.

The pseudorapidity distribution of individual tracks is considered. The pseudorapidity of a particle is defined as

$$\eta = -\log \tan\left(\frac{\theta}{2}\right) \tag{4.5}$$

where θ is the polar angle of the particle in the detector measured from the direction of the beam that has produced the target photon. Therefore the tag is always at the negative side of the pseudorapidity plot.

Figure 4.10(c) shows the pseudorapidity for charged tracks only. Since the tracks are only accepted for $|\cos\ \theta| < 0.95$ the track pseudorapidity limits are approximately ± 1.83. In the pseudorapidity plots there is one entry per track.

An energy flow distribution determined from tracks alone is shown in Figure 4.10(d). It has been produced by weighting each entry of the pseudorapidity distribution by the track energy.

All of the distributions are in good agreement with each other. The solid line corresponds to the 1990 dataset, which is has the lowest statistics of the three years, and therefore shows some of the biggest statistical fluctuations of the three samples.

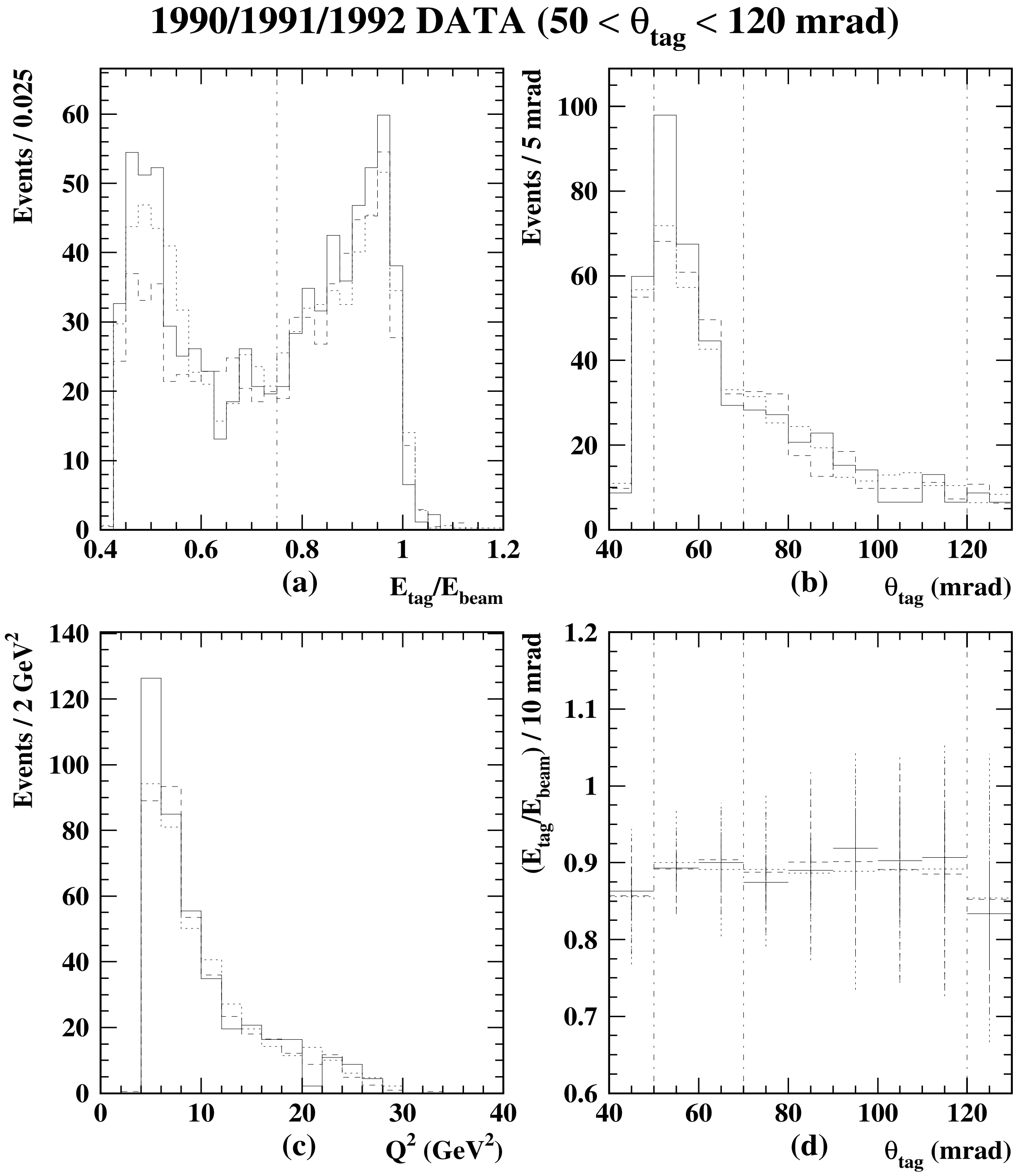

Figure 4.3: Comparison of 1990 (solid), 1991 (dashed) and 1992 (dotted) tag distributions. Final selection cuts are represented by vertical dot–dashed lines.

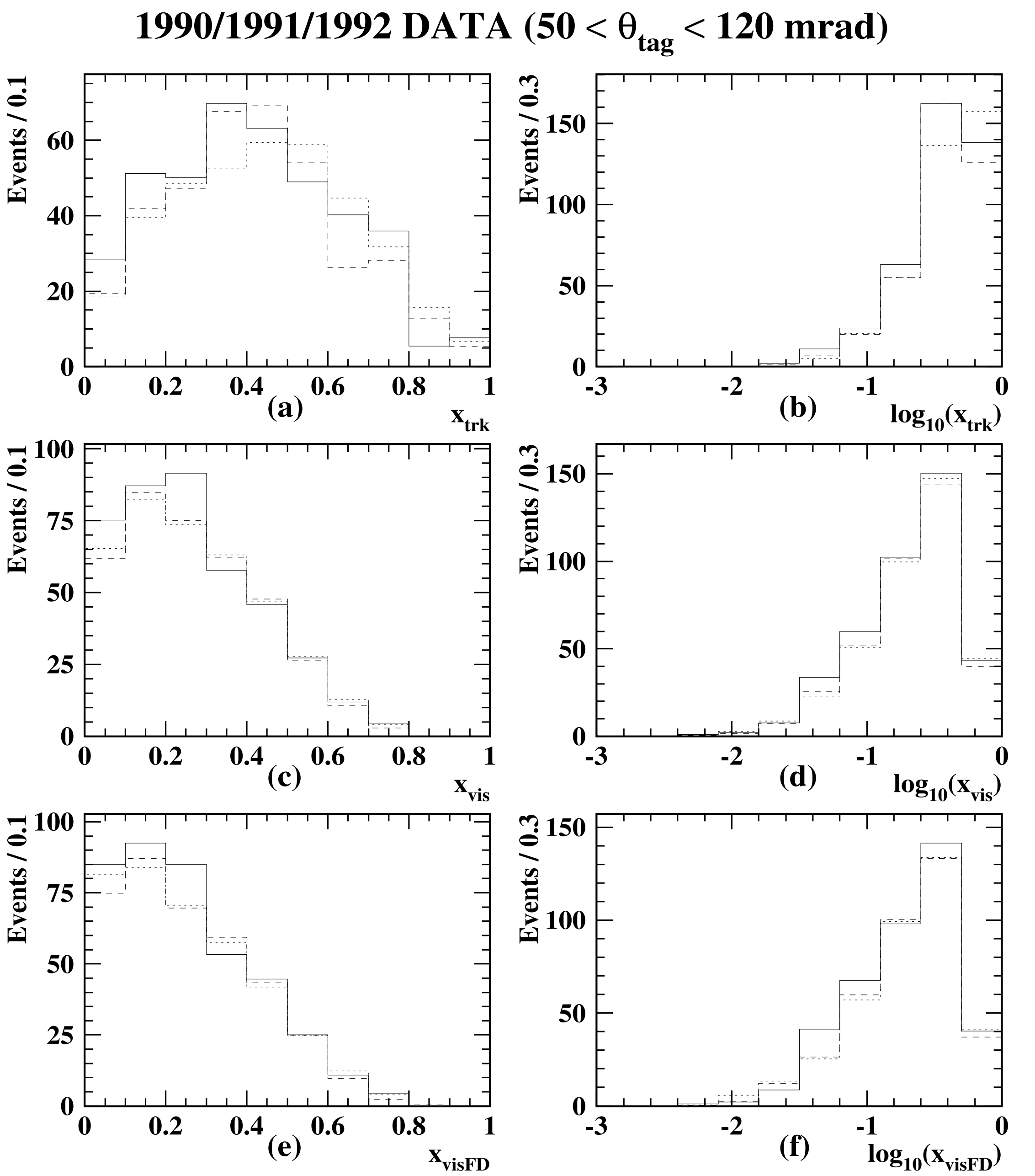

Figure 4.4: Comparison of 1990 (solid), 1991 (dashed) and 1992 (dotted) x_{trk}, x_{vis} and x_{visFD} distributions.

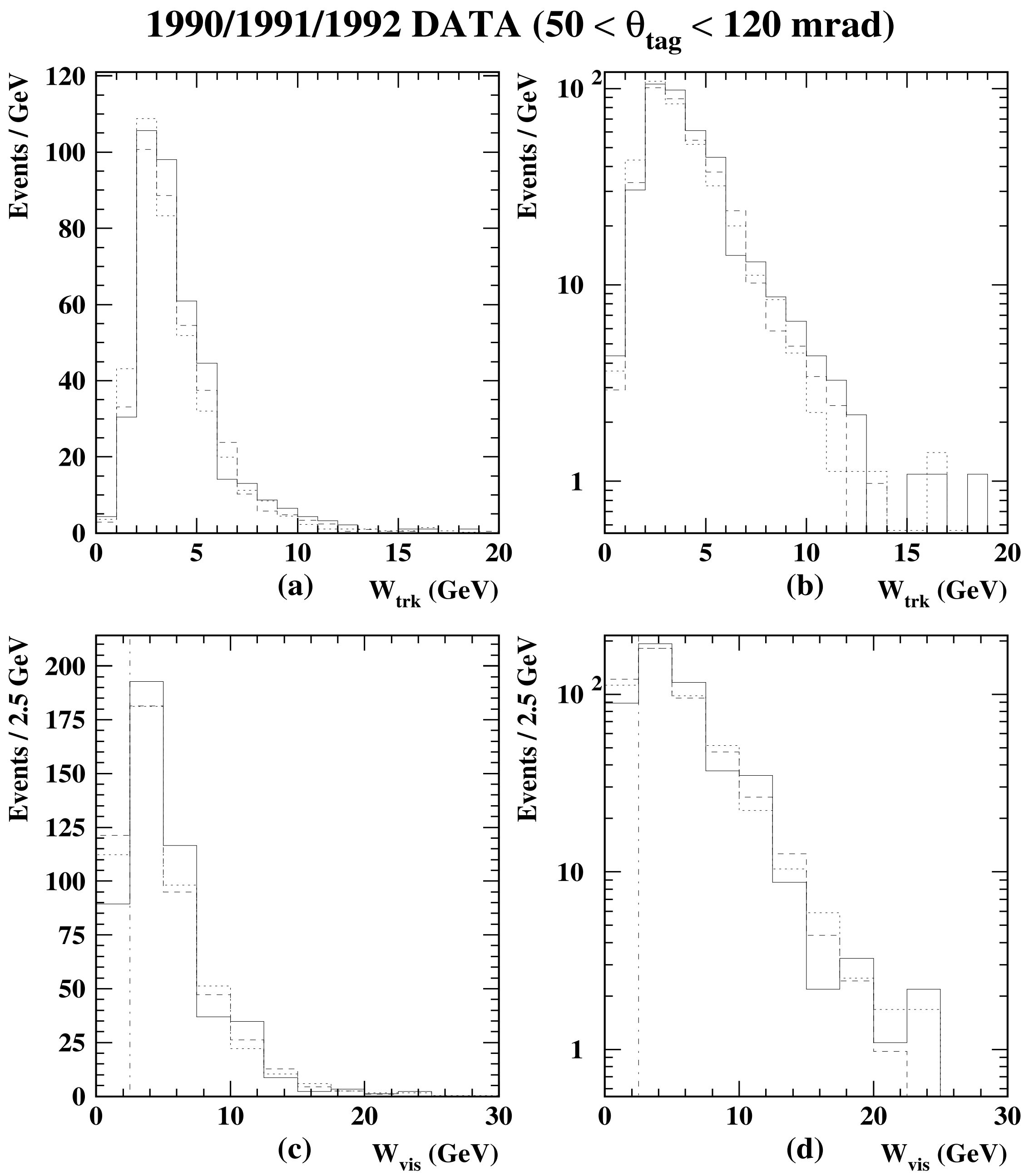

Figure 4.5: Comparison of 1990 (solid), 1991 (dashed) and 1992 (dotted) invariant mass distributions. Final selection cuts are represented by vertical dot–dashed lines.

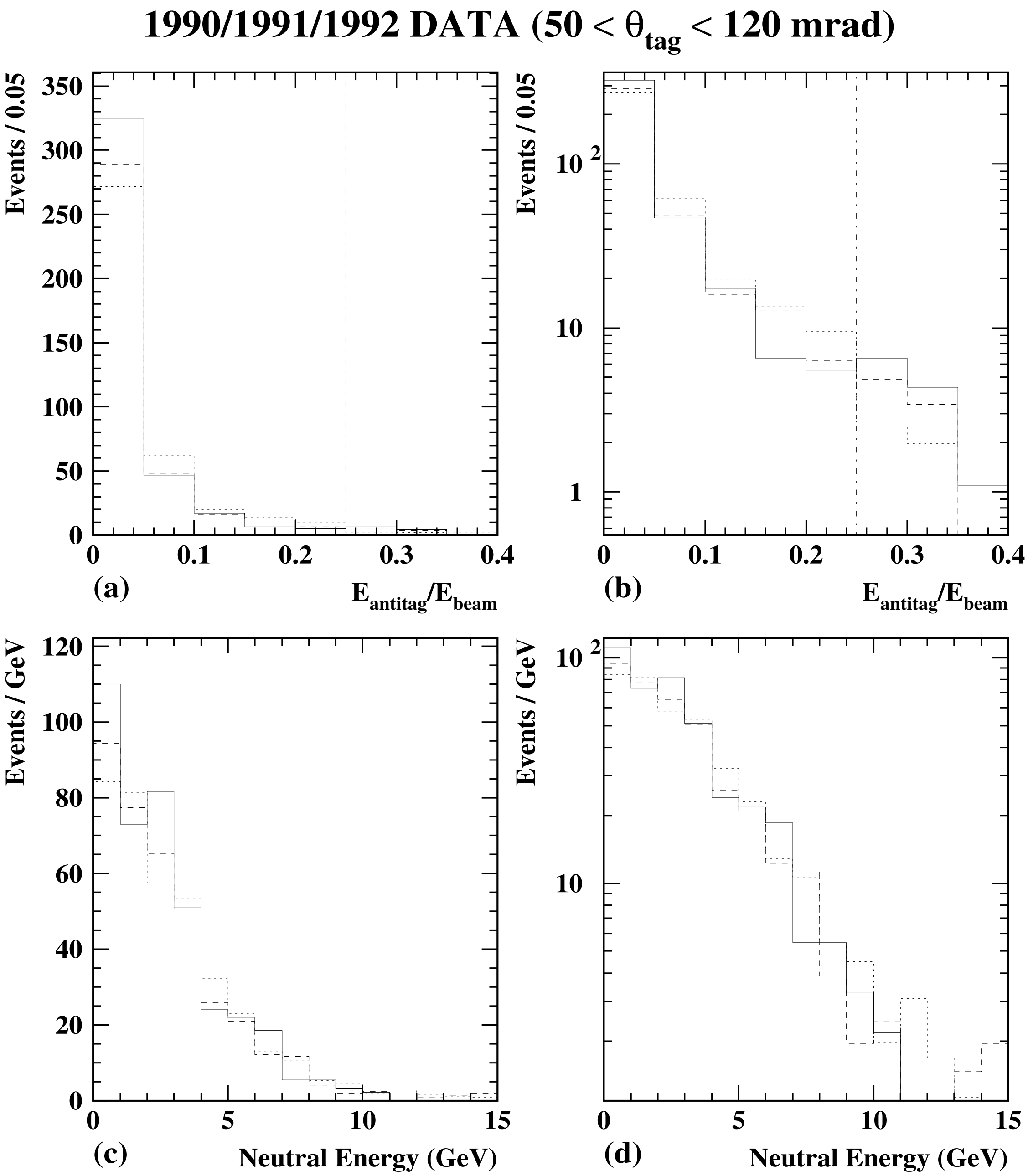

Figure 4.6: Comparison of 1990 (solid), 1991 (dashed) and 1992 (dotted) anti–tag and neutral energy distributions. Final selection cuts are represented by vertical dot–dashed lines.

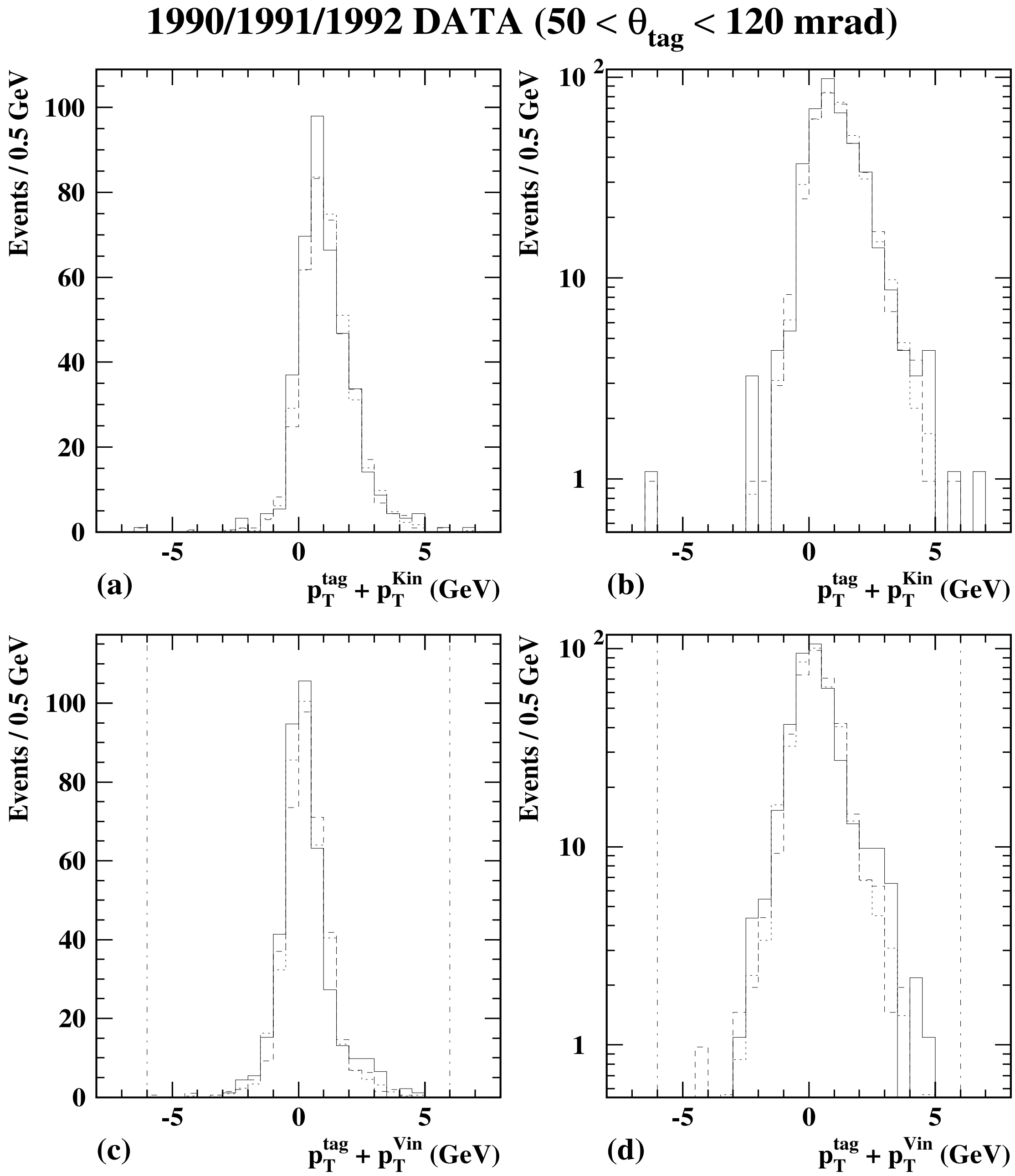

Figure 4.7: Comparison of 1990 (solid), 1991 (dashed) and 1992 (dotted) transverse momentum distributions (defined in Section 4.1.3) in the plane of the beam and the tag. Final selection cuts are represented by vertical dot–dashed lines.

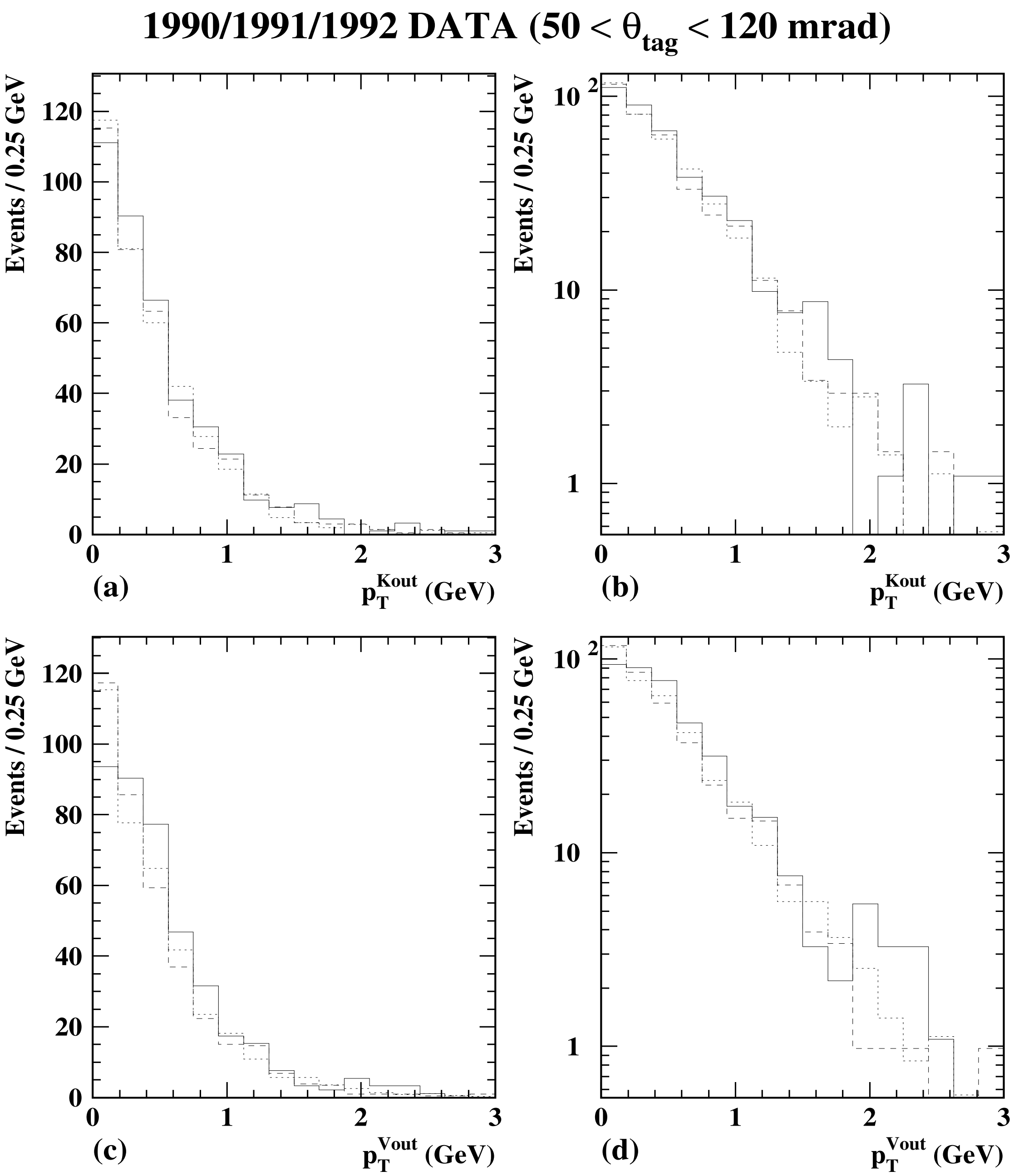

Figure 4.8: Comparison of 1990 (solid), 1991 (dashed) and 1992 (dotted) transverse momentum distributions (defined in Section 4.1.3) out of the plane of the beam and the tag.

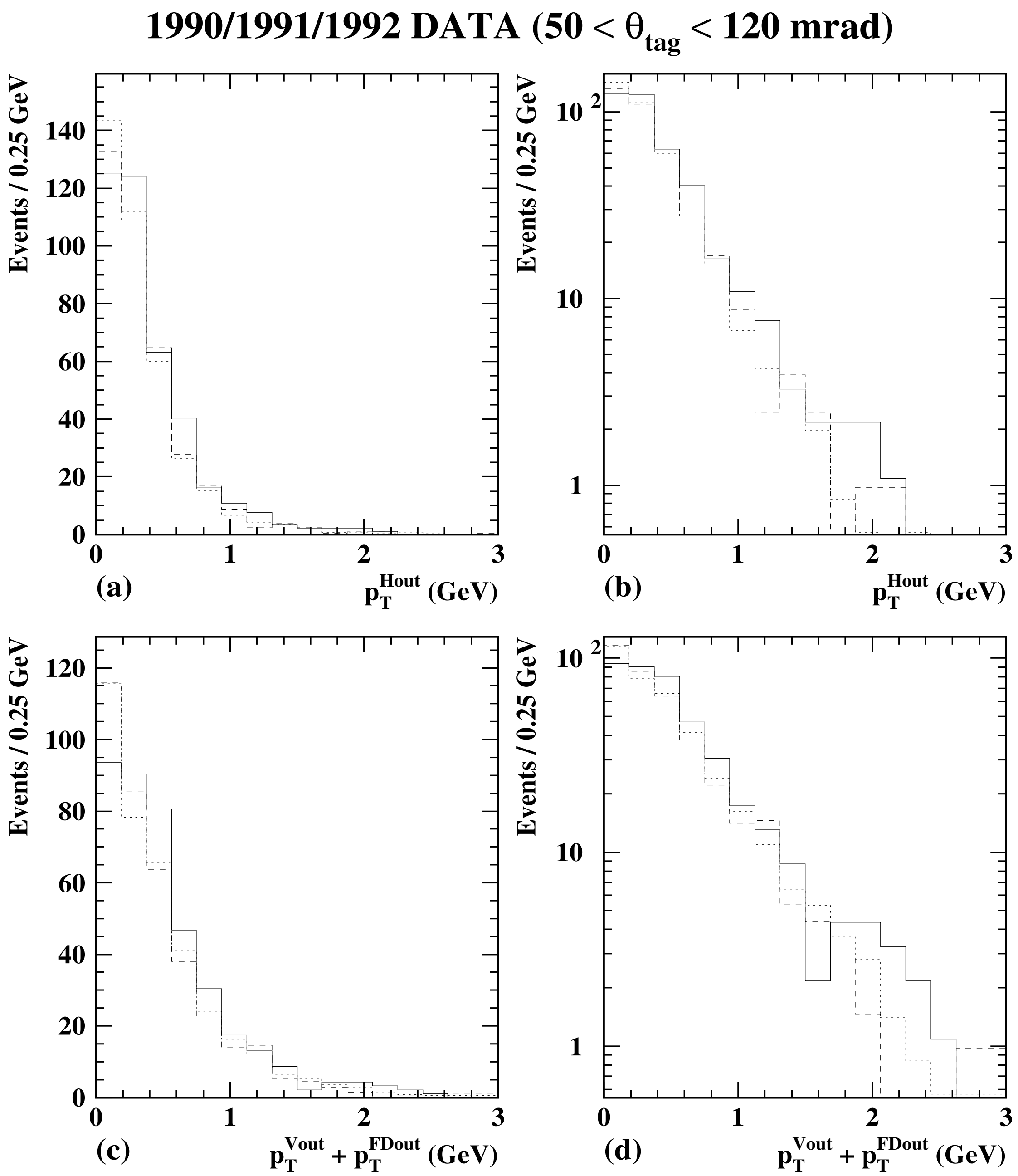

Figure 4.9: Comparison of 1990 (solid), 1991 (dashed) and 1992 (dotted) transverse momentum distributions (defined in Section 4.1.3) out of the plane of the beam and the tag.

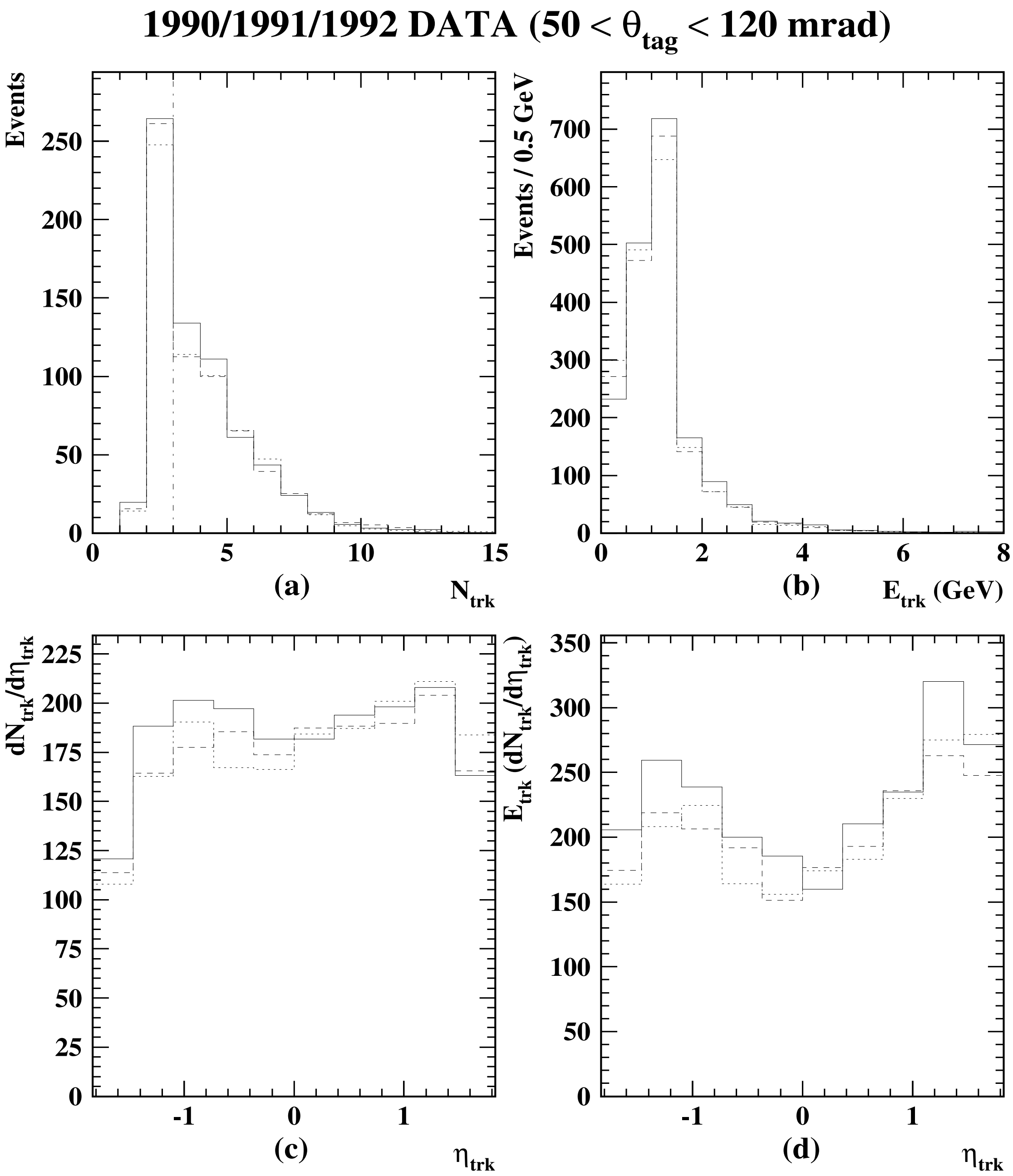

Figure 4.10: Comparison of 1990 (solid), 1991 (dashed) and 1992 (dotted) track multiplicity distributions. Final selection cuts are represented by vertical dot–dashed lines.

Chapter 5

Monte Carlo Simulation

Two-photon events generated from Monte Carlo programs are used for a number of purposes. When passed through the OPAL detector simulation, GOPAL [88], Monte Carlo events have the same event selection applied to them as is applied to the OPAL data. Data and Monte Carlo distributions can be compared and Monte Carlo can be used in the unfolding procedure to correct for the effects of finite detector acceptance and resolution. Monte Carlo samples can also be treated as data to test the unfolding algorithm.

Three Monte Carlo programs are used to generate events. These are:

- Vermaseren [89, 90, 91], a QED matrix-element program (see Section 5.2).
- F2GEN [92], which generates a $q\overline{q}$ pair in the two-photon centre of mass with a total cross-section according to a chosen formula for $F_2^{\gamma}(x, Q^2, P^2)$ or $F_2^{\gamma}(x, Q^2)$ (see Section 5.3).
- HERWIG [93], which generates events in the deep inelastic $e\gamma$ scattering mode according to a chosen set of photonic parton distribution functions. It accurately describes the perturbative phase of parton evolution, whilst also including the remnant of the struck photon in the final state (see Section 5.4).

5.1 $\gamma^*\gamma$ Fragmentation

Much use will be made of the phrase '$\gamma^*\gamma$ fragmentation', so it is defined here. The phrase describes the complete process of producing particles from the two incoming photons, one virtual (γ^*) and one real (γ). It includes the production of partons from the two photons, their spatial and momentum distributions, and the parton fragmentation to produce the final state particles.

5.2 Vermaseren

This is a QED matrix element Monte Carlo program that calculates exactly the multiperipheral process of Figure 4.2(a) and the s–channel bremsstrahlung process of Figure 4.2(c) (photon exchange only). When given quark masses, charges and colour factors it can be run as a QPM generator. It is used to generate singly–tagged $\tau^+\tau^-$ and $c\bar{c}$ events for background and unfolding studies.

5.3 F2GEN

This is a Monte Carlo program that generates events according to a chosen formula for $F_2^\gamma(x, Q^2)$. It is a modification of TWOGEN [92] which is based on the transverse–transverse two–photon luminosity generator developed by Langeveld [94]. F2GEN separates the two–photon interaction into two parts. It generates the luminosity function $L_{\gamma\gamma}$ of the two photons and then constructs the final state X of the two–photon collision. This is made possible from the assumption that the cross section for the production of a state X can be factorised [95, 96, 97] as

$$\sigma(\mathrm{e^+e^-}\to\mathrm{e^+e^-}X) = L_{\gamma\gamma}(\mathrm{e^+e^-}\to\mathrm{e^+e^-}\gamma_1^*\gamma_2^*)\ \sigma(\gamma_1^*\gamma_2^*\to X). \qquad (5.1)$$

The electron, positron and the two photons are generated using the luminosity generator. Events are accepted if they are within defined kinematic limits, such as minimum and maximum tag angle, minimum and maximum invariant mass of the two–photon system W and minimum tag energy. A quark–antiquark state of invariant mass W is then generated according to a chosen angular distribution in the two–photon centre–of–mass. The quark flavour is chosen by a $(charge)^4$ weighting. The total cross section is approximated using only the transverse–transverse (σ_{TT}) term with

$$\sigma_{TT} = \frac{4\pi^2\alpha}{Q^2} F_2^\gamma(x, Q^2, P^2). \tag{5.2}$$

Point–like Mode of $\gamma^*\gamma$ Fragmentation

For the point–like mode, the final state is simulated as $\gamma^*\gamma \to q\overline{q}$, where the quarks have the same angular distribution as the leptons in $\gamma\gamma \to l^+l^-$. The differential cross–section for the production of l^+l^- from the two *real* photons is given [98] by

$$\frac{d\sigma(\gamma\gamma \to l^+l^-)}{d\Omega^*} = \frac{\alpha^2}{W_{\gamma\gamma}^2} \beta^* \frac{2\beta^{*2} sin^2\theta^* - \beta^{*4} sin^4\theta^* + 1 - \beta^{*4}}{(1 - \beta^{*2} cos^2\theta^*)^2} \tag{5.3}$$

where θ^* is the angle that one of the leptons makes with respect to the $\gamma\gamma$ direction in the $\gamma\gamma$ centre–of–mass, $W_{\gamma\gamma}$ is the invariant mass of the photon pair, and

$$\beta^* = \sqrt{1 - \frac{4m_l^2}{W_{\gamma\gamma}^2}} \tag{5.4}$$

is the velocity of the leptons. The * in β^*, θ^* and Ω^* denotes a $\gamma\gamma$ centre–of–mass quantity and m_l is the mass of one of the produced leptons. When a quark pair is produced, m_l is replaced by the mass of the quark produced. The quark–antiquark state is allowed to shower using the parton shower model [99] and fragment using the Lund string model [100, 101].

Peripheral Mode of $\gamma^*\gamma$ Fragmentation

Not all two–photon interactions are expected to be point–like, because of the low–x and VMD processes. These result in particles having limited transverse momenta in the two–photon centre–of–mass frame. This effect is modelled in F2GEN by generating a quark–antiquark pair such that the quark p_T with respect to the $\gamma\gamma$ axis has a gaussian distribution with a half–width of 300 MeV. This scale was chosen to represent the average transverse momentum of a quark in a meson.

'Perimiss' Mode of $\gamma^*\gamma$ Fragmentation

This mode is a mixture of the point–like mode and peripheral mode, where one of these two modes is chosen based on the x and Q^2 of the generated event.

If the generated x is less than a certain small value x_0 then the event is made peripheral. This is intended to simulate the low–x behaviour of the final state. The value x_0 is chosen to coincide approximately with the onset of the low–x rise in the GRV F_2^γ parameterisation. In this work the values $x_0 = 0.1$ and $x_0 = 0.05$ are used.

If the generated x is larger than x_0 then a hit–and–miss decision is made using the ratio $F_2^\gamma(x, Q^2)$ / $F_2^{\gamma VMD}(x)$ where $F_2^\gamma(x, Q^2)$ is the structure function being used in the F2GEN generator. The purpose of this is to make the VMD portion of $F_2^\gamma(x, Q^2)$ peripheral and the remaining portion point–like. The formula used for $F_2^{\gamma VMD}(x)$ in the hit–and–miss is that of Equation 2.10. Since all of the events for $x < x_0$ are peripheral, the hit–and–miss is not active in this region.

The use of two different values of x_0 actually makes little difference to the overall degree of peripherality of the sample. This is due to the fact the the value $F_2^{\gamma VMD}$ is closer to the value of $F_2^\gamma(x, Q^2)$ at x_0 than at higher x and therefore shifting the value of x_0 down to 0.05 from 0.1 does not make many more of the events point–like.

For the comparison of data with Monte Carlo, and for unfolding, a purely point–like sample and a 'perimiss' sample with $x_0 = 0.1$ are used. These will be referred to as '100% point–like' and 'perimiss(0.1)' respectively.

5.4 HERWIG

The HERWIG event generator simulates Hadron Emission Reactions With Interfering Gluons. It includes any combination of lepton, hadron or photon scattering [93]. It is intended to be the best possible implementation of perturbative QCD [102, 103] that also includes a simple model of non-perturbative effects [104, 105], covering as many processes as possible. It gives a good description of high energy data, with few adjustable parameters, so when it is extended to two-photon collisions [106] at lower energies it should predict the data distributions well, once a few free parameters have been tuned.

Production of the Two Photons

The first step in generating a two–photon event with HERWIG is to emit a photon from each of the electron and positron beams. The Equivalent Photon Approximation (EPA) [107] is used. The limits on the photon transverse momentum and virtuality are set by the user. All of the event is then boosted to the two–photon centre–of–mass frame.

Deep Inelastic Scattering

The deep inelastic $e\gamma$ interaction as modelled in HERWIG is schematically presented in Figure 5.1 and is dealt with in the following way. Incoming and outgoing partons are evolved into jets by generating initial- and final-state parton showers. This is the perturbative phase of the $\gamma^*\gamma$ fragmentation. Once cut-offs in the perturbative evolution have been reached, non-perturbative confinement effects set in and QCD calculations switch over to the hadronisation model. The hadronisation also includes the remnant of the struck photon. Although HERWIG strongly emphasises the accurate description of the perturbative phase of parton evolution, there are theoretical ambiguities in dealing with the photon remnant.

Parton Showers in HERWIG

For both the initial and final state parton showers (ISPS and FSPS) the evolution is downwards in scale. The evolution of the final state parton shower moves outwards from the hard process towards the outgoing hadrons and stops when the generated transverse momentum is less than a global cut–off. The evolution of the initial state parton shower is backwards towards the incoming photons and stops when the evolution scale reaches a cut–off related to the structure function being used. The backward evolution algorithm [108] ensures that at each stage of branching, the parton distributions agree with the input parton distribution functions.

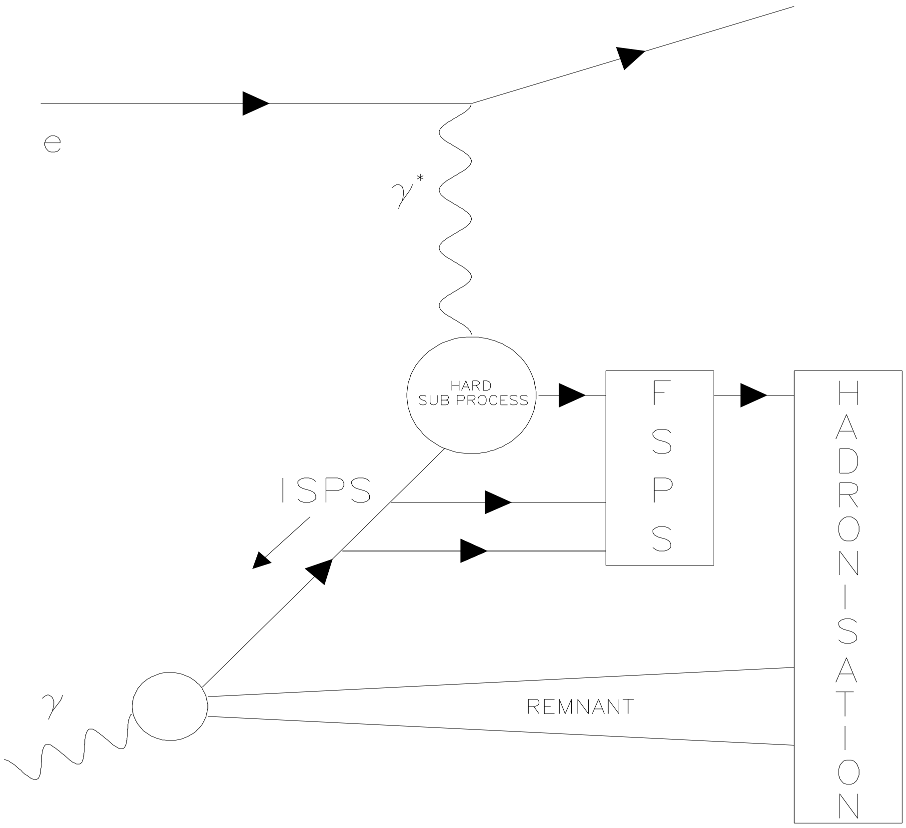

Figure 5.1: A representation of the deep inelastic $e\gamma$ scattering process in the HERWIG Monte Carlo. ISPS and FSPS are the initial and final state parton showers respectively.

The Soft Underlying Event (SUE)

In a γp collision, one parton from the photon interacts with one parton from the proton. This leaves two hadron remnants, one from the photon and the other from the proton. The generation of a soft underlying event is an option, and models a soft hadron–hadron collision between a pair of colourless clusters that contain the hadron remnants. In DIS events that are considered in this thesis, there is only one hadron remnant. When the soft underlying event option is chosen in the DIS case, the breakup of the remnant is modelled as a soft underlying event between the remnant and its nearest neighbour. There is no physical basis for a soft underlying event in DIS, but the option is never-the-less exploited in some tests of the unfolding in Chapter 7.

5.5 Comparison of Generators

To ensure that the F2GEN and HERWIG generators give the correct normalisation, they have been compared with each other, and F2GEN has been compared with the Vermaseren generator. Each sample has been generated with 100 000 events satisfying the loose cuts $E_{tag} > 20$ GeV and $40 < \theta_{tag} < 130$ mrad. The beam energy in each case was 45.6 GeV.

The following tighter cuts have been applied to the generated samples to ensure that each has accessed the same phase space, and a phase space that is similar to the one defined by the cuts made on the data:

- $E_{tag}/E_{beam} > 0.75$
- $40 < \theta_{tag} < 130$ mrad
- $W_{true} > 2.5$ GeV
- $\theta_{antitag} < 50$ mrad.

F2GEN and Vermaseren

In this comparison, F2GEN has been run with the P^2 dependent Quark Parton Model formula for F_2^γ in Equation 2.11. Both generators in this comparison have been restricted to producing $u\overline{u}$ in the final state. The light quark mass is taken to be 0.35 GeV. Each sample contains 100 000 events that satisfy the loose cuts.

F2GEN and HERWIG

These two generators have been run with the leading order GRV F_2^γ (see Section 2.7.1) for four flavours. 100 000 events satisfying the loose cuts have been generated for each sample.

Comparison Results

The cross–section results are presented in table 5.1. N_{gen} is the number of events generated with a cross–section σ_{gen} to give 100 000 events satisfying the loose cuts. N_{cuts} is the number of events that pass the tighter cuts. The cross–section σ_{cuts} is determined from the equation

$$\sigma_{cuts} = \sigma_{gen} \times \frac{N_{cuts}}{N_{gen}}. \tag{5.5}$$

The quoted error on σ_{cuts} is the fraction $(N_{cuts})^{-1/2}$ of σ_{cuts}.

It is usual to assume that the Vermaseren generator produces the correct cross–section, since the program uses the QED matrix element to calculate exactly the multiperipheral cross–section. The F2GEN cross–section is lower than the Vermaseren cross–section by 5.4 $\pm$ 0.7 %. F2GEN has been found to have a cross–section that is 2.3 $\pm$ 0.8 % lower than the corresponding HERWIG cross–section. HERWIG has not been compared directly to Vermaseren, because of difficulties in running both of them with similar conditions. The cross–section shifts should be one of the systematic errors in a final F_2^γ result. However, for the purpose of this thesis, the agreement between the cross–sections of the generators is good.

Generator	N_{gen}	σ_{gen} (pb)	N_{cuts}	σ_{cuts} (pb)
Vermaseren	2 058 864	1805.24	40 449	35.47 $\pm$ 0.18
F2GEN $F_2^{QPM}(x, Q^2, P^2)$	189 197	159.2	39 978	33.64 $\pm$ 0.17
F2GEN $F_2^{GRV}(n_f = 4)$	210 301	487.7	33 363	77.37 $\pm$ 0.42
HERWIG $F_2^{GRV}(n_f = 4)$	399 573 (/2)	410.0	38 557	79.13 $\pm$ 0.40

Table 5.1: Results of the comparison of Vermaseren, F2GEN and HERWIG.

5.6 Monte Carlo Samples Generated

Details of the Monte Carlo samples generated for use in the comparison of data with Monte Carlo (see Chapter 6) and for unfolding tests (see Chapter 7) are given in Table 5.2. There are several points to note concerning this table:

- N_{GOPAL} is the number of generated events that have been passed through GOPAL (the OPAL detector simulation program). It is equivalent to the number of generated events that have passed the loose generator cuts. The same version of ROPE (the OPAL event reconstruction program) is applied to both the output of GOPAL and the data.

- All of the samples have $Q^2 > 1$ GeV^2 and $40 < \theta_{tag} < 130$ mrad at generator level.

- In addition to the Q^2 and θ_{tag} cuts, the Vermaseren $c\bar{c}$ events have passed the loose generator cuts of $E_{tag} > 20$ GeV and $W_{true} > 4.3$ GeV.

- In addition to the Q^2 and θ_{tag} cuts, the Vermaseren $\tau^+\tau^-$ events have passed the loose generator cuts of $E_{tag} > 20$ GeV and $W_{true} > 3.6$ GeV.

- In addition to the Q^2 and θ_{tag} cuts, the remaining F2GEN and HERWIG samples have passed the loose generator cuts of $E_{tag} > 20$ GeV and $W_{true} >$ 2.0 GeV, with the exception of F2GEN Perimiss (0.05) and HERWIG GRV without the SUE, which both have $E_{tag} > 28$ GeV.

- The integrated luminosity corresponds to the number of events that have passed through GOPAL.

- N_{cuts} is the number of events that have passed the full selection cuts described in Chapter 4. The cross–sections for these cuts, called σ_{cuts}, are given in the fourth column. The number outside the brackets corresponds to the cross–section for the cuts with the whole θ_{tag} range of 50–120 mrad. It is the sum of the two numbers in the brackets, which show the cross-sections for the low (50–70 mrad) and high (70–120 mrad) θ_{tag} ranges respectively.

Sample	N_{GOPAL}	Integrated Lumi (pb^{-1})	No. passing final cuts	σ_{cuts} (pb)
Vermaseren				
$c\bar{c}$	9000	493.70	3249	6.6 $\pm$ 0.1 (3.2 + 3.4)
$\tau^+\tau^-$	10 000	333.88	743	2.2 $\pm$ 0.1 (1.0 + 1.2)
F2GEN				
GRV ($n_f = 3$)				
100% Point–like	49 000	243.73	9675	39.7 $\pm$ 0.4 (23.4 + 16.3)
Perimiss (0.1)	50 000	246.28	9313	37.8 $\pm$ 0.4 (22.0 + 15.8)
Perimiss (0.05)	39 000	224.6	8099	36.1 $\pm$ 0.4 (21.0 + 15.1)
HERWIG				
GRV ($n_f = 4$)				
With SUE	25 000	123.6	6088	49.3 $\pm$ 0.6 (28.1 + 21.2)
No SUE	55 000	290.3	13 042	44.9 $\pm$ 0.4 (24.7 + 20.3)
LAC1 ($n_f = 4$)				
With SUE	29 000	128.2	8055	62.8 $\pm$ 0.7 (35.4 + 27.5)
No SUE	23 000	98.7	5792	58.7 $\pm$ 0.8 (32.0 + 26.7)
DATA				
	-	45.93	2518	54.8 $\pm$ 1.1 (30.7 + 24.2)

Table 5.2: Monte Carlo generated samples that have had the full OPAL detector simulation (GOPAL) applied to them. The data have been included at the bottom of the table for comparison with the Monte Carlo. The numbers in brackets indicate the cross–sections for the θ_{tag} regions of 50–70 mrad and 70–120 mrad respectively.

Chapter 6

Comparison of Data with Monte Carlo

In this chapter the central problem in measuring the photon structure function will become apparent. The method of determining $F_2^\gamma(x)$ from the data is to compare the x_{vis} distribution of the data with the x_{vis} distribution of the Monte Carlo where the $F_2^\gamma(x)$ used to generate the events is known. It will be demonstrated that the Monte Carlo x_{vis} distribution is also affected by the choice of model used to describe the $\gamma^*\gamma$ fragmentation in the generator (see Sections 5.3 and 5.4 for a description of the different $\gamma^*\gamma$ fragmentation models used in this chapter). Thus, conclusions concerning $F_2^\gamma(x)$ from the data are model dependent.

To begin with, the Monte Carlo models used in the comparison are commented on. Some variables associated with the tag are then examined. These are, to some extent, independent of the final state and should be described well by Monte Carlo. Further variables, such as invariant masses, cluster energies, transverse momenta, track multiplicities and track energies are compared to see if the data can distinguish between the $\gamma^*\gamma$ fragmentation models used.

6.1 Monte Carlo Models in the Comparison

Monte Carlo samples from F2GEN and HERWIG are compared in two ranges of θ_{tag}. Since there is also an E_{tag} cut, this is effectively a comparison in two bands of Q^2. Except for the tag variables, the comparison is made separately in each θ_{tag} region. For the samples generated by F2GEN the data are compared with the Monte Carlo sum of

$$GRV(n_f = 3)\ [F2GEN] + c\overline{c}\ [VERMASEREN] + \tau^+\tau^-\ [VERMASEREN].$$

For the samples generated by HERWIG, the data are compared with the Monte Carlo sum of

$$GRV(n_f = 4)\ [HERWIG] + \tau^+\tau^-\ [VERMASEREN].$$

Each contribution to the Monte Carlo sum is individually normalised to the experimental integrated luminosity. Each distribution is plotted with all of the analysis cuts applied both to the data and the Monte Carlo, except for cuts made on the quantity being plotted. These cuts are represented by vertical dot–dashed lines on the plots. A total of four Monte Carlo samples appear in Figures 6.1–6.17. The 3–flavour GRV structure function has been used to generate a sample of events where the $q\overline{q}$ in the final state has a 100% point–like angular distribution. When this is added to the $\tau^+\tau^-$ and $c\overline{c}$ contributions from Vermaseren, this forms the solid line. The dashed line differs from this only in that the $q\overline{q}$ system in F2GEN is partly peripheral ('perimiss' where all events with $x < 0.1$ are peripheral). The HERWIG samples are generated for four flavours, so only the Vermaseren $\tau^+\tau^-$ contribution is added to these samples. Both HERWIG samples are without the soft underlying event (SUE). The dotted line is the HERWIG/Vermaseren sum when the GRV structure function is used and the dot–dashed line is the HERWIG/Vermaseren sum when the LAC1 structure function is used.

None of the Monte Carlo samples have had parameters fixed by fitting to this data sample, unlike in [34]. The aim of this comparison is to see how well the shape of data distributions are described by the Monte Carlo models and to see if any differences can be seen between the Monte Carlo models after detector simulation and analysis cuts.

All variables used in the comparison are defined in Chapter 4. In all of the plots the dot–dashed distribution is higher than all of the other Monte Carlo distributions.

This is because it has been produced with the LAC1 structure function, which has a bigger cross section than the GRV structure function. (This can be seen from σ_{cuts} for LAC1 in Table 5.2).

6.2 Data and Monte Carlo Distributions

Tag Distributions

Distributions for the tag are shown in Figure 6.1. Unlike the other distributions in the comparisons, these plots are for the complete θ_{tag} range of 50–120 mrad. The distributions in E_{tag}/E_{beam}, θ_{tag} and Q^2 shown in Figure 6.1(a), (b) and (c) show that the tagged leptons are reasonably well described within the range of these models. The disagreement between the data and the simulation at low tag energy in Figure 6.1(a) are caused by backgrounds in the data (see Section 4.2). Below the 50 mrad cut there is a large discrepancy between the data and all of the Monte Carlo models, which is the motivation for placing the minimum θ_{tag} cut at 50 mrad. The source of this discrepancy is unknown, although it might be because the detector response has been tuned to match the sample of Bhabha events which have a different θ distribution. Figure 6.1(d) shows that the Monte Carlo and the data have similar forward detector calibration.

x and W Distributions

The comparison of the x distributions of the data and Monte Carlo should reveal the actual photon structure function of the data. Distributions of x (Figures 6.2 and 6.3) and W (Figures 6.4 and 6.5) are shown for the low and high θ_{tag} regions respectively.

Although the visible x is not the true x, one should be able to anticipate the shape and size of $F_2^\gamma(x)$ from the data when the visible x distribution is compared with Monte Carlo. Strictly, such a conclusion about the data $F_2^\gamma(x)$ should be made by applying an unfolding algorithm (see Chapter 7). In doing such a comparison one assumes that the differences in shape of the x distributions are due only to different photon structure functions in the data and the Monte Carlo models.

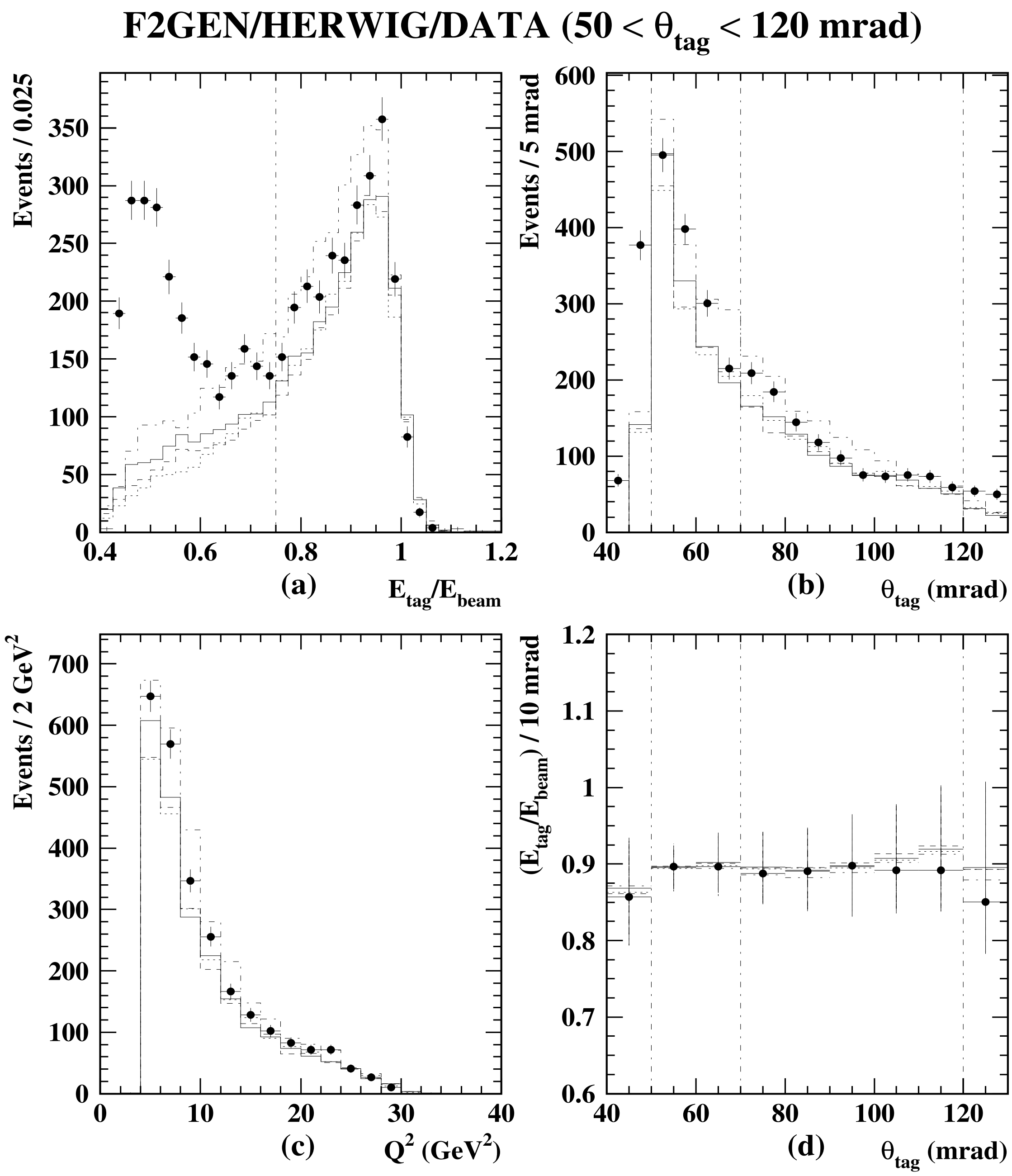

Figure 6.1: Tag distributions for the data (dots) and the Monte Carlo models in the whole θ_{tag} range. The different samples are from F2GEN GRV 100% point–like (solid), F2GEN GRV 'perimiss(0.1)' (dashed), HERWIG GRV without the SUE (dotted) and HERWIG LAC1 without the SUE (dot–dashed).

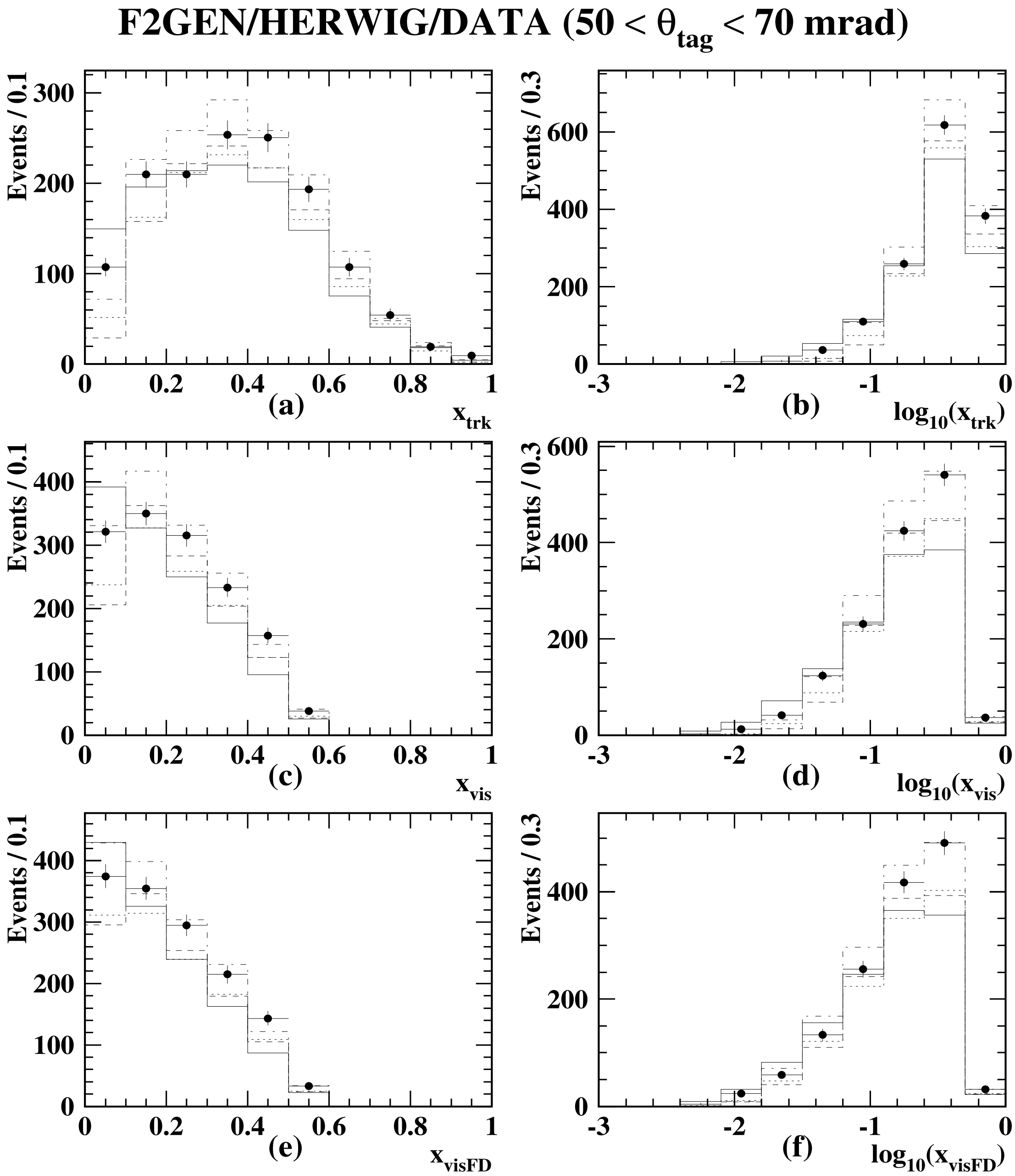

Figure 6.2: x_{trk}, x_{vis} and x_{visFD} distributions (each defined in Section 4.1.2) for the data (dots) and the Monte Carlo models in the low θ_{tag} range. The different samples are from F2GEN GRV 100% point–like (solid), F2GEN GRV 'perimiss(0.1)' (dashed), HERWIG GRV without the SUE (dotted) and HERWIG LAC1 without the SUE (dot–dashed).

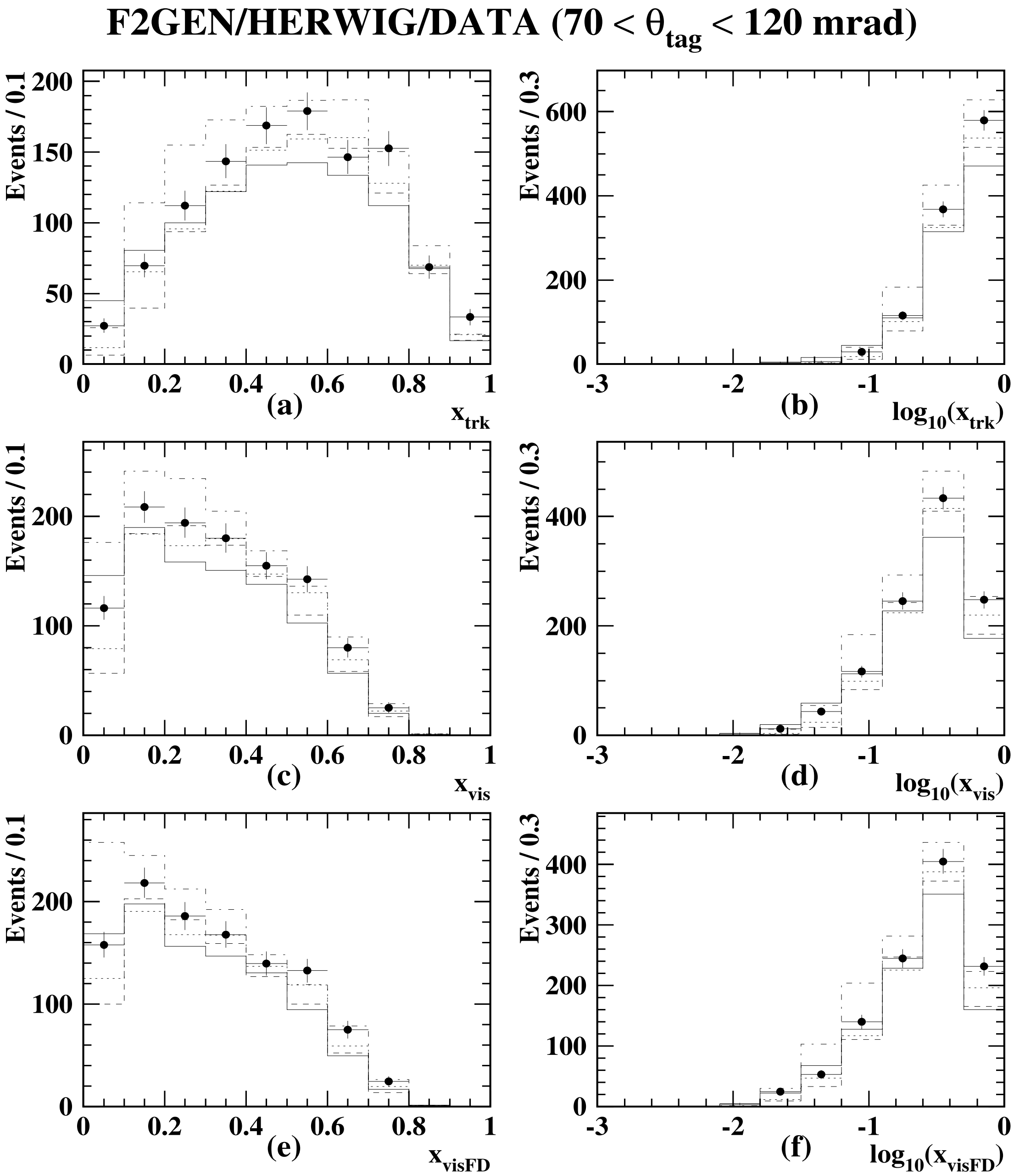

Figure 6.3: x_{trk}, x_{vis} and x_{visFD} distributions (each defined in Section 4.1.2) for the data (dots) and the Monte Carlo models in the high θ_{tag} range. The different samples are from F2GEN GRV 100% point–like (solid), F2GEN GRV 'perimiss(0.1)' (dashed), HERWIG GRV without the SUE (dotted) and HERWIG LAC1 without the SUE (dot–dashed).

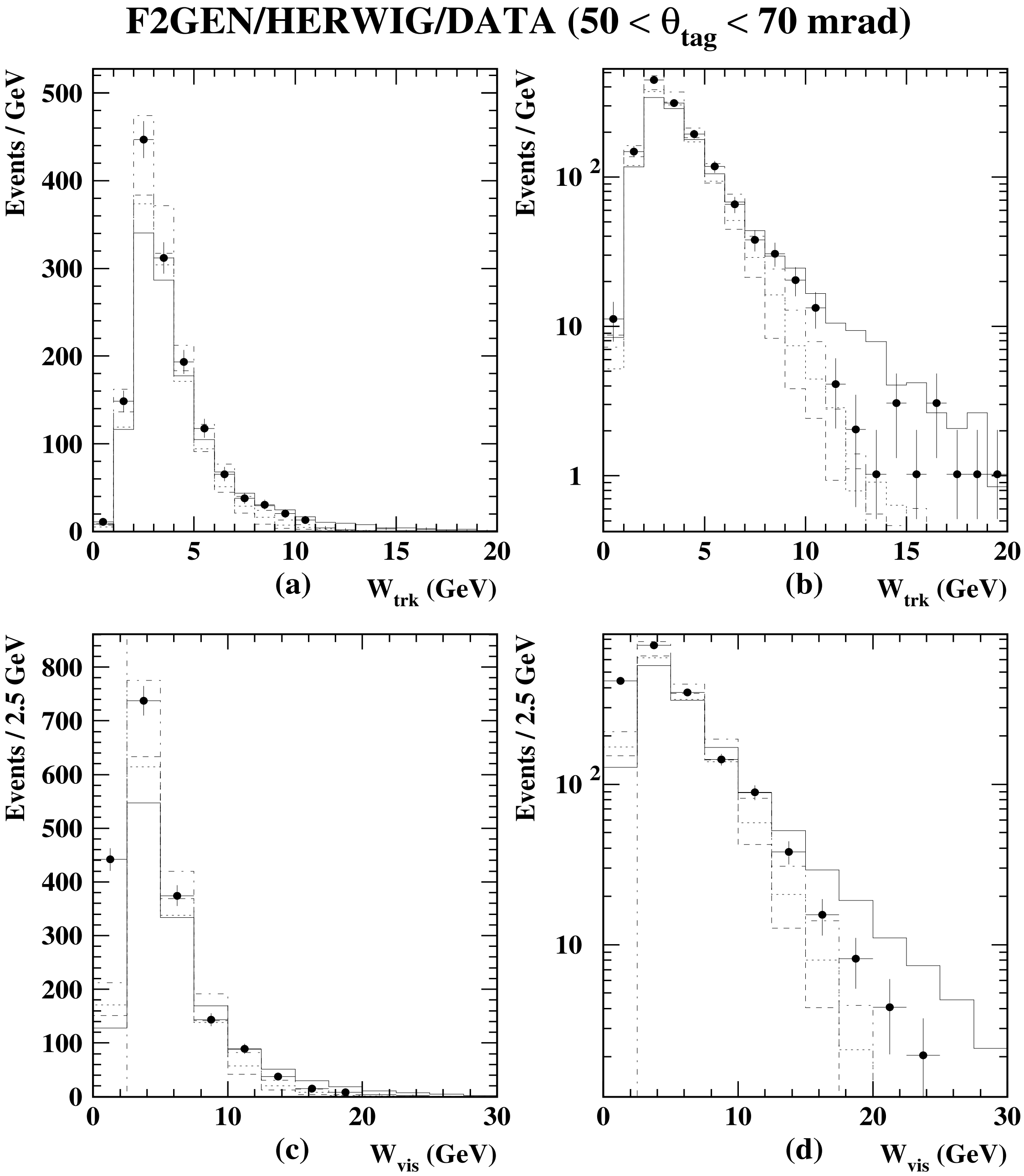

Figure 6.4: Invariant mass distributions for the data (dots) and the Monte Carlo models in the low θ_{tag} range. The different samples are from F2GEN GRV 100% point–like (solid), F2GEN GRV 'perimiss(0.1)' (dashed), HERWIG GRV without the SUE (dotted) and HERWIG LAC1 without the SUE (dot–dashed).

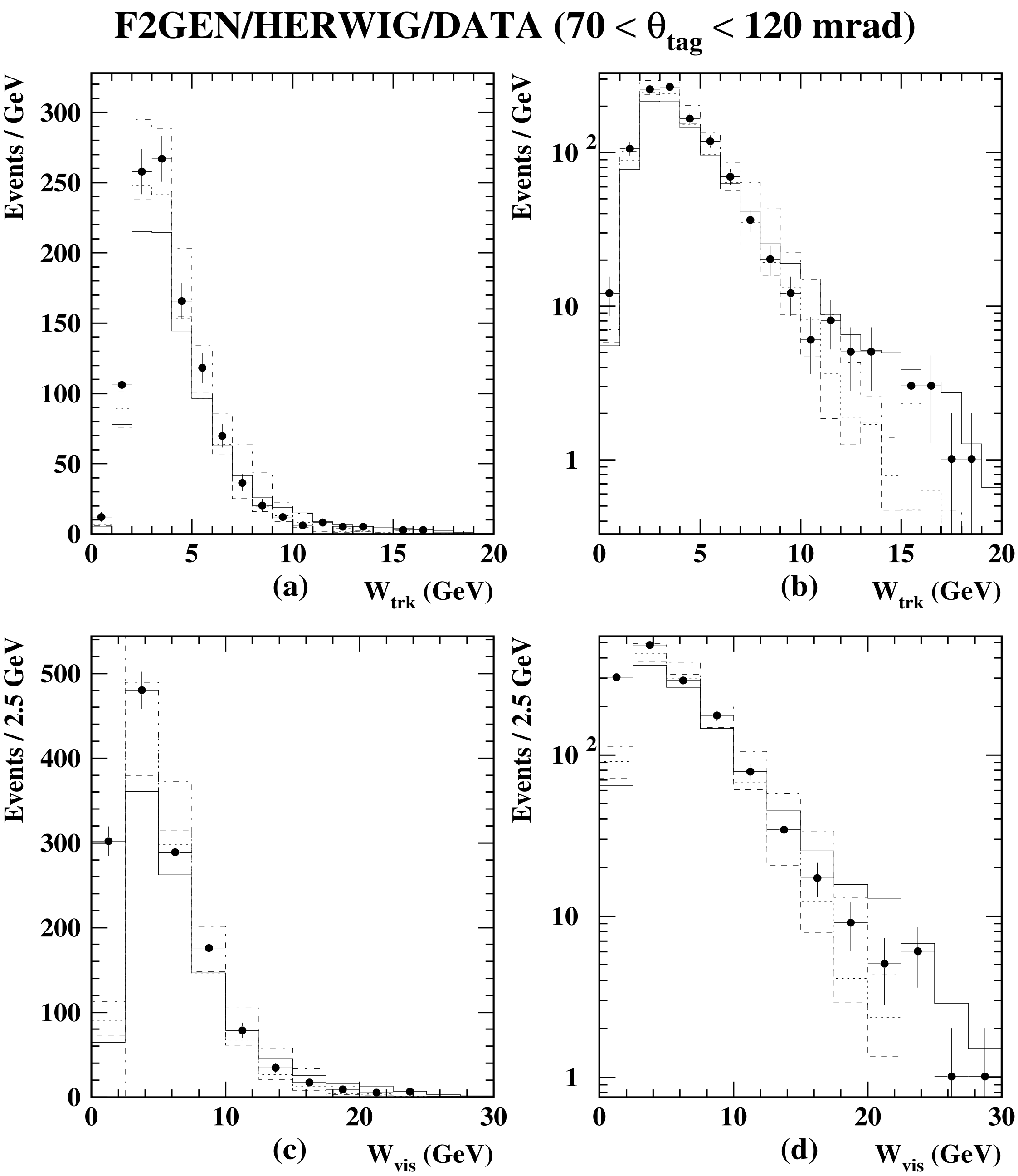

Figure 6.5: Invariant mass distributions for the data (dots) and the Monte Carlo models in the high θ_{tag} range. The different samples are from F2GEN GRV 100% point–like (solid), F2GEN GRV 'perimiss(0.1)' (dashed), HERWIG GRV without the SUE (dotted) and HERWIG LAC1 without the SUE (dot–dashed).

However, the solid, dashed and dotted lines in Figures 6.2 and 6.3 show that the resulting Monte Carlo visible x distributions differ when the *same* $F_2^\gamma(x)$ has been used to generate events with different $\gamma^*\gamma$ fragmentation models. Therefore, part of the systematic error in a final unfolded result will be due to the choice of the $\gamma^*\gamma$ fragmentation model.

A shape comparison of the GRV 100% point–like x_{visFD} distributions (solid lines) with the data distributions show that there are more Monte Carlo events than data events at low x_{visFD} and fewer at high x_{visFD}. If this was used as an unfolding Monte Carlo one would expect an $F_2^\gamma(x)$ result which is below the GRV expectation at low x and above it at higher x. The unfolded result would also reflect the fact that there are more events in the data than in the Monte Carlo by having an unfolded $F_2^\gamma(x)$ that represents a bigger cross section than the GRV parameterisation of $F_2^\gamma(x)$. The same trends are visible in the x_{vis} and x_{trk} distributions.

The GRV 'perimiss' x_{visFD} distributions (dashed lines) show the opposite effect. There are fewer Monte Carlo events than data events at low x_{visFD} and more at high x_{visFD}. Using this as an unfolding Monte Carlo one would expect an $F_2^\gamma(x)$ result which is above the GRV expectation at low x and below it at higher x, before the effects of normalisation.

HERWIG should have a more realistic $\gamma^*\gamma$ fragmentation model than F2GEN, so one may wish to use HERWIG as an unfolding Monte Carlo instead of F2GEN. The GRV sample without the SUE (dotted lines) is quite similar in shape to the data x_{visFD} distributions and one might therefore expect an unfolded $F_2^\gamma(x)$ to be very similar to the GRV $F_2^\gamma(x)$. The HERWIG LAC1 sample lies above the data at low x_{visFD}, so relative to this sample, $F_2^\gamma(x)$ from the data would not rise as much as LAC1 at low x which is consistent with the result expected if the data is unfolded with the HERWIG GRV sample.

Since the use of the same $F_2^\gamma(x)$ (i.e. the same x_{true} distribution) has produced three different visible x distributions corresponding to three different $\gamma^*\gamma$ fragmentation models, another way of thinking about the $\gamma^*\gamma$ fragmentation modelling is in terms of the x_{vis}/x_{true} correlation profile histograms. If all of the final state particles were observed with perfect detector acceptance and resolution, events would lie on the diagonal of an x_{vis}/x_{true} plot. Different $\gamma^*\gamma$ fragmentation models, combined with effects of finite detector acceptance and resolution, lie on different ‘lines’ in an x_{vis}/x_{true} profile histogram. Such profile histograms are shown in Figures 6.6 and 6.7. The 100% point–like process (solid line, closed circles) produces the most activity in the detector, because this type of $\gamma^*\gamma$ fragmentation produces higher p_T particles than the other types of $\gamma^*\gamma$ fragmentation models. With the 100% point–like process, relatively little is lost outside the acceptance region. This $\gamma^*\gamma$ fragmentation model therefore lies closest to the diagonal line. The ‘perimiss’ model (dashed line, open circles) produces the extreme opposite effect where x smears the most. HERWIG with the SUE (dot–dashed line, open squares) and without the SUE (dotted line, closed squares) lie in between these extreme F2GEN models. (Note that in the x_{vis}/x_{true} correlation plots the dot–dashed lines represent HERWIG GRV with the SUE whereas in all of the other distributions in this chapter the dot–dashed lines represent HERWIG LAC1 without the SUE).

Progress must now be made with some caution, as one can very easily arrive at a conclusion about $F_2^\gamma(x)$ that is biased in some way. The x_{vis} distributions show that the source of the shape differences between the data and the Monte Carlo are ambiguous. A shape difference can arise from either the Monte Carlo incorrectly modelling the $\gamma^*\gamma$ fragmentation or the $F_2^\gamma(x)$ in the Monte Carlo being different from that of the real $F_2^\gamma(x)$. Clearly the data has to be compared with Monte Carlo to find which of the $\gamma^*\gamma$ fragmentation models best describes the data.

This is a difficult problem, as all distributions are affected both by the $F_2^\gamma(x)$ and the $\gamma^*\gamma$ fragmentation model. It now becomes apparent why one of the $\gamma^*\gamma$ fragmentation models used in the comparison is purely point-like in nature. We know that this should be unphysical, since the low x and hadronic components of photon structure result in non point–like final states. Therefore one should be able to rule out the pure point–like sample by comparison with the data. Yet, from the x_{vis} distribution alone, the possibility that the data is purely point–like cannot be ruled out, as the difference in the shape of the data and the 100% point–like Monte Carlo may be due to different photon structure functions only. Similar arguments apply to the other Monte Carlo samples. All distributions to be considered suffer from the same problem. However, since it is known how the Monte Carlos model the $\gamma^*\gamma$ fragmentation, one can at least search for the variables which show the greatest sensitivity to different $\gamma^*\gamma$ fragmentation models.

The W distributions for the data and the Monte Carlos not surprisingly reflect

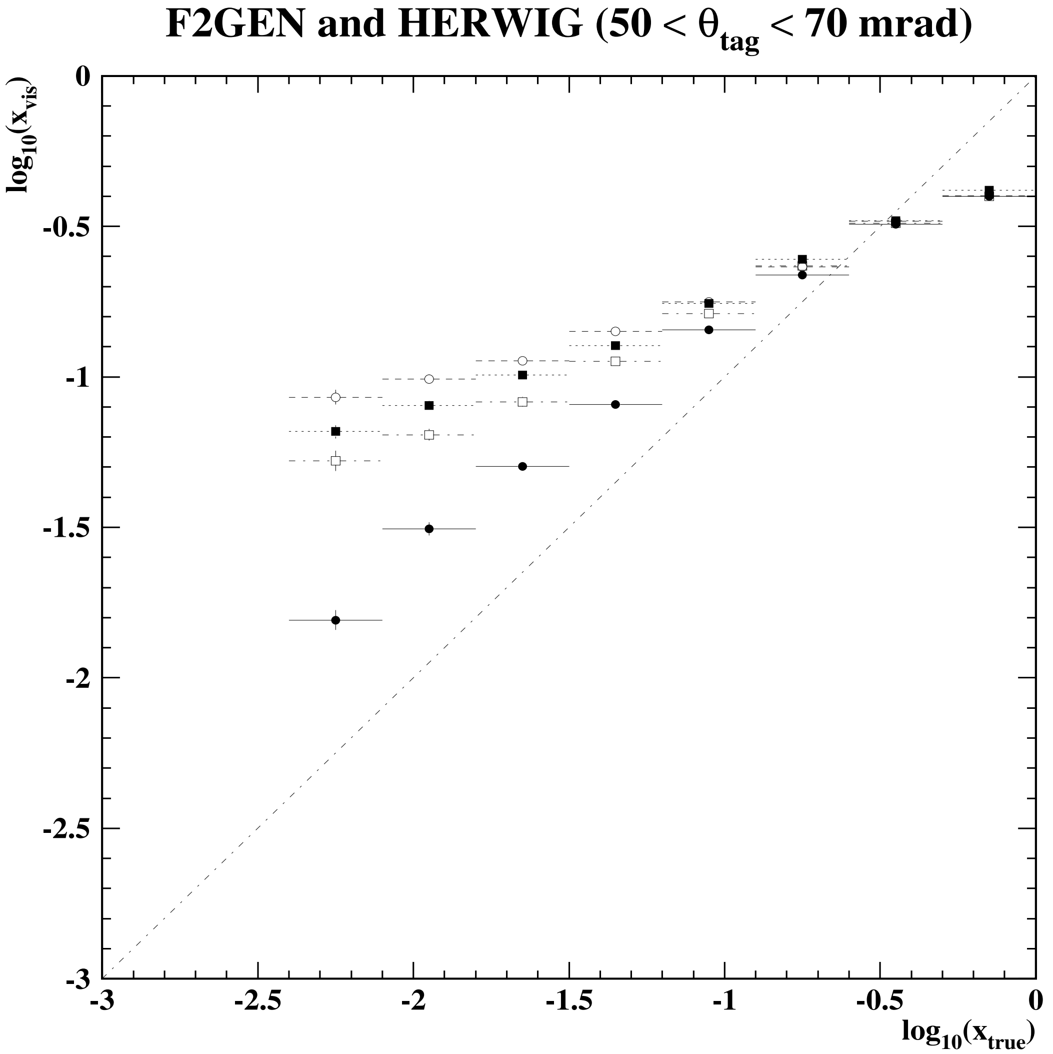

Figure 6.6: x_{vis}/x_{true} correlation plots from the F2GEN and HERWIG Monte Carlo models in the low θ_{tag} range. The different samples are from F2GEN GRV 100% point–like (solid lines, closed circles), F2GEN GRV 'perimiss(0.1)' (dashed lines, open circles), HERWIG GRV without the SUE (dotted lines, closed squares) and HERWIG GRV with the SUE (dot–dashed lines, open squares).

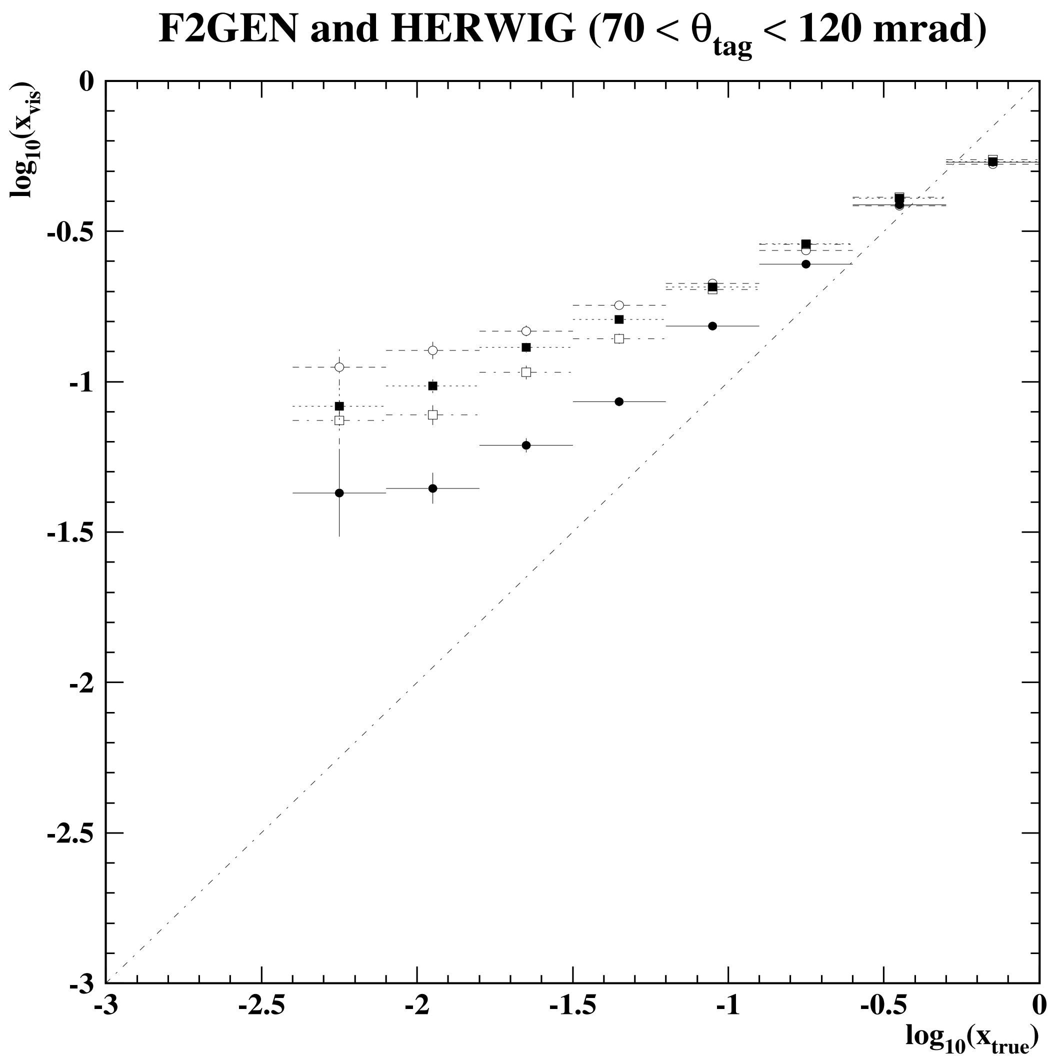

Figure 6.7: x_{vis}/x_{true} correlation plots from the F2GEN and HERWIG Monte Carlo models in the high θ_{tag} range. The different samples are from F2GEN GRV 100% point–like (solid lines, closed circles), F2GEN GRV 'perimiss(0.1)' (dashed lines, open circles), HERWIG GRV without the SUE (dotted lines, closed squares) and HERWIG GRV with the SUE (dot–dashed lines, open squares).

the trends in the x distributions, since W is so closely related to x (Equation 1.7). Different $\gamma^*\gamma$ fragmentation models mostly effect low x and high W.

Cluster Energy Distributions

The $E_{antitag}/E_{beam}$ distributions are shown in Figure 6.8(a) and (b) and Figure 6.9(a) and (b). The cut on events with $E_{antitag}/E_{beam} > 0.25$ is designed to remove double–tagged events which would appear as a small peak in the $E_{antitag}/E_{beam}$ plots at $E_{antitag}/E_{beam} \simeq 1$. In addition to the electromagnetic endcap and barrel clusters, $E_{antitag}$ also uses cluster information from the Forward Detector calorimeter (FK) and the gamma catcher (FE). The shapes of the distributions of $E_{antitag}/E_{beam}$ at low values are mostly affected by the final state, since every event has some activity in the hemisphere opposite to the tag, but few of them have a true anti–tag.

The neutral energy distribution is the total energy of all unassociated electromagnetic clusters in the barrel and endcap regions only. The distribution is shown in Figure 6.8(c) and (d) and Figure 6.9(c) and (d).

Transverse Momentum Distributions

The transverse momentum variables are defined in Section 4.4. Figures 6.10–6.15 show various transverse momentum distributions. The p_T distributions of Figures 6.12– 6.15 are taken normal to the plane of the tag and the beam. This component of p_T should be more sensitive to different final states than the p_T distributions in the plane of the tag and the beam (Figures 6.10– 6.11) because the component normal to the plane is independent of the momentum imparted to the hadronic system by the probe photon.

All of the transverse momentum distributions are consistent in their behaviour. The 100% point–like sample (solid line) is separated from the other three samples. It is very difficult to distinguish any separation in the remaining models. This behaviour comes through most clearly in the tails of the track distributions (Figures 6.10(b) – 6.14(b)). The separation is less prominent in the high θ_{tag} track distributions than in the low θ_{tag} track distributions. For both θ_{tag} ranges the switch to using charged and neutral particles rather than just charged parti-

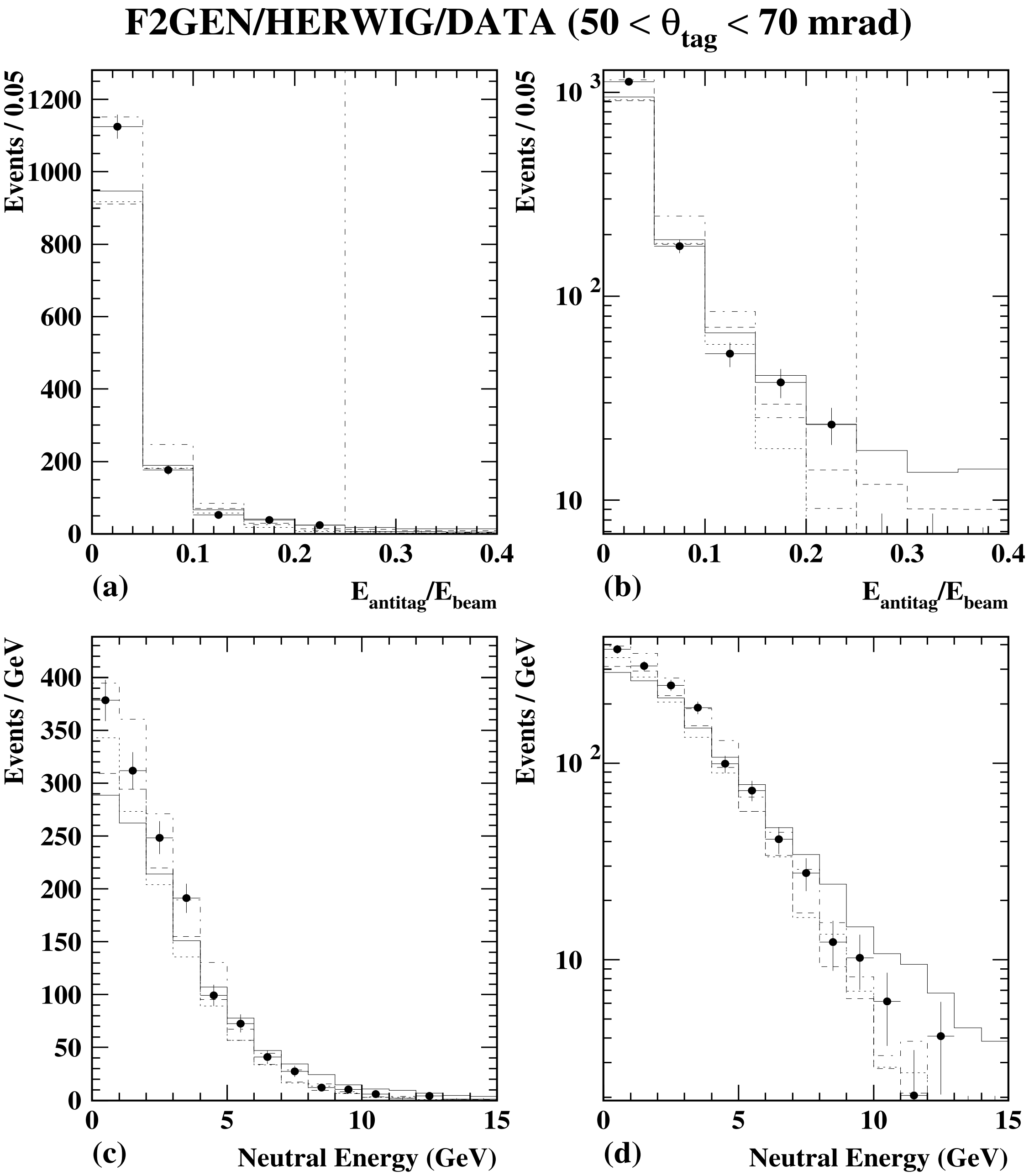

Figure 6.8: Anti–tag and neutral energy distributions for the data (dots) and the Monte Carlo models in the low θ_{tag} range. The different samples are from F2GEN GRV 100% point–like (solid), F2GEN GRV 'perimiss(0.1)' (dashed), HERWIG GRV without the SUE (dotted) and HERWIG LAC1 without the SUE (dot–dashed).

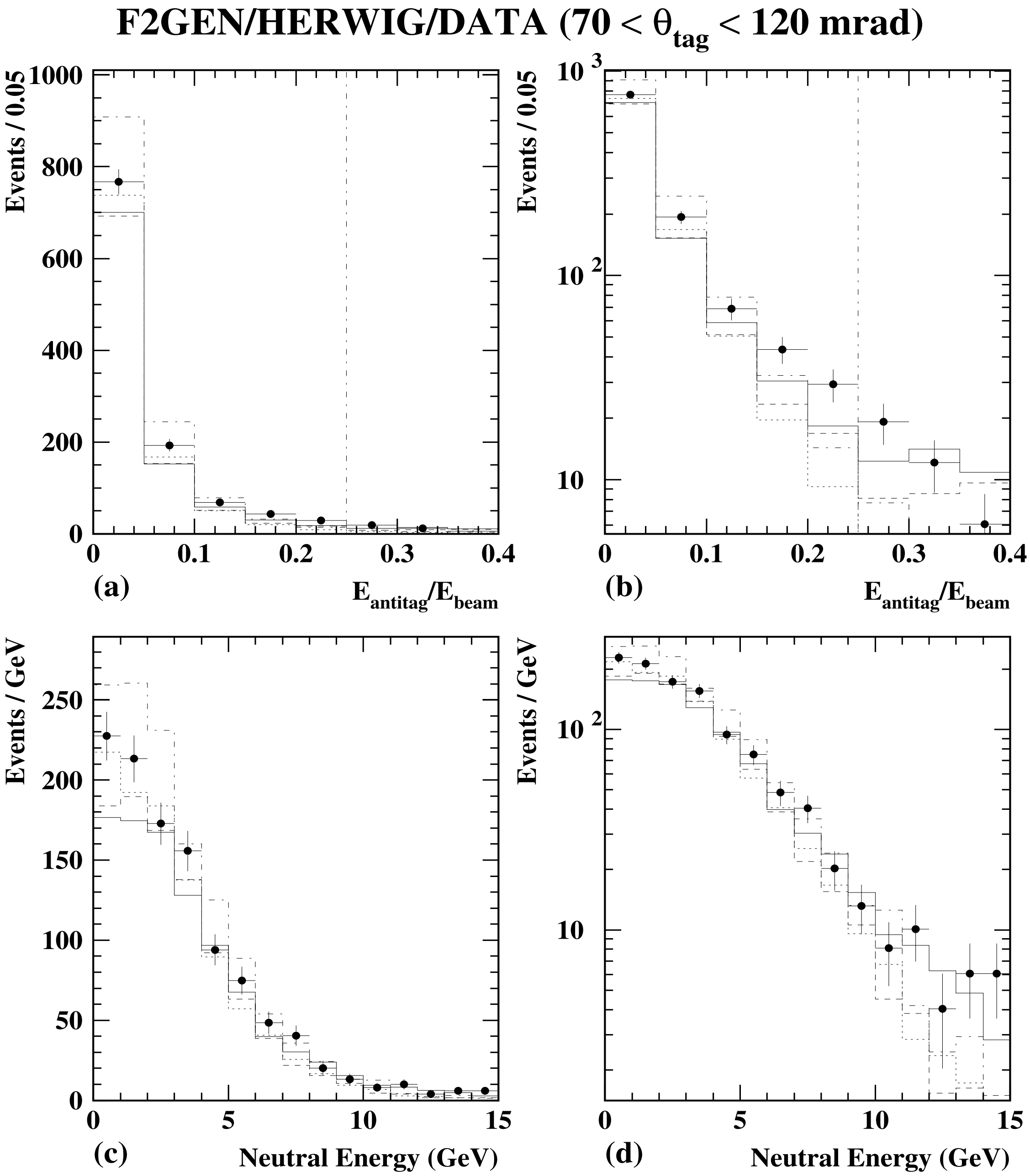

Figure 6.9: Anti-tag and neutral energy distributions for the data (dots) and the Monte Carlo models in the high θ_{tag} range. The different samples are from F2GEN GRV 100% point–like (solid), F2GEN GRV 'perimiss(0.1)' (dashed), HERWIG GRV without the SUE (dotted) and HERWIG LAC1 without the SUE (dot–dashed).

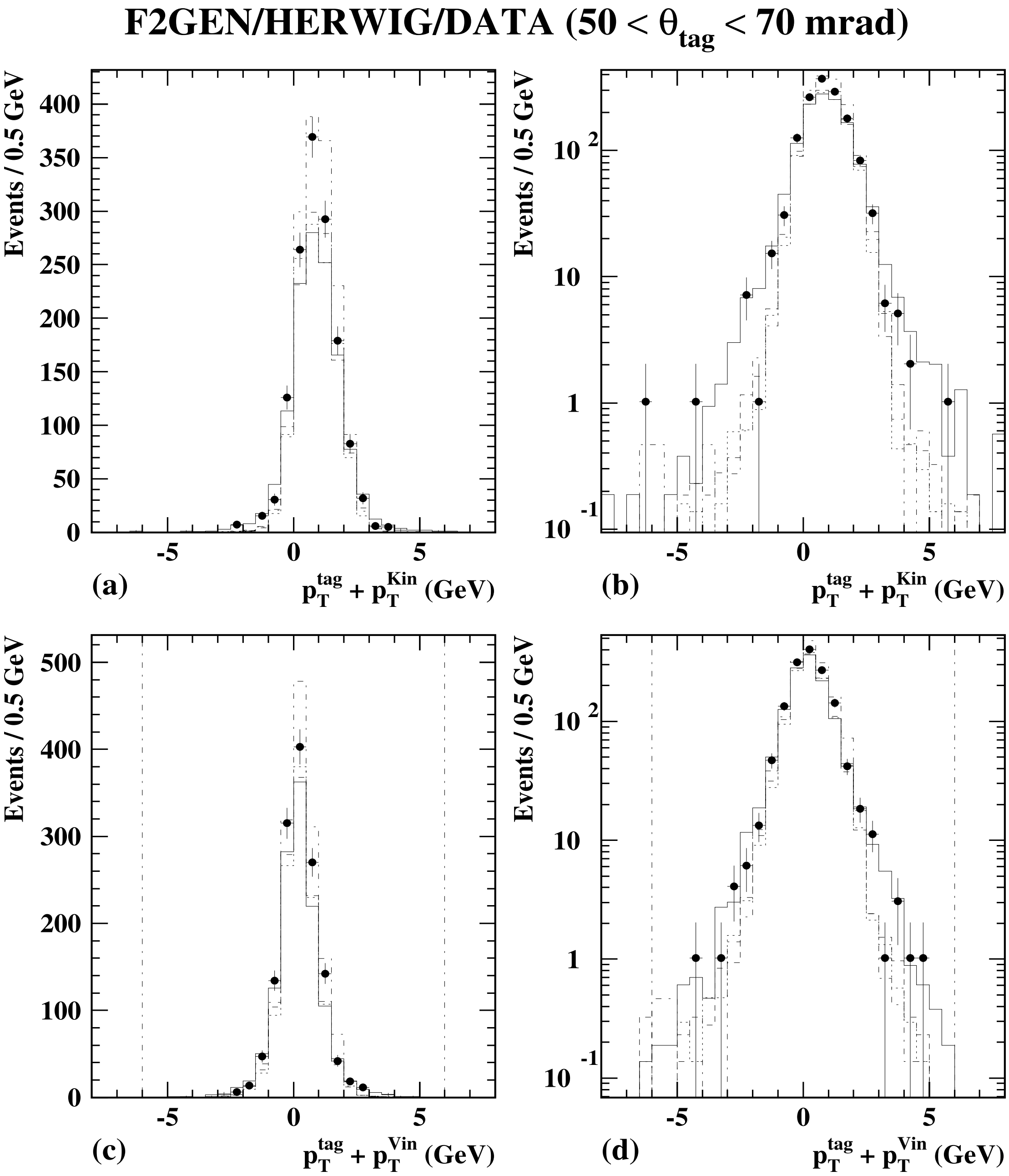

Figure 6.10: Transverse momentum distributions (defined in Section 4.1.3) in the plane of the beam and the tag for the data (dots) and the Monte Carlo models in the low θ_{tag} range. The different samples are from F2GEN GRV 100% point–like (solid), F2GEN GRV 'perimiss(0.1)' (dashed), HERWIG GRV without the SUE (dotted) and HERWIG LAC1 without the SUE (dot–dashed).

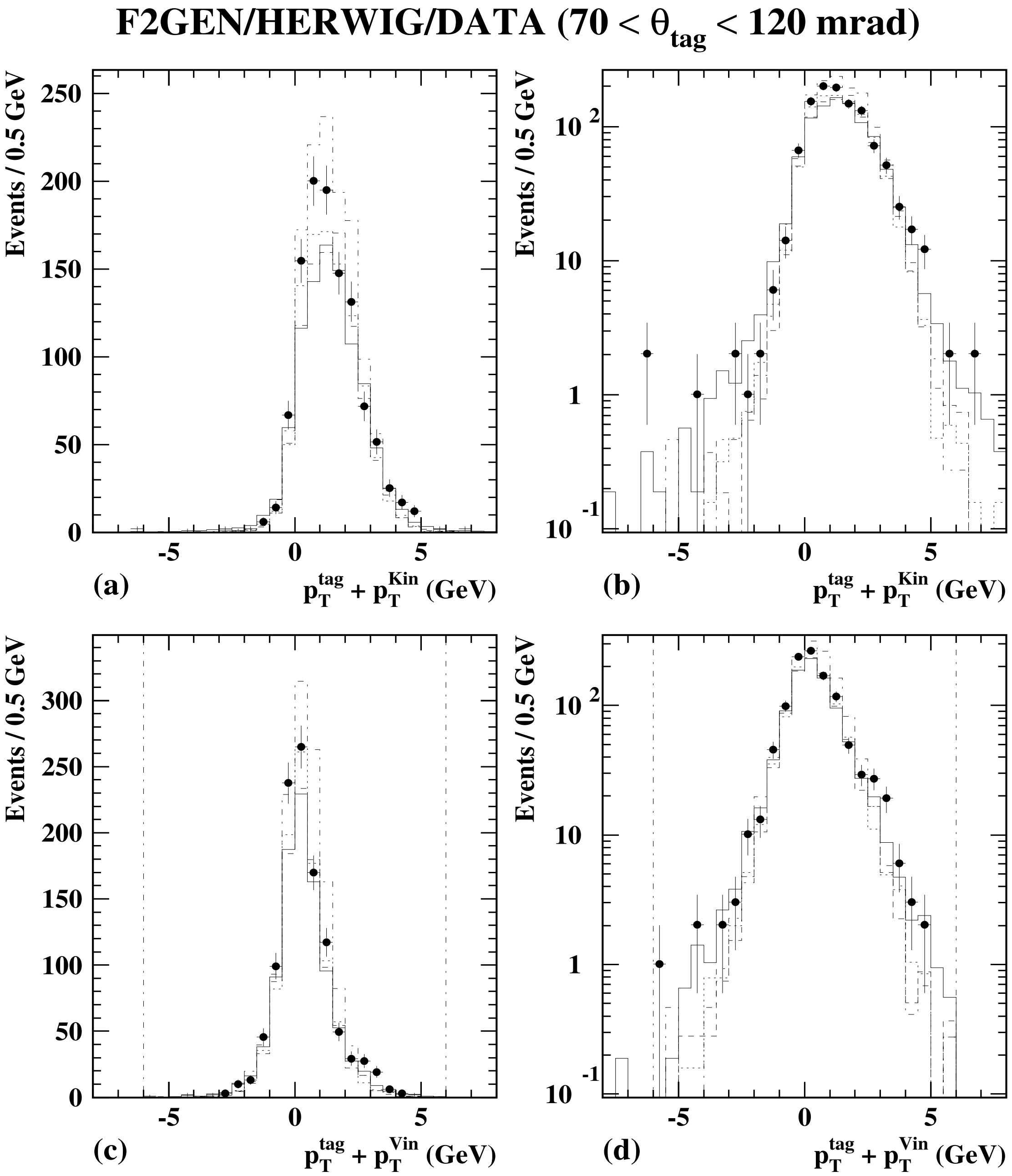

Figure 6.11: Transverse momentum distributions (defined in Section 4.1.3) in the plane of the beam and the tag for the data (dots) and the Monte Carlo models in the high θ_{tag} range. The different samples are from F2GEN GRV 100% point–like (solid), F2GEN GRV 'perimiss(0.1)' (dashed), HERWIG GRV without the SUE (dotted) and HERWIG LAC1 without the SUE (dot–dashed).

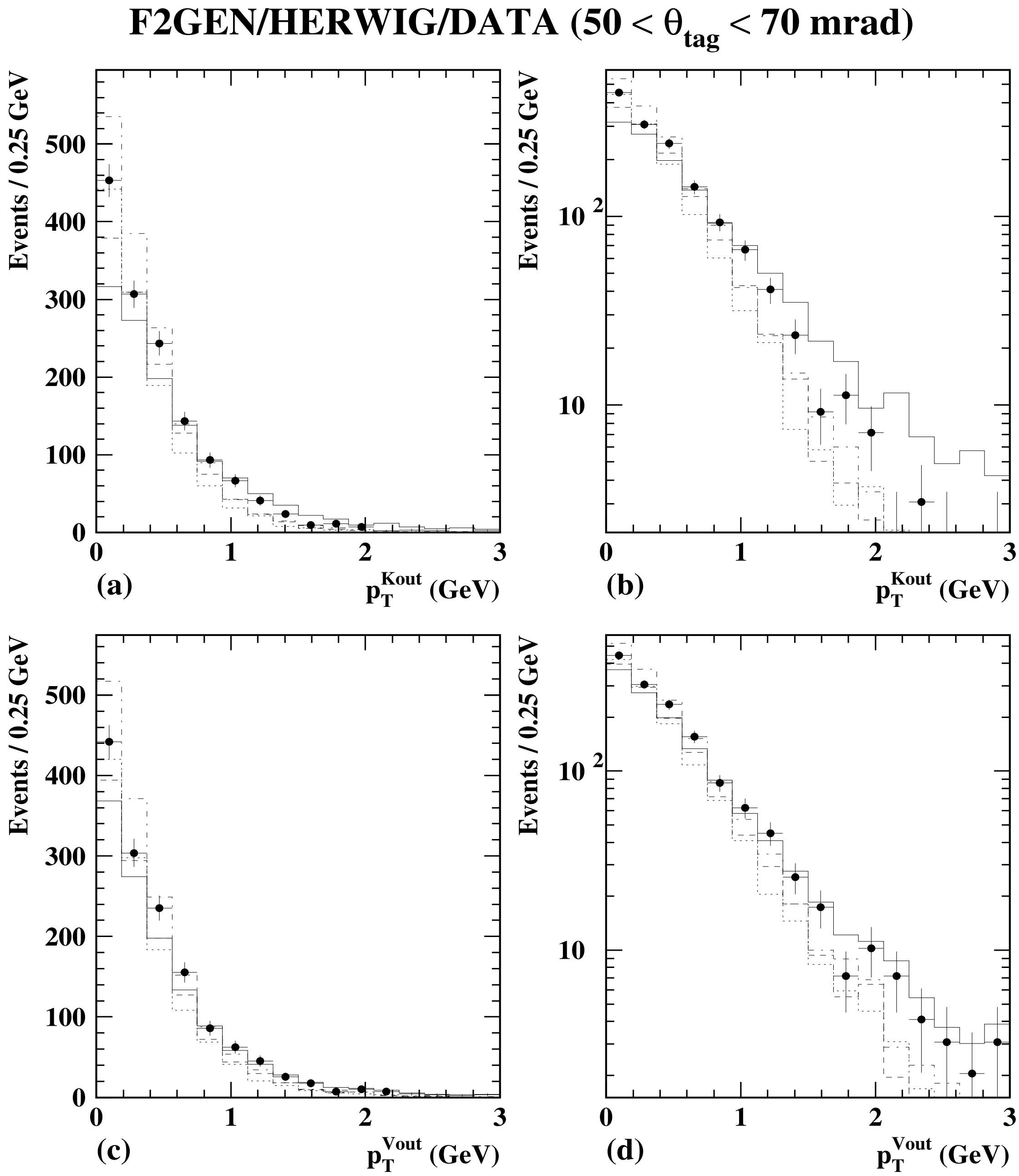

Figure 6.12: Transverse momentum distributions (defined in Section 4.1.3) out of the plane of the beam and the tag for the data (dots) and the Monte Carlo models in the low θ_{tag} range. The different samples are from F2GEN GRV 100% point–like (solid), F2GEN GRV 'perimiss(0.1)' (dashed), HERWIG GRV without the SUE (dotted) and HERWIG LAC1 without the SUE (dot–dashed).

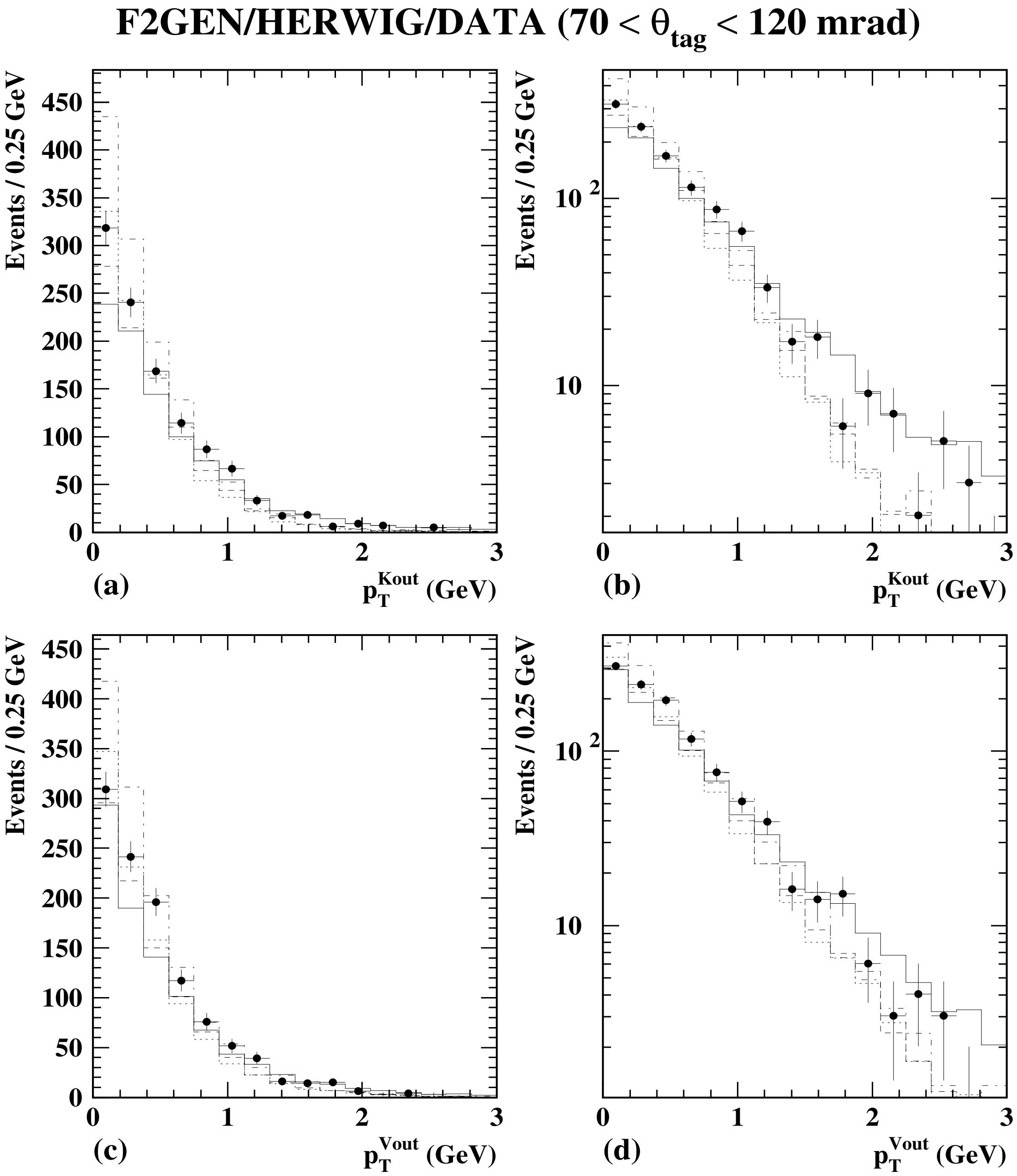

Figure 6.13: Transverse momentum distributions (defined in Section 4.1.3) out of the plane of the beam and the tag for the data (dots) and the Monte Carlo models in the high θ_{tag} range. The different samples are from F2GEN GRV 100% point–like (solid), F2GEN GRV 'perimiss(0.1)' (dashed), HERWIG GRV without the SUE (dotted) and HERWIG LAC1 without the SUE (dot–dashed).

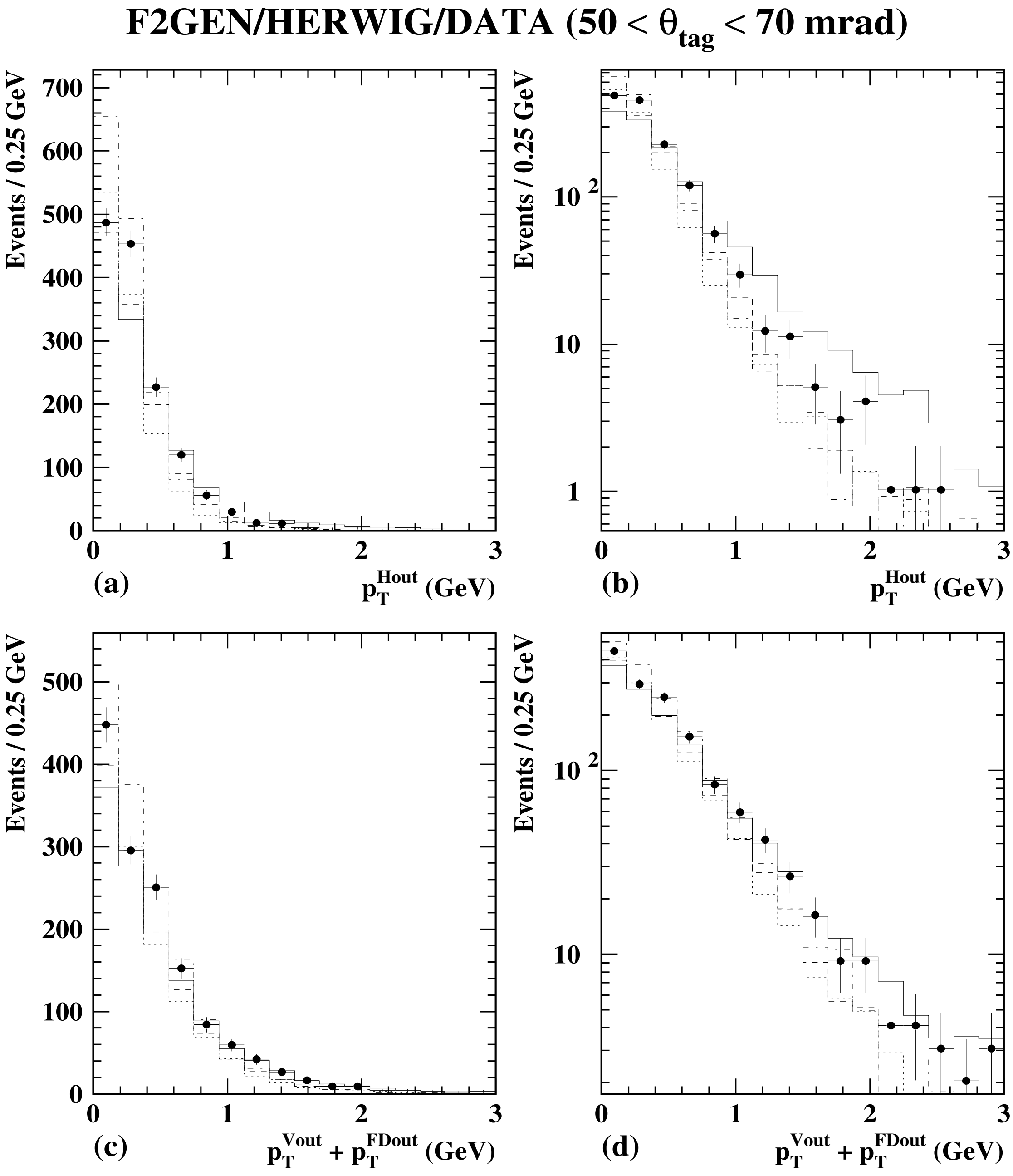

Figure 6.14: Transverse momentum distributions (defined in Section 4.1.3) out of the plane of the beam and the tag for the data (dots) and the Monte Carlo models in the low θ_{tag} range. The different samples are from F2GEN GRV 100% point–like (solid), F2GEN GRV 'perimiss(0.1)' (dashed), HERWIG GRV without the SUE (dotted) and HERWIG LAC1 without the SUE (dot–dashed).

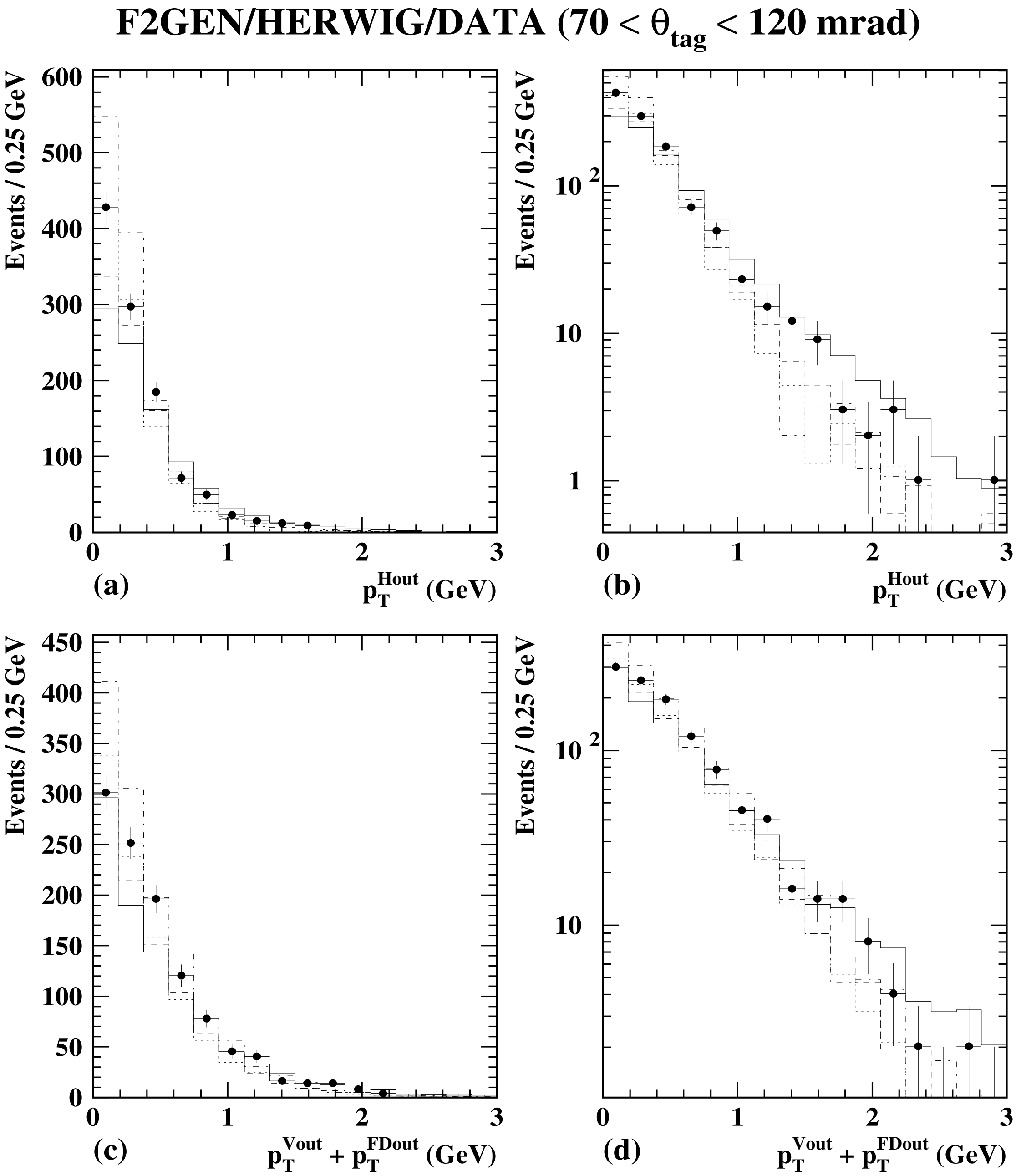

Figure 6.15: Transverse momentum distributions (defined in Section 4.1.3) out of the plane of the beam and the tag for the data (dots) and the Monte Carlo models in the high θ_{tag} range. The different samples are from F2GEN GRV 100% point–like (solid), F2GEN GRV 'perimiss(0.1)' (dashed), HERWIG GRV without the SUE (dotted) and HERWIG LAC1 without the SUE (dot–dashed).

cles in the p_T calculations reduces the separation between the different final state samples.

Track Multiplicity and Energy Distributions

Figures 6.16(a) and 6.17(a) plot the track multiplicity, n_{trk}, of good quality tracks. The analysis requires at least three good charged tracks and each figure shows a large difference between data and Monte Carlo models in the $n_{trk} = 2$ bin. The excess in the data is partly due to muon pairs being produced from two photons. Above the cut there is generally good agreement between data and all of the Monte Carlo models, showing that this distribution is not ideal for distinguishing $\gamma^*\gamma$ fragmentation models. The energy of individual tracks, E_{trk}, is plotted in Figures 6.16(b) and 6.17(b). There is not a very good agreement between the shapes of the E_{trk} distributions, and this becomes apparent in the energy flow distributions considered next.

Pseudorapidity and Energy Flow

The pseudorapidity of a particle is defined as

$$\eta = -\log\tan\left(\frac{\theta}{2}\right) \tag{6.1}$$

where θ is the polar angle of the particle in the detector measured from the direction of the beam that has produced the target photon. Therefore the tag is always at the negative side of the pseudorapidity plot. An energy flow distribution is obtained by weighting each entry of the pseudorapidity plot by the energy of the object at that pseudorapidity.

The pseudorapidity and energy flow distributions of tracks in the low θ_{tag} region are shown in Figures 6.16(c) and 6.16(d) respectively. They are important because they each show a difference between the 100% point–like model and the data. In particular, the double–peak feature in energy flow in the data does not exist in the 100% point-like model. The other three Monte Carlo models in the low θ_{tag} region, apart from normalisation, look more like the data in terms of shape.

The pseudorapidity and energy distributions of tracks in the high θ_{tag} region are

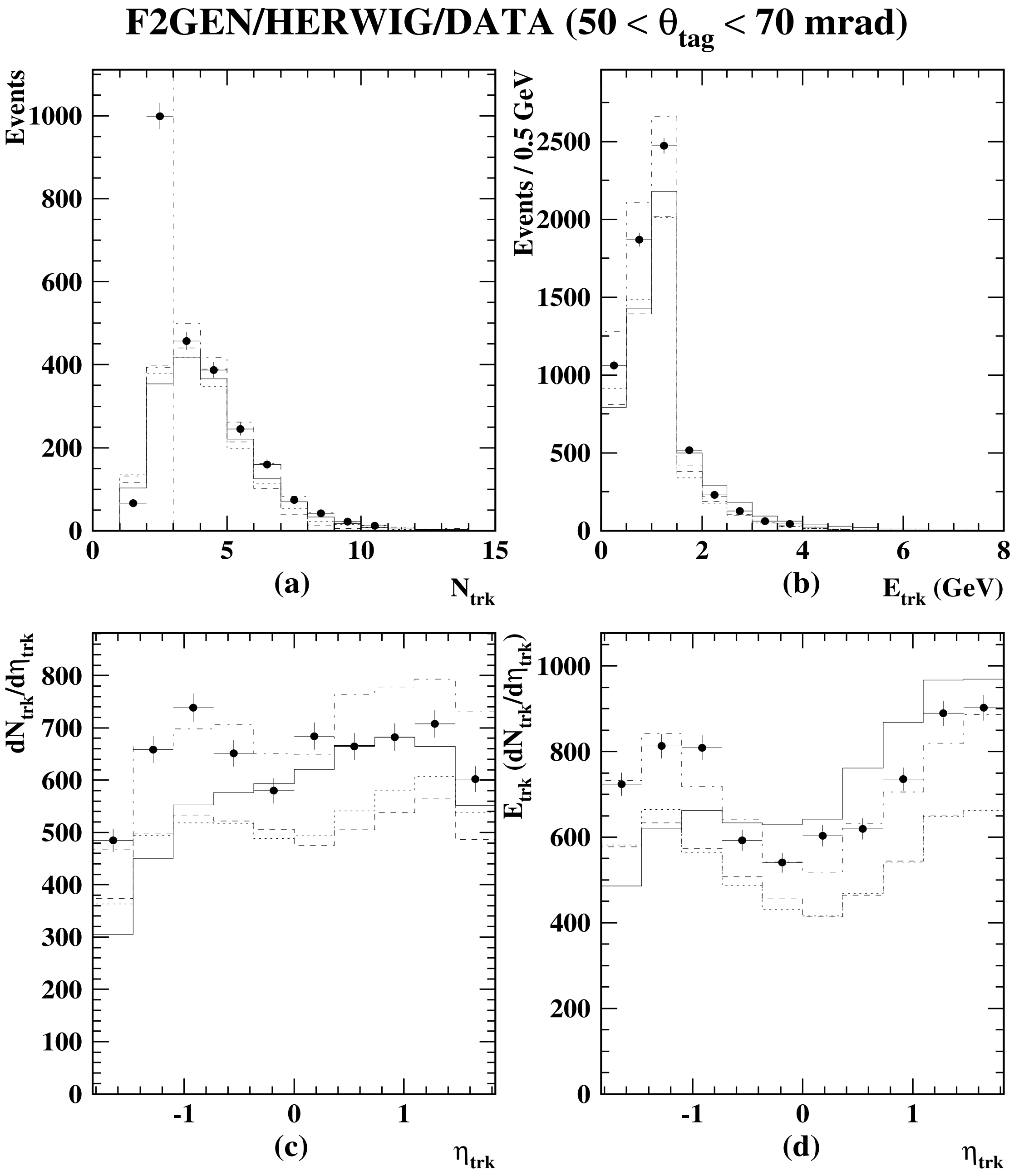

Figure 6.16: Track multiplicity, energy and energy flow distributions for the data (dots) and the Monte Carlo models in the low θ_{tag} range. The different samples are from F2GEN GRV 100% point–like (solid), F2GEN GRV 'perimiss(0.1)' (dashed), HERWIG GRV without the SUE (dotted) and HERWIG LAC1 without the SUE (dot–dashed).

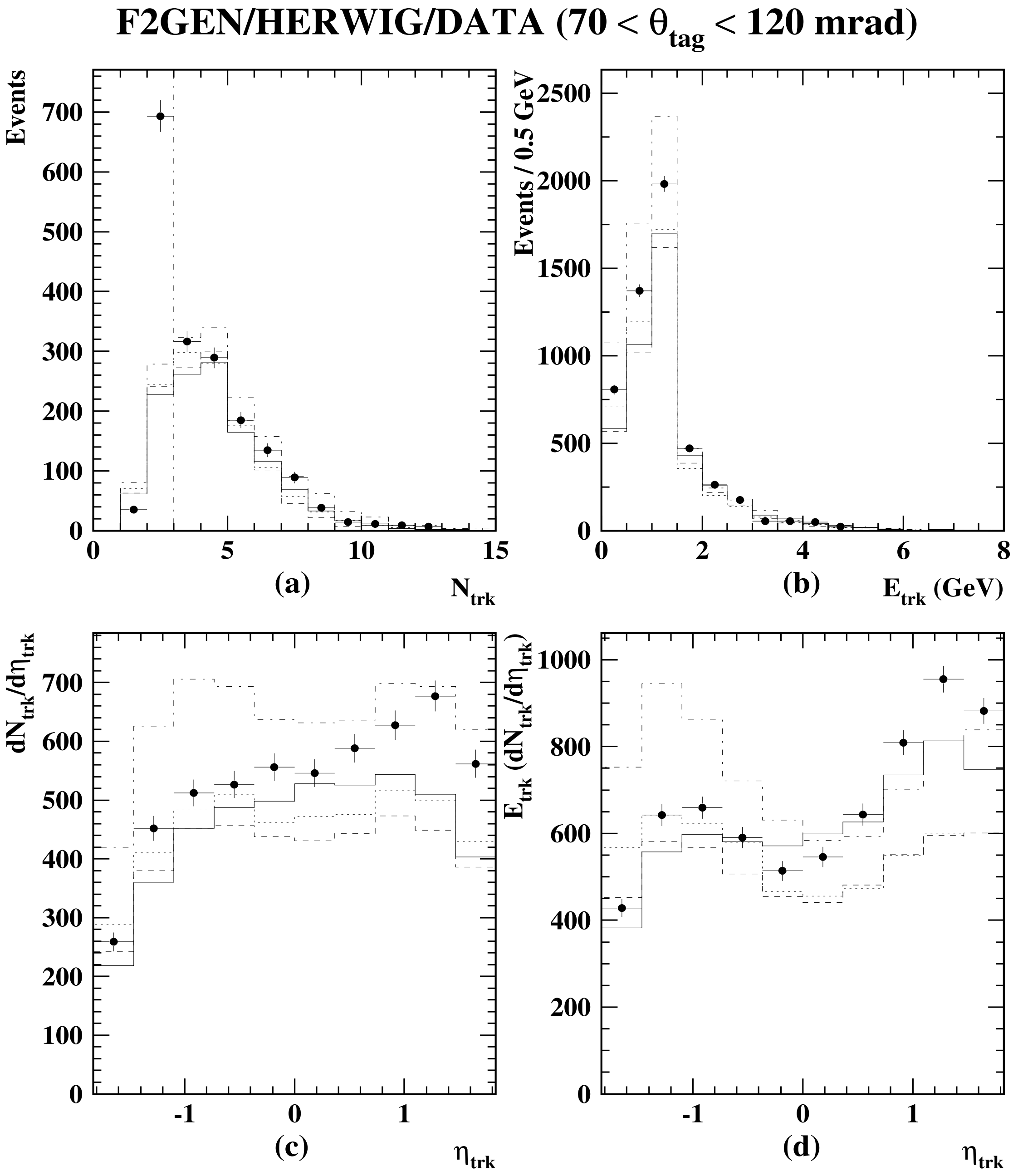

Figure 6.17: Track multiplicity, energy and energy flow distributions for the data (dots) and the Monte Carlo models in the high θ_{tag} range. The different samples are from F2GEN GRV 100% point–like (solid), F2GEN GRV 'perimiss(0.1)' (dashed), HERWIG GRV without the SUE (dotted) and HERWIG LAC1 without the SUE (dot–dashed).

shown in Figures 6.17(c) and 6.17(d) respectively. The data now have a track energy distribution that is double–peaked, asymmetric and more pronounced in the hemisphere opposite to the tag. None of the Monte Carlo models have this feature. There are two conclusions to be made from this observation. Firstly, the Monte Carlo models must have their $\gamma^*\gamma$ fragmentation model adjusted to provide a better description of the data. Secondly, if these models are used for unfolding, one has to make an estimate of the systematic error on the unfolded result due to uncertainties in the $\gamma^*\gamma$ fragmentation.

6.3 Summary

This chapter is summarised with the following points:

- The separation of different $\gamma^*\gamma$ fragmentation models is less prominent in the high θ_{tag} region than in the low θ_{tag} region. This is most clearly seen by comparing the x_{vis}/x_{true} correlation plots of Figures 6.6 and 6.7, but can also be seen from the tails of the transverse momentum, neutral energy and W_{vis} distributions.
- Both the photon structure function and the $\gamma^*\gamma$ fragmentation affect the shape of the visible x distribution.
- The track pseudorapidity and energy flow distributions, with the tag at one side of the plot, show that different $\gamma^*\gamma$ fragmentation models can be distinguished, even when only considering the central detector region.
- From the energy flow distributions of Figures 6.16(d) and 6.17(d), one can see that none of the Monte Carlo models correctly describe the $\gamma^*\gamma$ fragmentation. If the present $\gamma^*\gamma$ fragmentation models are to be used for the determination of $F_2^\gamma(x)$ (see the next Chapter), one must estimate a systematic error on the result due to uncertainties in the $\gamma^*\gamma$ fragmentation models.

Chapter 7

Unfolding

The measurement of $F_2^\gamma(x)$ with the OPAL detector is an example of the classic problem in experimental physics of how to find a true distribution given a detected signal and knowledge of the experimental apparatus.

In this chapter we shall first see why we cannot obtain $F_2^\gamma(x)$ directly from our data. Unfolding is the process by which we recover $F_2^\gamma(x)$ from our data distributions. The general problem of unfolding is discussed, followed by a summary of the unfolding procedure used for this work. Finally, and most importantly, we test our unfolding procedure on Monte Carlo samples generated from various $F_2^\gamma(x)$ parameterisations that have different features, to see if those features are resolved.

7.1 The Problem of Measuring $F_2^\gamma(x)$

The aim of our work is to measure $F_2^\gamma(x)$ by taking measurements from events where the particle reaction $\gamma^*\gamma \to$ hadrons occurs. With an ideal detector we could just obtain $F_2^\gamma(x)$ from a simple histogram of x but with our detector this determination is complicated by a number of effects:

1) Limited acceptance

   The probability to observe a given event is less than one.

2) Backgrounds

We do observe some events that look like $\gamma^*\gamma \to$ hadrons events, but are not.

3) Transformation

Instead of measuring the quantity x from the event of interest, we measure the related quantity x'. In this thesis such a quantity is x_{Bj} (see Equation 1.7). Here, x'_{Bj} differs from x_{Bj} because the measured invariant mass, W_{vis}, of particles from the $\gamma^*\gamma$ collision is less than the true invariant mass, W_{true}. This is due to some of the particles from the $\gamma^*\gamma$ collision being lost in the forward direction or being discarded for not having good track or neutral cluster quality. A Monte Carlo example of the difference between x'_{Bj} and x_{Bj} (called x_{vis} and x_{true} respectively elsewhere in this thesis) is shown in Figure 7.1.

4) Resolution

The measured quantities are smeared out due to the finite resolution of the detector.

The general problem can be summarised as follows: Suppose we have a true distribution $f(x)$. The expected distribution from the experiment, $g(x')$, can be written as the convolution

$$g(x') = \int A(x', x) f(x) dx + b(x') \tag{7.1}$$

where $A(x', x)$ is a known function that describes the response of the detector and $b(x')$ represents the known background. The data, $d(x')$, will differ from $g(x')$ by statistical errors $e(x')$. The determination of $f(x)$ from $d(x')$ is the well-known problem of unfolding.

7.2 The Forward Method

One can assume a true distribution $f(x)$. The resulting distribution $g(x')$ can be calculated using Equation 7.1. The parameters in $f(x)$ can be adjusted in such a way that the set of parameters that gives a minimum χ^2 between $g(x')$ and $d(x')$ is taken to be the solution. This has the advantage that the model may be simple,

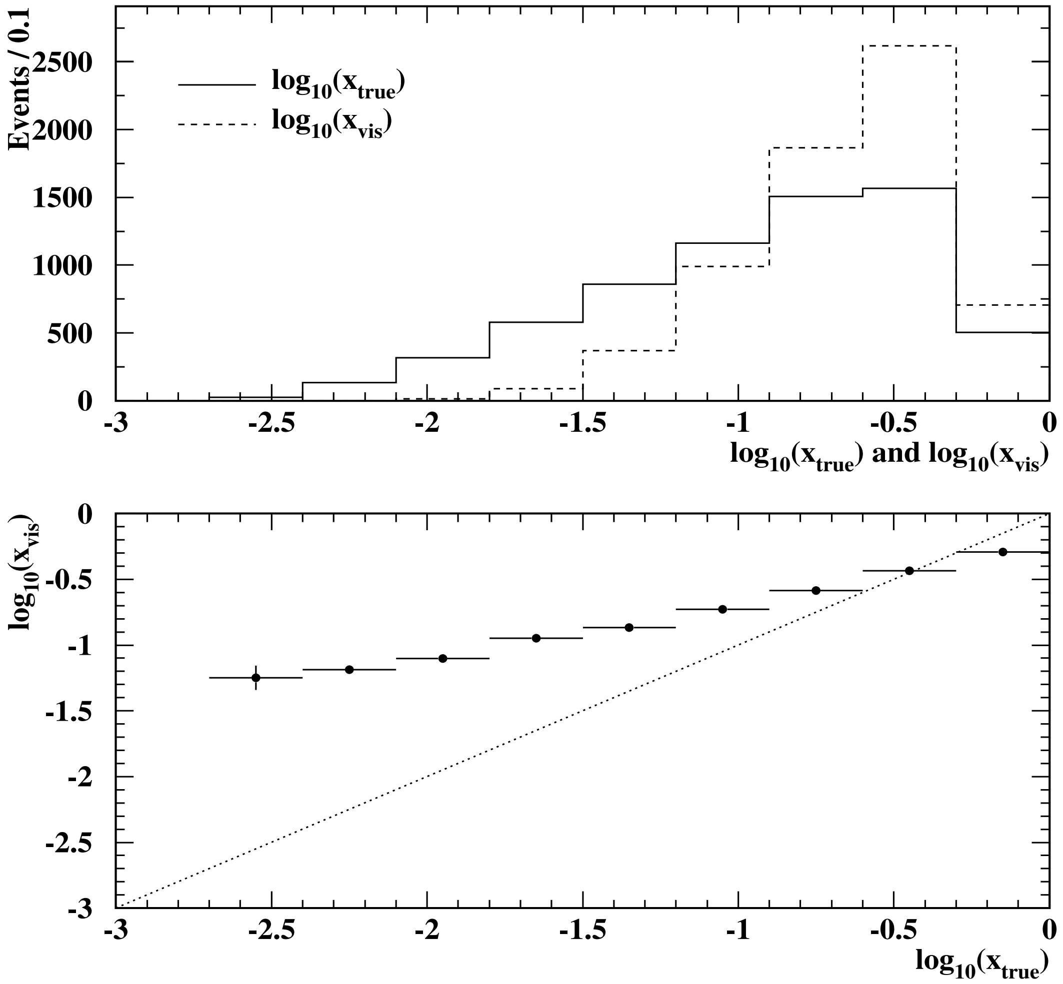

Figure 7.1: Histogram and profile plot of x_{vis} and x_{true}. The HERWIG Monte Carlo has been used with the GRV F_2^γ and without the soft underlying event. The events have passed the analysis cuts with tags for all of the θ_{tag} region (50–120 mrad). The vertical error bars on the profile plot represent the error on the mean.

with only a few parameters to vary, and that these parameters and their errors may be estimated. One should, however, be aware that a perfectly acceptable set of parameters may result in a poor model fitting the data well.

7.3 The Inverse Method

The classical solution to Equation 7.1 would be to assume no prior information and deconvolve it directly. Such methods are problematic for the following three reasons.

1) Some possible true distributions exist where the convolution of the true distribution $f(x)$ with the detector response function is zero. Thus the data, $d(x')$, contain no information about these signals and solving Equation 7.1 for $f(x)$ does not have a unique solution. This lack of unique solutions occurs because the smearing effect of A removes information about finely structured signals.

2) The presence of the statistical error $e(x')$ in the data increases the number of possible solutions because some true distributions $f(x)$ exist such that the convolution of $f(x)$ with the detector response function is small compared to the expected statistical error. Such a solution can be added to any other possible solution to give yet another solution. This is why instabilities occur when trying to directly invert Equation 7.1; small changes in the data correspond to large changes in the estimate of $f(x)$.

3) The data are discrete and finite in number and the true distribution, $f(x)$, is continuous.

Without prior information, there is no way to favour one solution over another. The method of unfolding used for this work is one of *regularisation* which will be described in Section 7.5. The method has been implemented by Blobel in a package called *RUN* [109]. Our data is binned, so before unfolding, we must consider the discretized version of Equation 7.1.

7.4 Discretization

Discretization is done in two steps. In the first step, $f(x)$ is parameterised by the sum

$$f(x) = \sum_{j=1}^{m} a_j p_j(x). \tag{7.2}$$

where the basis functions $p_j(x)$ are taken to be cubic B–splines. Using cubic B–splines enables $f(x)$ to be a smooth curve parameterised by m coefficients. Then Equation 7.2 can be written as

$$g(x') = \sum_{j=1}^{m} a_j A_j(x') + b(x') \tag{7.3}$$

with

$$A_j(x') = \int A(x', x) p_j(x) dx. \tag{7.4}$$

The expected distribution $g(x')$ has therefore been expressed as a superposition of functions $A_j(x')$, which each represent one of the basis functions $p_j(x)$ in Equation 7.2.

In the second discretization step, all of the x'–dependent functions of Equation 7.3 are represented by histograms;

$$g_i = \int g(x')\ dx' \qquad A_{ij} = \int A_j(x')\ dx' \qquad b_i = \int b(x')\ dx' \tag{7.5}$$

where the integral is over the ith bin. The discretized version of Equation 7.1 is therefore

$$g = Aa + b \tag{7.6}$$

where g and b are n–vectors, a is an m–vector containing the a_j coefficients and A is an $n \times m$ matrix of elements A_{ij}. The elements of the A matrix are defined by Monte Carlo events. The data d is also an n–vector.

7.5 Unfolding

The unfolding can now proceed by fitting the linear expression of Equation 7.6 to the data d. For the matrix inversion method (in the case $m = n$)

$$a = A^{-1}(d - b) \tag{7.7}$$

and the resulting distribution $f(x)$ from Equation 7.2 can show oscillating behaviour, with fluctuations larger than anything that is physically motivated.

Determination of a.

By the maximum likelihood method, the best estimate of a is given by $\hat{a}$, for which the likelihood function takes on its largest value. It is usual in the maximum likelihood method to search for the minimum of the negative logarithm of the likelihood function

$$S(a) = -\sum_{i=1}^{n} \log P(d_i|g_i) \tag{7.8}$$

where $P(d_i|g_i)$ is the probability of observing d_i events if g_i events are expected. The number of entries in a histogram bin will follow the Poisson distribution

$$P(d_i|g_i) = e^{-g_i}\frac{(g_i)^{d_i}}{(d_i)!}. \tag{7.9}$$

Inserting this expression into Equation 7.8, and disregarding constant terms, one obtains

$$S(a) = \sum_{i=1}^{n} (g_i - d_i \log g_i). \tag{7.10}$$

$S(a)$ can be approximated by a quadratic function. The motivation for this approximation is that the minimum can be determined by standard matrix methods. The quadratic approximation is, in matrix notation,

$$S(a) = S(\tilde{a}) - (a - \tilde{a})^T h + \frac{1}{2}(a - \tilde{a})^T H (a - \tilde{a}) \tag{7.11}$$

where the derivatives of $S(a)$ with respect to the parameters at an approximate solution $\tilde{a}$ are given by

$$h_j = -\frac{\partial S}{\partial a_j} = -\sum_{i=1}^{n}\left(A_{ij} - \frac{d_i}{g_i}A_{ij}\right) \tag{7.12}$$

and

$$H_{jk} = -\frac{\partial^2 S}{\partial a_j \partial a_k} = -\sum_{i=1}^{n} d_i \frac{A_{ij}A_{ik}}{g_i^2}. \tag{7.13}$$

The minimum condition is $\nabla S = 0$. The resulting approximation to the true a is

$$a_{app} = \tilde{a} + H^{-1}h \tag{7.14}$$

and is based on the approximation of the true function $S(\tilde{a})$ at $\tilde{a}$. The process is iterated, taking the result of the previous iteration for $\tilde{a}$, until both the expected change of $S(a)$ in one iteration

$$(\Delta S)_{exp} = -\frac{1}{2}(a_{app} - \tilde{a})^T h \tag{7.15}$$

and the actual change of $S(a)$ are small compared to 1. Convergence is usually achieved, resulting in $\hat{a}$, within a few iterations.

Unfolding without Regularisation

The method described in the previous section does not remove the inherent instabilities. Consider one step of the iteration process described above. The matrix H is symmetric, so it can be transformed to a diagonal matrix D by

$$D = U_1^T H U_1, \tag{7.16}$$

where D contains in its diagonal the real and positive eigenvalues D_{jj} of H. The matrix U_1 is orthogonal with the property $U_1^T U_1 = I_{mm}$ and it contains the eigenvectors u corresponding to the eigenvalues in its columns. The eigenvalues can be arranged in decreasing order $D_{11} \geq D_{22} \geq \ldots D_{mm}$. A diagonal matrix $D^{1/2}$ with the property $D^{1/2}D^{1/2} = D$ can be defined, which has the positive square roots of D_{jj} in the diagonal. The parameter vector a can be related to another vector a_1 by

$$a = U_1 D^{-1/2} a_1. \tag{7.17}$$

Inserting this into Equation 7.11 and applying the minimum condition $\nabla S = 0$, the solution

$$\hat{a}_1 = D^{-1/2} U_1^T (H\tilde{a} + h) \tag{7.18}$$

is obtained.

The importance of this transformation is that the vector $\hat{a}_1$ has the property that the covariance matrix $V(\hat{a}_1)$ is equal to the unit matrix I, so that each of the components of $\hat{a}_1$ are statistically independent and have a variance of 1. Since these components are independent, the significance of every component can be tested. If all $(\hat{a}_1)_j$ with $j > m_0$ are compatible with zero, then they can be ignored. The result can be expressed as a linear combination of the first m_0

eigenvectors. Equation 7.17 can be re–written as

$$\hat{a} = \sum_{j=1}^{m} \left(\frac{1}{D_{jj}} \right)^{1/2} (\hat{a}_1)_j \, u_j. \tag{7.19}$$

It is clear that insignificant components get a large weight factor in the full solution, because of the $(1/D_{jj})^{-1/2}$ factor in Equation 7.19. Setting all $(\hat{a}_1)_j = 0$ where $j > m_0$ also introduces some fluctuations in the solution (known as the "Gibbs phenomenon" in Fourier analysis theory). A smooth cut off reducing these oscillations is provided by the method of *regularisation*.

Unfolding with Regularisation

The regularisation technique introduces a smooth cut–off in the $(\hat{a}_1)_j$ coefficients, whilst also introducing a bias much less than the statistical error. The regularised result is

$$\bar{f}(x) = \sum_{j=1}^{m} \bar{a}_j p_j(x). \tag{7.20}$$

where the bar indicates that the regularisation weight has been included.

Final Unfolded Result

The final unfolded results are represented by histograms with error bars. The data values f_k are obtained by integration of $\bar{f}(x)$ over regions in x;

$$f_k = \left(\int_{x_{k-1}}^{x_k} \bar{f}(x) \, dx \right) / (x_k - x_{k-1}). \tag{7.21}$$

The bin limits are chosen in such a way that the bin-to-bin correlations are minimised.

7.6 Unfolding Examples

The Monte Carlo events that have been generated (see Table 5.2) can be used to verify that the unfolding algorithm correctly determines the known $F_2^\gamma(x)$ of a Monte Carlo sample that is treated as mock data. In the examples presented in this chapter, the following information has been given to the unfolding program:

- $\log_{10}(x_{vis})$ of each "data" event that passes the selection cuts;
- $\log_{10}(x_{vis})$ and $\log_{10}(x_{true})$ of each Monte Carlo event that passes the same selection cuts;
- the integrated luminosity of the "data" sample and the Monte Carlo sample;
- $F_2^\gamma(x)$ of the parameterisation used in the generation of the unfolding Monte Carlo sample. Implicit in this information are the number of flavours used in the generation of the Monte Carlo and some information about the Q^2 scale involved.

7.6.1 Unfolding in a Q^2 Bin

Ideally, $F_2^\gamma(x)$ should be determined at one Q^2 scale. However, the data and the unfolding Monte Carlo have events with various Q^2 values where the Q^2 of each event is determined from the tag energy and the tag angle. By requiring a tag angle range and a minimum tag energy, a finite Q^2 range is defined.

As outlined above, the unfolding program needs to know the $F_2^\gamma(x)$ used in the event generation so that it may be re–weighted to give the unfolded result. This re–weighting occurs only in the x variable, so the Q^2 scale has to be set in the unfolding. The Q^2 value chosen is usually that of the mean Q^2 of data events that have passed the selection cuts.

One should be aware that events contributing to the lowest x–point in an unfolding will have a mean Q^2 less than the mean Q^2 of the whole sample. Since the latter value is used to represent the scale that the Monte Carlo events were generated at, the $F_2^\gamma(x)$ to be re–weighted will be too big (due to the increase of $F_2^\gamma(x)$ with Q^2) and consequently the unfolded $F_2^\gamma(x)$ value for the low-x bin will be too big. The converse is true for the highest x point in the unfolding. One could correct for this, but for a comparison of an unfolded result with a theoretical expectation, it is unnecessary if the theoretical expectation for the x–bin is derived from the theory curve as a function of x with Q^2 set to the mean Q^2 of the "data" events. Essentially, so long as one is consistent in both the unfolding and in the comparison to theory, then the comparison is a fair one.

The comparison of an unfolded result with a theoretical expectation has been reduced to being with a variation of x alone. Since the bins of the unfolded result have width in x, one has to decide where within a wide bin in x one can correctly compare the unfolded value to the theoretical expectation. Neither the central value of each unfolded bin nor the weighted mean value (the barycentre) of the abscissa within the bin is the appropriate place to make the comparison, as has been demonstrated in [110]. Instead, the correct value of the predicted function is equal to its mean value over the whole wide bin. This is especially important at low–x where some theories have $F_2^\gamma(x)$ that vary rapidly and non–linearly across that bin.

A χ^2 goodness of fit of a theoretical model to an unfolded result can be determined using the expression

$$\chi^2 = \Delta_i (V^{-1})_{ij} \Delta_j,$$

where $\Delta_i = F_i^{meas} - \overline{F_i^{th}}$ in each bin i, and V is the statistical covariance matrix that is also an output of the unfolding.

All unfoldings presented in this thesis use a horizontal solid line for each x–bin to indicate the unfolded F_2^γ value for that bin. It's width represents the bin range rather than a horizontal error bar. The vertical lines represent the errors on the unfolded F_2^γ for that bin. They are positioned in the middle of the bin on the chosen scale of x. No importance is attached to the x–values at which these vertical error bars appear at. Any other labelled horizontal line refers to a theory expectation for the $(x,\, Q^2)$ bin of the data determined by the method described above.

7.6.2 The Unfolding Tests

Table 7.1 shows the HERWIG Monte Carlo samples used in the unfolding tests.

The x_{vis} column refers to whether or not the FD neutral clusters have been included in the evaluation of x_{vis}. When they have been included, only the raw cluster energies have been used as opposed to the corrected [80] ones. Also, only clusters with an energy of at least 2 GeV are used, so as to be consistent with the readout threshold of FD in the years 1990–1992. The F_2^γ column indicates which photon structure function has been used to generate the unfolding Monte Carlo (top line of each entry) and the mock data set (bottom line of each entry). The

Figure	θ_{tag} (mrad)	x_{vis}	F_2^γ	N_{cuts}	$\gamma^*\gamma$ fragmentation	ρ	$\chi^2/4$ DoF
7.2(a)	50–70	no FD	GRV	7160	no sue	0.70	-
			GRV	1000	no sue	-	1.2
7.2(b)	70-120	no FD	GRV	5882	no sue	0.72	-
			GRV	1000	no sue	-	0.9
7.2(c)	50–70	no FD	GRV	7160	no sue	0.70	-
			GRV	2615	with sue	-	78.7
7.2(d)	70-120	no FD	GRV	5882	no sue	0.72	-
			GRV	3473	with sue	-	15.0
7.3(a)	50–70	no FD	GRV	7160	no sue	0.70	-
			LAC1	3000	no sue	-	73.4
7.3(b)	70-120	no FD	GRV	5882	no sue	0.72	-
			LAC1	2632	no sue	-	3.96
7.3(c)	50–70	with FD	GRV	7287	no sue	0.81	-
			LAC1	3000	no sue	-	130.0
7.3(d)	70-120	with FD	GRV	5940	no sue	0.82	-
			LAC1	2655	no sue	-	30.9

Table 7.1: Monte Carlo samples generated by HERWIG for unfolding tests. In each entry, the first line is the unfolding Monte Carlo and the second line is the mock data. Further explanation of this table is given in Section 7.6.2.

N_{cuts} column shows how many events have passed the selection cuts. The 'final state' column refers to whether or not the soft underlying event has been included. ρ is the x_{vis}/x_{true} correlation and so an entry only exists for the unfolding Monte Carlo. Each unfolding has four bins in the final unfolded result. The χ^2 between the unfolded result and the $F_2^\gamma(x)$ that generated the mock data sample is given in the final column.

The purpose of the unfolding tests is to determine if the process of unfolding correctly recovers the photon structure function used to produce a mock data sample. Tests have been performed where the unfolding Monte Carlo and the mock data have

- the same $F_2^\gamma(x)$ and the same $\gamma^*\gamma$ fragmentation;
- the same $F_2^\gamma(x)$ and a different $\gamma^*\gamma$ fragmentation;
- a different $F_2^\gamma(x)$ and the same $\gamma^*\gamma$ fragmentation.

Same $F_2^\gamma(x)$ and Same $\gamma^*\gamma$ Fragmentation

These are ideal circumstances for the unfolding procedure. The x_{vis}/x_{true} relationship is identical for the unfolding Monte Carlo and the mock data, since the $\gamma^*\gamma$ fragmentation is the same in both. The results for the low and high θ_{tag} regions are shown in Figure 7.2 (a) and (b).

The χ^2 comparison shows an exceptionally good agreement between the unfolded result and the theoretical expectation. One might think that this result is trivial; on the contrary, it demonstrates that unfolding with $\log_{10}(x)$ as the unfolding variable does work, placing the lowest x points where they should be.

Same $F_2^\gamma(x)$ and Different $\gamma^*\gamma$ Fragmentation

When HERWIG events were generated with the same $F_2^\gamma(x)$ (GRV) but with different methods of treating the $\gamma^*\gamma$ fragmentation (with and without the soft underlying event), σ_{cuts} was different (see Table 5.2). One would expect, therefore, that if one $\gamma^*\gamma$ fragmentation model is used in the unfolding Monte Carlo and a different one for the mock dataset, the unfolded result must disagree with the

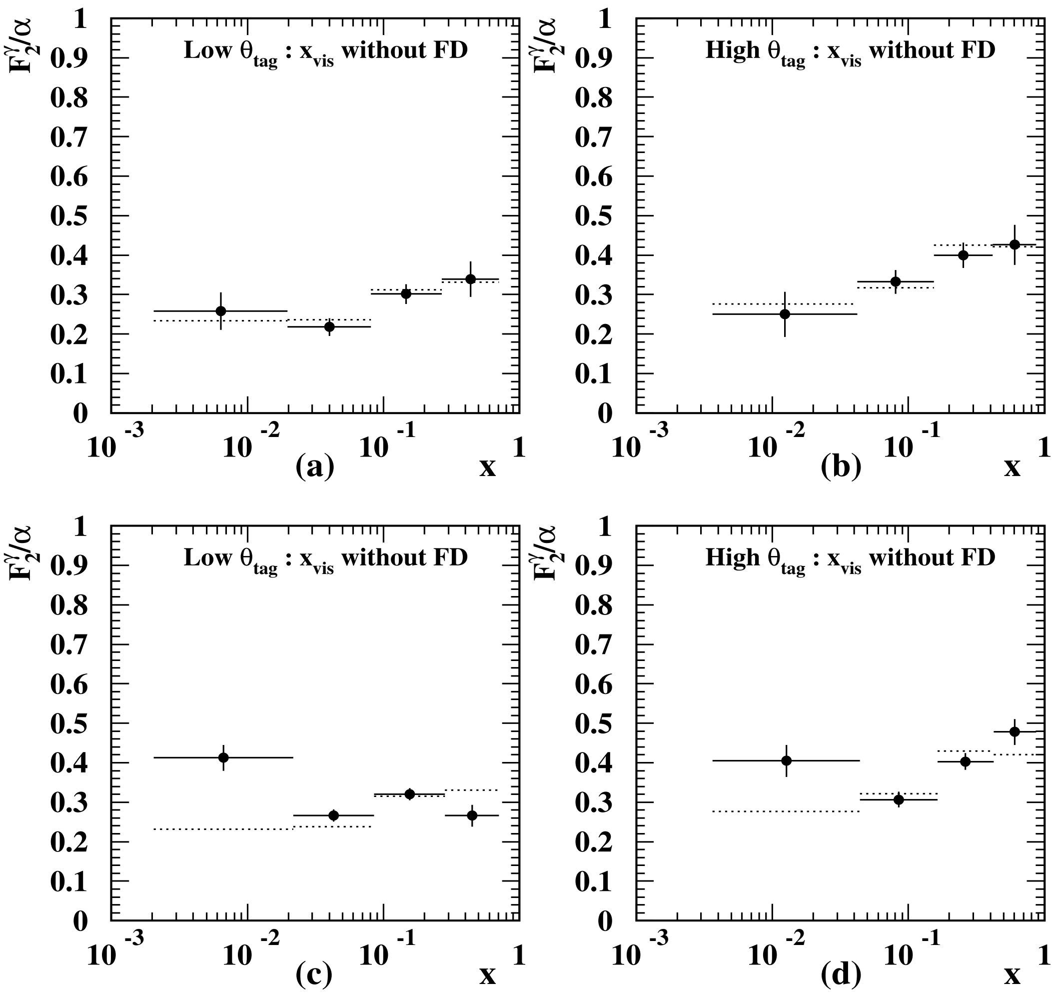

Figure 7.2: Test unfoldings each using the HERWIG generator with the GRV $F_2^\gamma(x)$ (*without* the soft underlying event) as the unfolding Monte Carlo. (a) and (b) use the HERWIG GRV $F_2^\gamma(x)$ *without* the soft underlying event as the "data". (c) and (d) use the HERWIG GRV $F_2^\gamma(x)$ *with* the soft underlying event as the "data". Solid lines represent the unfolded results and the horizontal dotted lines represent the GRV expectation values for each unfolded bin.

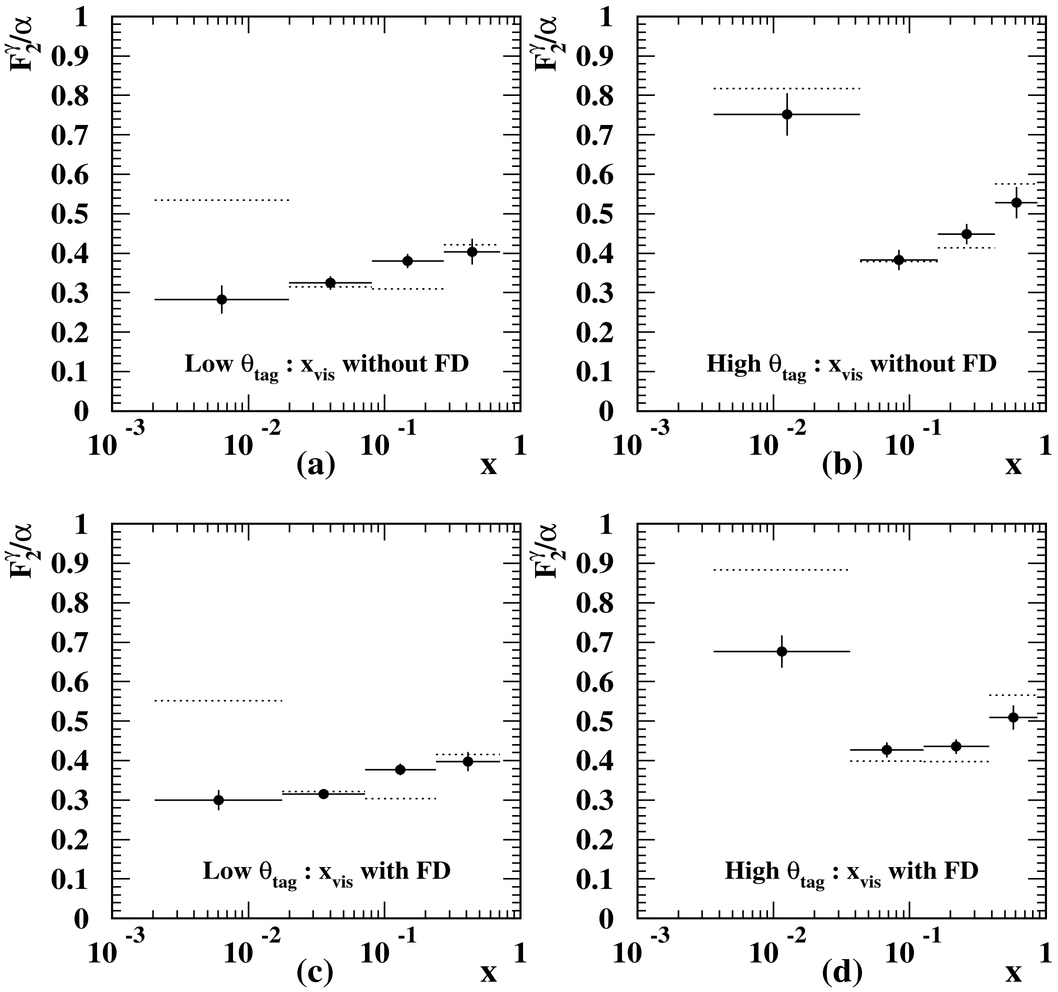

Figure 7.3: Test unfoldings each using the HERWIG generator with the GRV $F_2^\gamma(x)$ as the unfolding Monte Carlo. The "data" in each case come from HERWIG with the LAC1 $F_2^\gamma(x)$. Both the unfolding Monte Carlo and the "data" are without the soft underlying event. x_{vis} for both "data" and Monte Carlo is calculated *without* FD clusters in (a) and (b); *with* FD clusters in (c) and (d). Solid lines represent the unfolded results and the horizontal dotted lines represent the LAC1 expectation values for each unfolded bin.

theoretical expectation. Figure 7.2 (c) and (d) demonstrates that this is indeed the situation. The χ^2 values are poor, particularly for the low θ_{tag} (and hence low Q^2) bin. One should note how the additional events in the "data" have changed the unfolded points. Alarmingly, in both cases, the low-x point has been falsely boosted. If the differences in $\gamma^*\gamma$ fragmentation models is ignored, one would incorrectly conclude that $F_2^\gamma(x)$ is starting to rise as x decreases, when clearly the theoretical expectation shows that it should not.

Different $F_2^\gamma(x)$ and Same $\gamma^*\gamma$ Fragmentation

If the same final state is chosen for the "data" and the unfolding Monte Carlo, one can test to see if an F_2^γ used to make the "data" can be reproduced when a different F_2^γ is used in the unfolding Monte Carlo.

Since there is particular interest in the low–x behaviour of F_2^γ , a crucial test of unfolding would be to see if an F_2^γ in the "data" with a steep low–x rise (e.g. LAC1) is resolved when such a rise is not in the unfolding Monte Carlo. Figure 7.3(a) and (b) show unfolded data points in the low and high θ_{tag} regions respectively. The result of the test is that the LAC1 F_2^γ rise at low-x in the low θ_{tag} region cannot be resolved using the GRV F_2^γ as the unfolding Monte Carlo *even when the $\gamma^*\gamma$ fragmentation models are identical.* This is an important result to consider when making a measurement of F_2^γ at low Q^2 . In the high θ_{tag} region the LAC1 F_2^γ rise is clearly resolved, resulting in a good χ^2 comparison to the theoretical expectation.

FD clusters were not used in the calculation of x_{vis}, yet we know that tagged two–photon collisions produce a final state that is peaked in the forward direction. One would hope that including FD clusters into the x_{vis} evaluation would bring the unfolded points nearer to the theoretical expectation in the low θ_{tag} region. The results of Figure 7.3(c) demonstrates that this is not the case. Attention is drawn to the fact that this is despite the x_{vis}/x_{true} correlation coefficient for the unfolding Monte Carlo increasing from 0.70 to 0.81. This result should be noted if one assumes that increasing the x_{vis}/x_{true} correlation coefficient improves the unfolding, as in [80] and [111]. The techniques proposed in these two notes to estimate the invariant mass of the final state are, however, not used in this work. Also, the minimum cluster energy in the FD for the 1990–1992 data is 2

GeV which is higher than the 1 GeV threshold set for later years. Therefore the conclusions drawn from the test of Figure 7.3(c) are likely to be a little pessimistic, but useful in highlighting a potentially serious problem.

It can be seen, by comparing Figure 7.3(a) and (c), that including FD clusters does have the effect of reducing the size of the statistical error estimated by the unfolding on each point. The reduction in the size of the errors should therefore not be taken to mean that the unfolding has produced a more accurate measurement of $F_2^\gamma(x)$.

By comparing Figures 7.3(b) and (d), one sees that including FD clusters has had an adverse effect on reproducing the sharply rising $F_2^\gamma(x)$ well. The bin limits have changed (because the bins are chosen to minimise the bin–to–bin correlations), increasing the theoretical expectation of $F_2^\gamma(x)$ in the smallest x bin. This test supports the previous comment that including FD clusters into the visible x calculation for unfolding does not make the result more accurate. Again, the error bars have decreased, reflecting the improvement in the x_{vis}/x_{true} correlation. The drop in the lowest x bin of Figure 7.3(d) seems to have been compensated for by the rise in value of the second lowest bin. This result may reflect statistical uncertainties in the unfolding and may raise the issue of how well the errors of an unfolded result represent the statistical fluctuations in a data sample. One feature remains clear; the increase of $F_2^\gamma(x)$ in the 'data' sample is still observed in the high θ_{tag} region.

Different $F_2^\gamma(x)$ and Different $\gamma^*\gamma$ Fragmentation

This is the scenario that the experimentalist is faced with when trying to obtain $F_2^\gamma(x)$ from the data. The actual $F_2^\gamma(x)$ is most likely to be different from the one assumed in the Monte Carlo samples generated. Also, the final state in the data is unlikely to be properly modelled by the unfolding Monte Carlo. A test is not done here, since the tests so far have been sufficient to express the problems of unfolding $F_2^\gamma(x)$ from the data.

7.7 Data Unfoldings

In this section the real data are unfolded with four Monte Carlo models:

- GRV($n_f = 4$)[HERWIG] (with the SUE)
- GRV($n_f = 4$)[HERWIG] (without the SUE)
- GRV($n_f = 3$)[F2GEN] (Perimiss 0.1) + $c\bar{c}$ [VERMASEREN]
- GRV($n_f = 3$)[F2GEN] (Point–like) + $c\bar{c}$ [VERMASEREN]

In each case the unfolding is told that the $F_2^\gamma(x)$ used to generate the events was the four–flavour GRV leading order parameterisation, properly constructed in accordance with the GRV publication [11].

This treatment assumes that the charm contribution in the parameterisation correctly describes the charm contribution in the unfolding Monte Carlo sets. This is not actually true because:

1. HERWIG interfaces to PDFLIB [112], which uses the GRV charm distribution from their evolution, rather than the Bethe Heitler contribution that GRV use to construct their F_2^γ with.
2. The charm mass in HERWIG (1.8 GeV) is incompatible with the charm mass in the GRV parameterisation (1.5 GeV). Consequently the charm threshold in HERWIG appears at a lower x than it does in the GRV parameterisation.
3. The charm contribution for the F2GEN unfoldings has been generated by Vermaseren, rather than with F2GEN.

The x_{vis} distributions of the data and the unfolding Monte Carlo models used in the unfoldings for the low and high θ_{tag} regions are shown in Figures 7.4 and 7.5. The data and Monte Carlo events have passed the same selection cuts. The corresponding x_{true} distributions for the unfolding Monte Carlos are also shown in the same figures. The x_{true} distributions are not identical, even though the same $F_2^\gamma(x)$ has been used. This is expected because of the charm problems described above and also because the different final state models have different

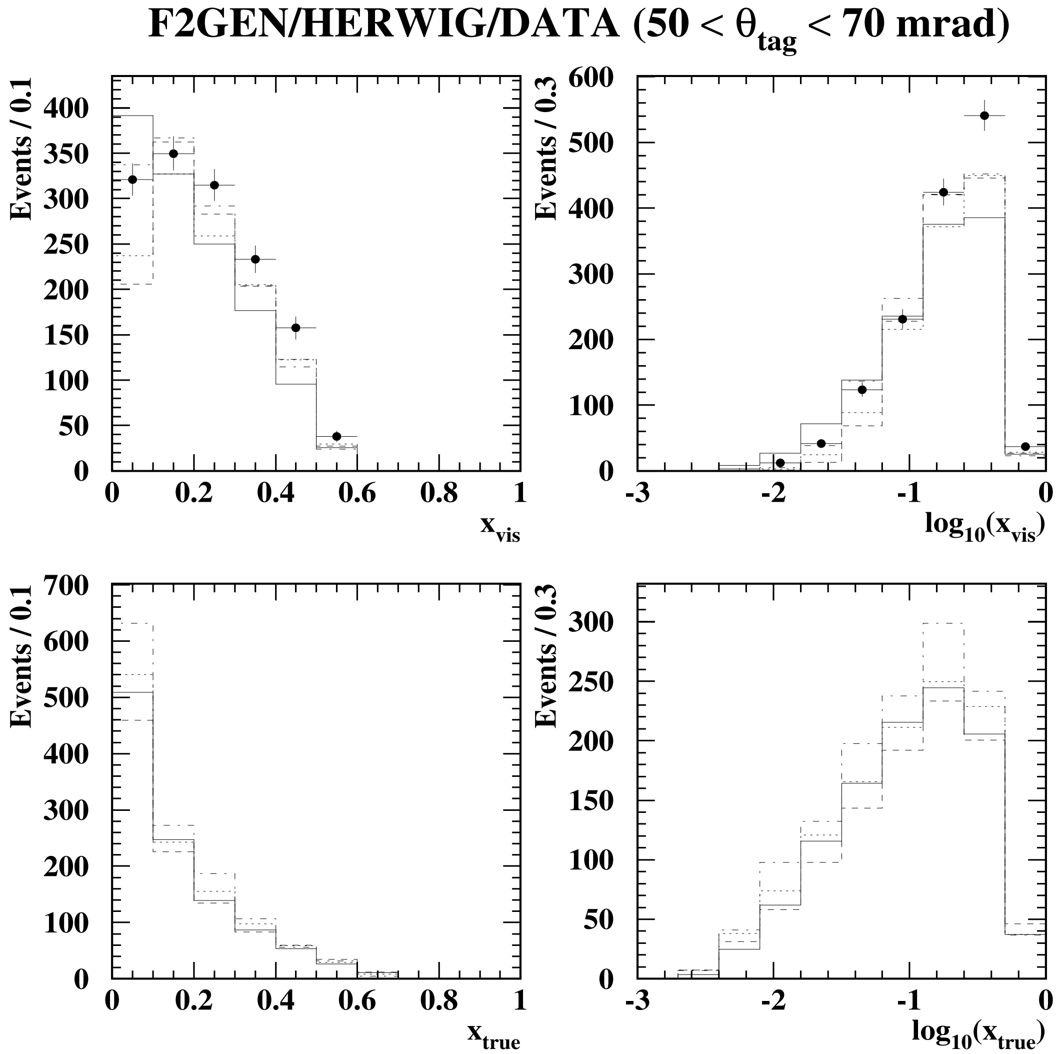

Figure 7.4: x distributions for data and Monte Carlo in the low θ_{tag} region. The data x_{vis} distributions are represented by the dots. The different Monte Carlo samples are from F2GEN GRV 100% point–like (solid line), F2GEN GRV 'perimiss(0.1)' (dashed line), HERWIG GRV without the SUE (dotted line) and HERWIG GRV with the SUE (dot–dashed line).

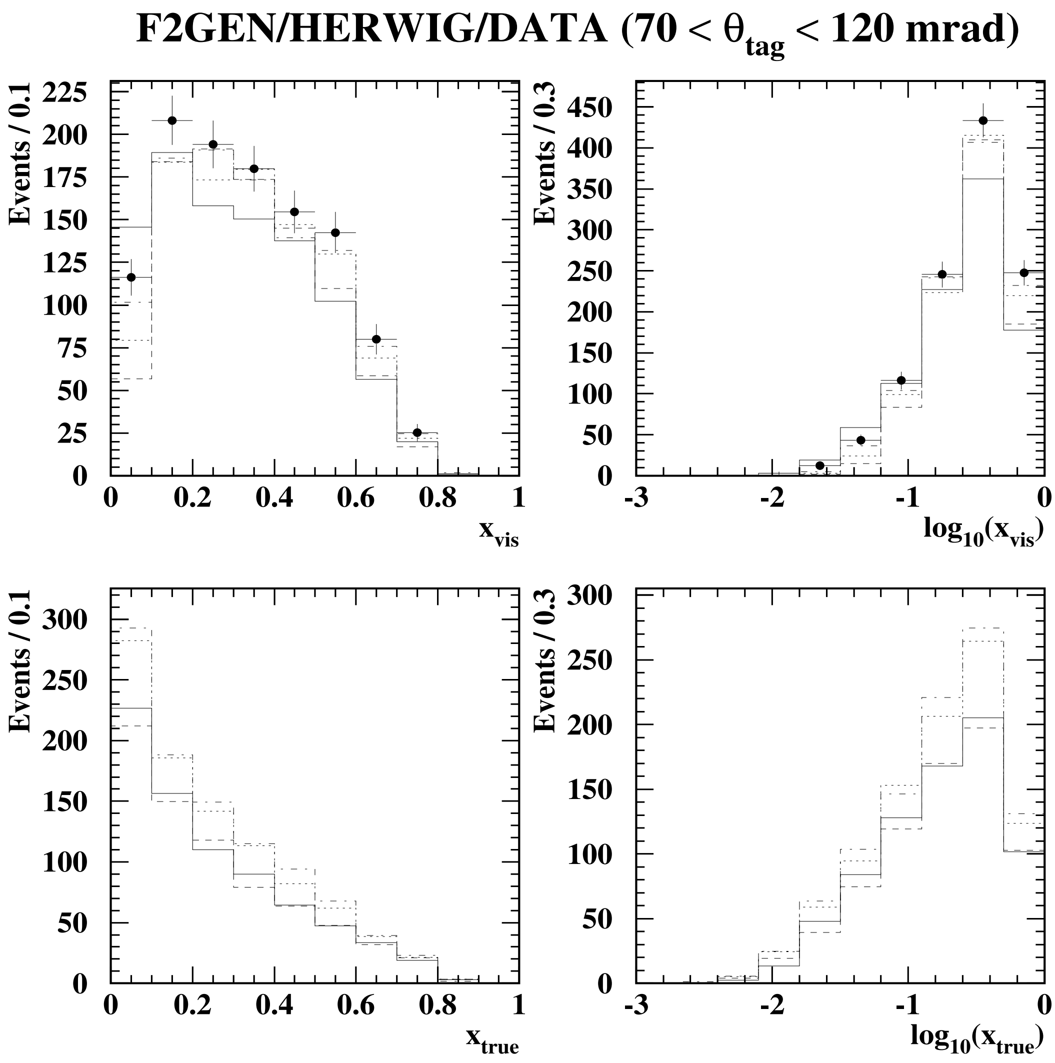

Figure 7.5: x distributions for data and Monte Carlo in the high θ_{tag} region. The data x_{vis} distributions are represented by the dots. The different Monte Carlo samples are from F2GEN GRV 100% point–like (solid line), F2GEN GRV 'perimiss(0.1)' (dashed line), HERWIG GRV without the SUE (dotted line) and HERWIG GRV with the SUE (dot–dashed line).

acceptances, resulting in different numbers of events passing the selection cuts. It is worth noting at this point how extremely similar the x_{true} distributions of the two F2GEN samples (100% point–like and Perimiss 0.1) look and yet how different their x_{vis} distributions are. The x_{vis} distributions show that the unfolded results will be dependent on the Monte Carlo model used for unfolding. The greatest differences between Monte Carlo models and the data appear for $x_{vis} < 0.1$ and this large uncertainty will propagate through to the lower x bins in an unfolded result.

The data unfoldings for the low and high θ_{tag} regions are shown in Figures 7.6 and 7.7 respectively. In each unfolding the x_{vis} distribution of the $\tau^+\tau^-$ background has been subtracted from the data x_{vis} distribution before the unfolding fit takes place. The FD clusters are not used for the calculation of x_{vis}. The bin limits in x are different for each unfolding since they are chosen to minimise the bin–to–bin correlations. On each unfolded result the GRV parameterisation (dashed line) has been overlayed, simply for reference.

The results of the same unfoldings are shown in Table 7.2 (low θ_{tag} region) and 7.3 (high θ_{tag} region). In the tables, the bin limits in x have been fixed, so the F_2^γ values for each bin are not the same as those shown in Figures 7.6 and 7.7, and the bin–to–bin correlations are larger. However, this is useful for comparing results from unfoldings with different $\gamma^*\gamma$ fragmentation models within a given θ_{tag} range.

The combined result for a given θ_{tag} region is constructed from the four unfoldings within that region as follows. The F_2^γ value in one x bin is the mean value of the four F_2^γ values from the same x bin in each unfolding. The combined statistical error is the mean value of the four individual statistical errors. The systematic error due to unfolding with different $\gamma^*\gamma$ fragmentation models is taken to be the r.m.s. of the four F_2^γ values in one x bin.

The combined result for the low θ_{tag} region is illustrated in Figure 7.8 and for the high θ_{tag} region in Figure 7.9.

The inner error bars on each point are statistical only. The outer error bars are the statistical and systematic errors added in quadrature. The GRV (dashed) and LAC1 (dotted) curves have been overlayed for reference.

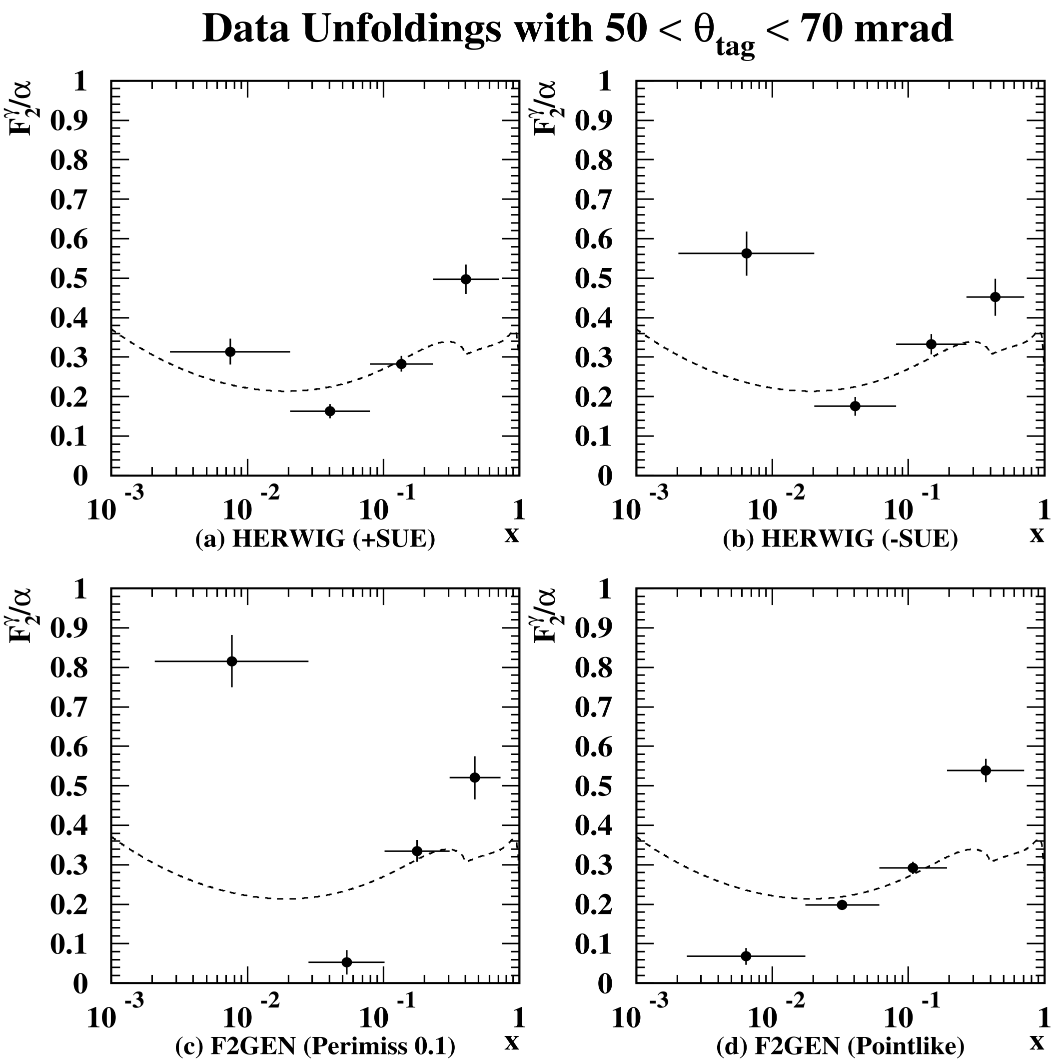

Figure 7.6: Four–flavour unfoldings of the data with different Monte Carlo models in the low θ_{tag} region. The dashed line is the four–flavour GRV parameterisation calculated at $Q^2 = 5.9$ GeV^2, which has been included for reference only.

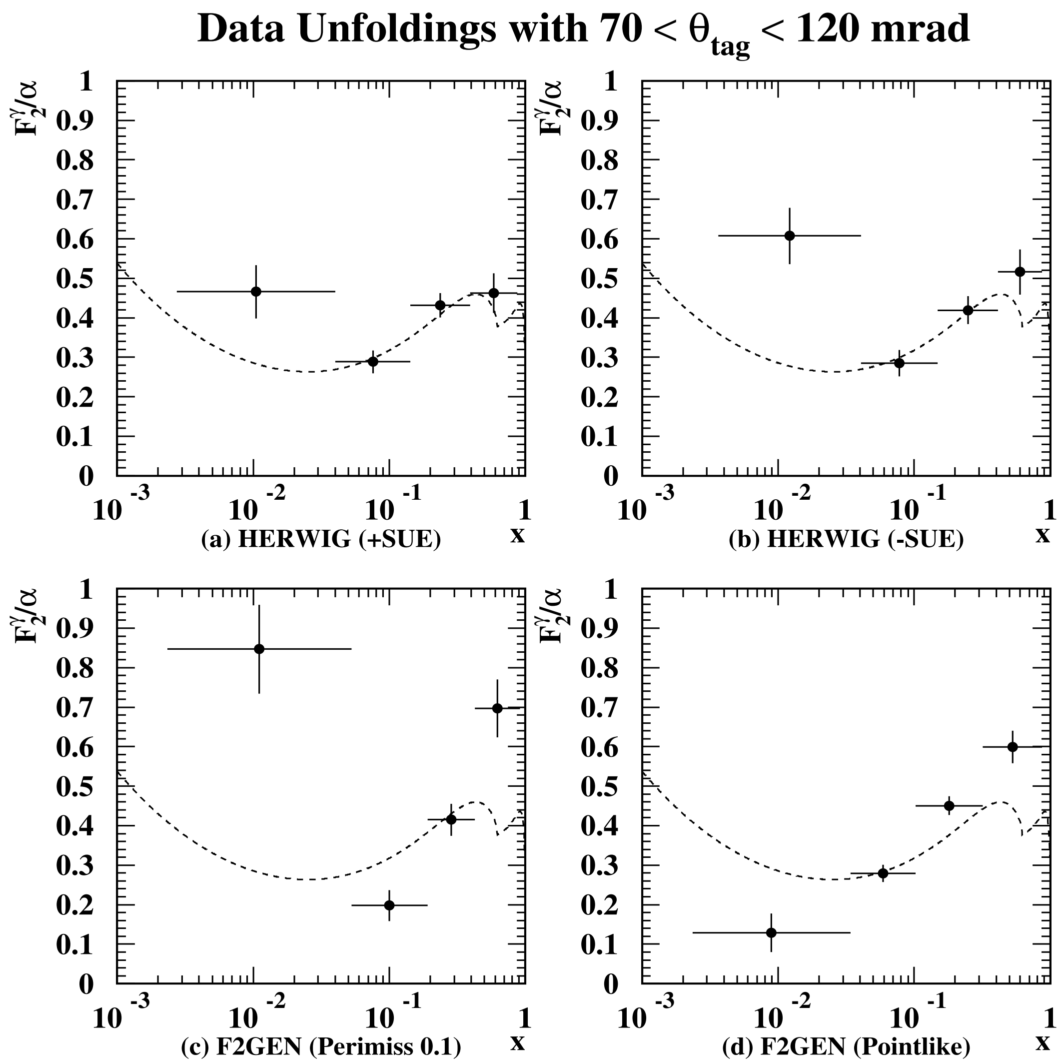

Figure 7.7: Four–flavour unfoldings of the data with different Monte Carlo models in the high θ_{tag} region. The dashed line is the four–flavour GRV parameterisation calculated at $Q^2 = 14.7$ GeV^2, which has been included for reference only.

x range	0.003 – 0.020	0.020 – 0.060	0.060 – 0.200	0.200 – 0.708
F_2^γ/α (+SUE)	0.317 $\pm$ 0.034	0.159 $\pm$ 0.020	0.247 $\pm$ 0.018	0.485 $\pm$ 0.033
F_2^γ/α (-SUE)	0.554 $\pm$ 0.054	0.180 $\pm$ 0.026	0.263 $\pm$ 0.025	0.450 $\pm$ 0.035
F_2^γ/α (Perimiss)	0.886 $\pm$ 0.075	0.146 $\pm$ 0.032	0.142 $\pm$ 0.025	0.508 $\pm$ 0.035
F_2^γ/α (Point–like)	0.076 $\pm$ 0.020	0.204 $\pm$ 0.013	0.294 $\pm$ 0.015	0.543 $\pm$ 0.030
Mean F_2^γ/α	0.458	0.172	0.237	0.497
Mean stat. error	0.046	0.023	0.021	0.033
R.m.s. F_2^γ/α	0.299	0.022	0.057	0.034
Total error	0.303	0.032	0.061	0.047

Table 7.2: Four–flavour unfoldings of the data with different Monte Carlo models in the low θ_{tag} region.

x range	0.003 – 0.030	0.030 – 0.100	0.100 – 0.302	0.302 – 0.871
F_2^γ/α (+SUE)	0.488 $\pm$ 0.076	0.282 $\pm$ 0.030	0.380 $\pm$ 0.029	0.470 $\pm$ 0.038
F_2^γ/α (-SUE)	0.648 $\pm$ 0.080	0.291 $\pm$ 0.035	0.367 $\pm$ 0.032	0.502 $\pm$ 0.041
F_2^γ/α (Perimiss)	0.915 $\pm$ 0.136	0.406 $\pm$ 0.042	0.211 $\pm$ 0.035	0.643 $\pm$ 0.047
F_2^γ/α (Point–like)	0.126 $\pm$ 0.050	0.269 $\pm$ 0.022	0.444 $\pm$ 0.024	0.597 $\pm$ 0.040
Mean F_2^γ/α	0.544	0.312	0.379	0.553
Mean stat. error	0.086	0.032	0.030	0.042
R.m.s. F_2^γ/α	0.286	0.055	0.086	0.070
Total error	0.299	0.064	0.091	0.082

Table 7.3: Four–flavour unfoldings of the data with different Monte Carlo models in the high θ_{tag} region.

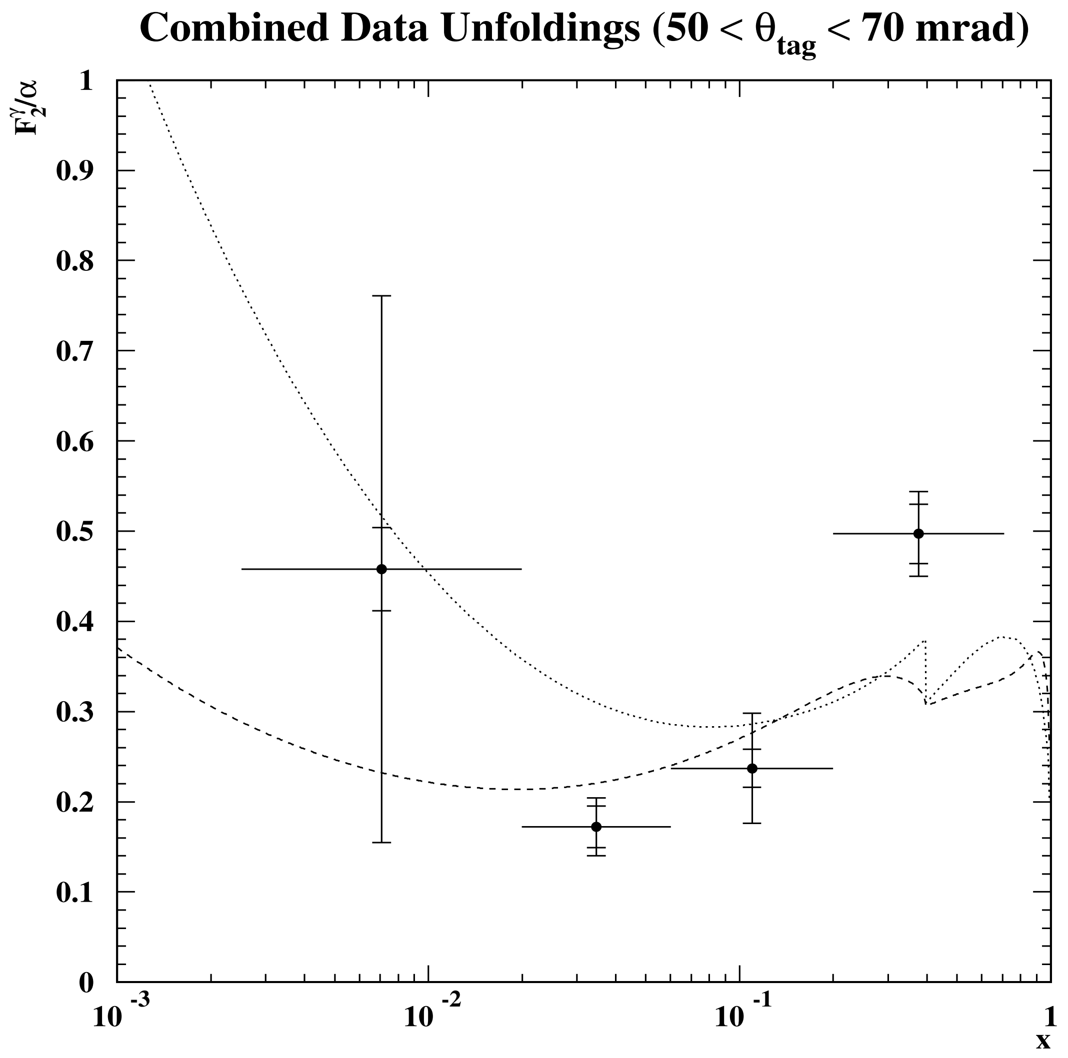

Figure 7.8: Combined four–flavour unfoldings of the data in the low θ_{tag} region. The inner error bars are statistical only. The outer error bars are the statistical and systematic errors combined in quadrature. The broken lines are the four–flavour GRV (dashed) and LAC1 (dotted) parameterisations calculated at $Q^2 = 5.9\ \mathrm{GeV}^2$.

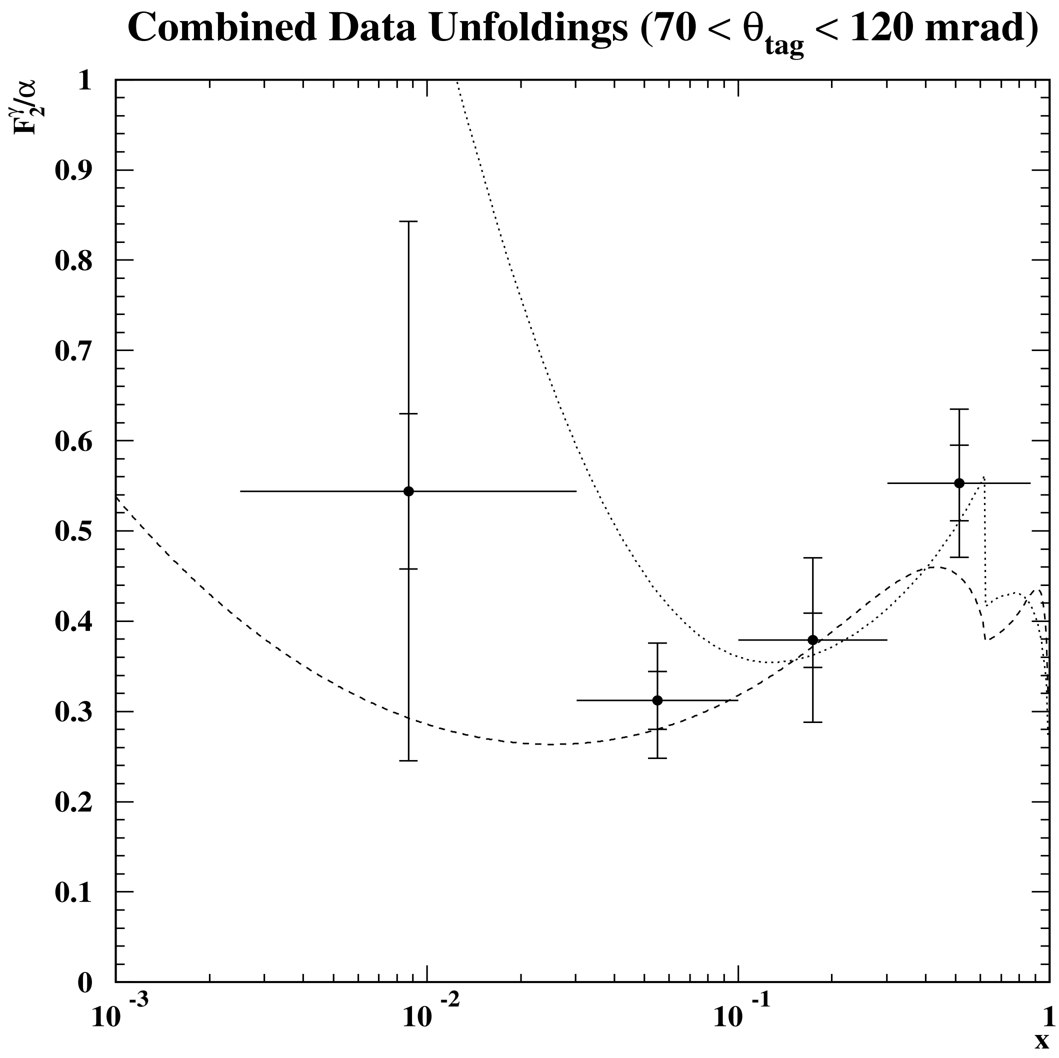

Figure 7.9: Combined four–flavour unfoldings of the data in the high θ_{tag} region. The inner error bars are statistical only. The outer error bars are the statistical and systematic errors combined in quadrature. The broken lines are the four–flavour GRV (dashed) and LAC1 (dotted) parameterisations calculated at $Q^2 = 14.7$ GeV^2.

The combined results are not intended to be final results, as there are many caveats to their presentation, the most important of which are listed here:

- The bin–to–bin correlations are not visible.
- Systematic errors other than from the $\gamma^*\gamma$ fragmentation have not been included. For example, there should be some contribution from variation of charm mass, the minimum E_{tag} cut and the minimum W_{vis} cut.
- The combined result from the low θ_{tag} range should be treated with caution, since the unfolding test of Figure 7.3 demonstrated that a low-x rise could not be observed in the low θ_{tag} region with the present unfolding conditions.

From the combined results it can be seen that unfolding the data with different $\gamma^*\gamma$ fragmentation models contributes significantly to the total error on each unfolded point. In the lowest x point, the variation of the $\gamma^*\gamma$ fragmentation models is the dominant source of error and one that cannot be neglected. With the present data sample and $\gamma^*\gamma$ fragmentation models, it is difficult to make a strong statement on the low-x behaviour of $F_2^\gamma(x)$.

The final unfolded results have been compared to published unfolded results from LEP in Figures 7.10–7.12. A number of points must be noted for this comparison:

- The published OPAL [34] and DELPHI [36] results, shown in Figures 7.10 and 7.11, have been unfolded using linear x as the unfolding variable, rather than $\log_{10} x$ as used in this thesis. The benefit of using $\log_{10} x$ as the unfolding variable is that it divides the lowest linear x data point up into approximately two points. The published OPAL [35] and DELPHI [36] results in Figure 7.12 have been unfolded to emphasise the low-x region.
- The published results are three–flavour unfoldings, but the results from this thesis are four–flavour unfoldings. Hence, for a fair comparison of results, each data point of the published three–flavour results has had an estimate of the charm contribution added to it. This has been done by calculating the average charm contribution for each x bin, using Equation 2.22 with $m_c = 1.5$ GeV and the mean Q^2 value of the published unfolded result.
- The published results do not account for the various $\gamma^*\gamma$ fragmentation schemes in the calculation of their systematic error. This is apparent from

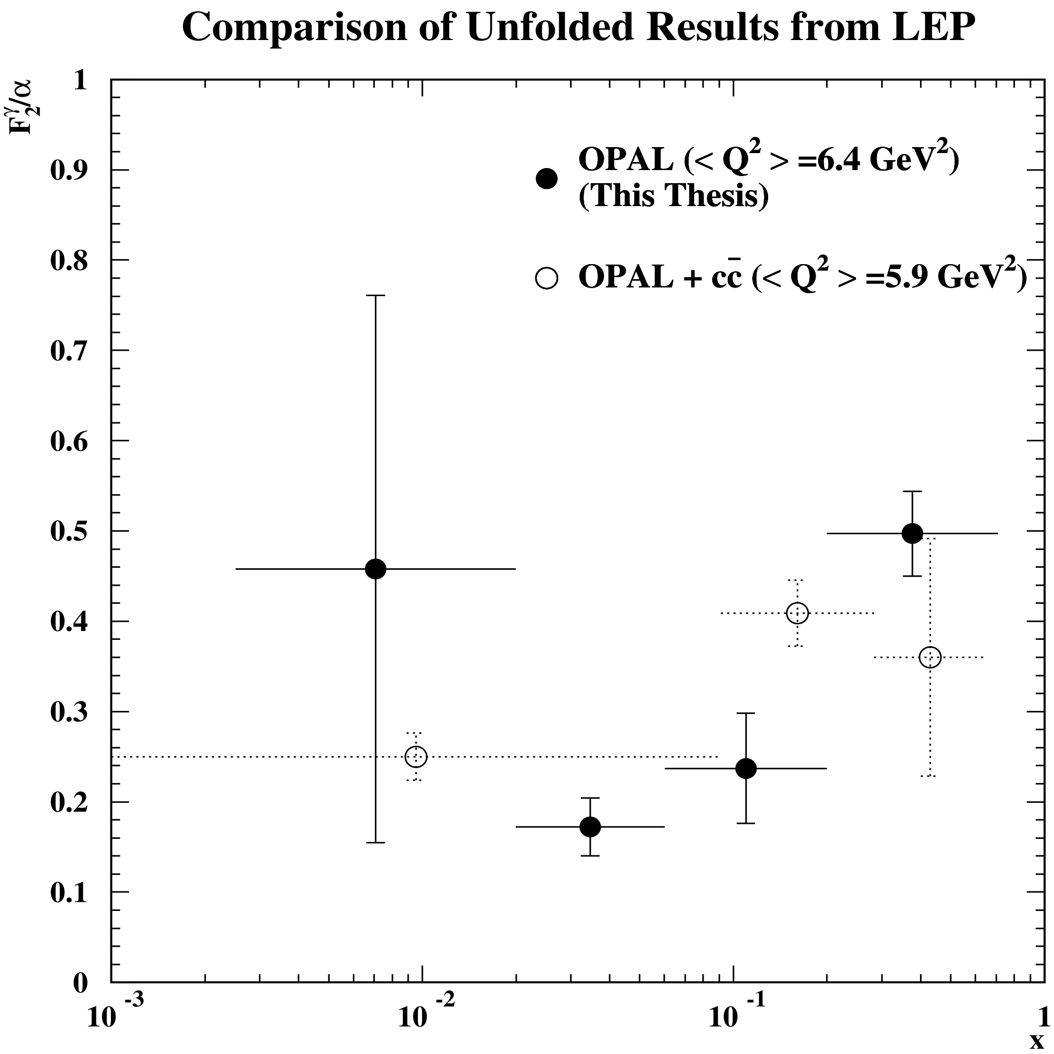

Figure 7.10: Comparison in the low Q^2 region of the combined four–flavour result of this thesis, unfolded on a $\log_{10} x$ scale, with the three–flavour OPAL [34] result (with an estimate of the charm contribution added) unfolded on a linear x scale.

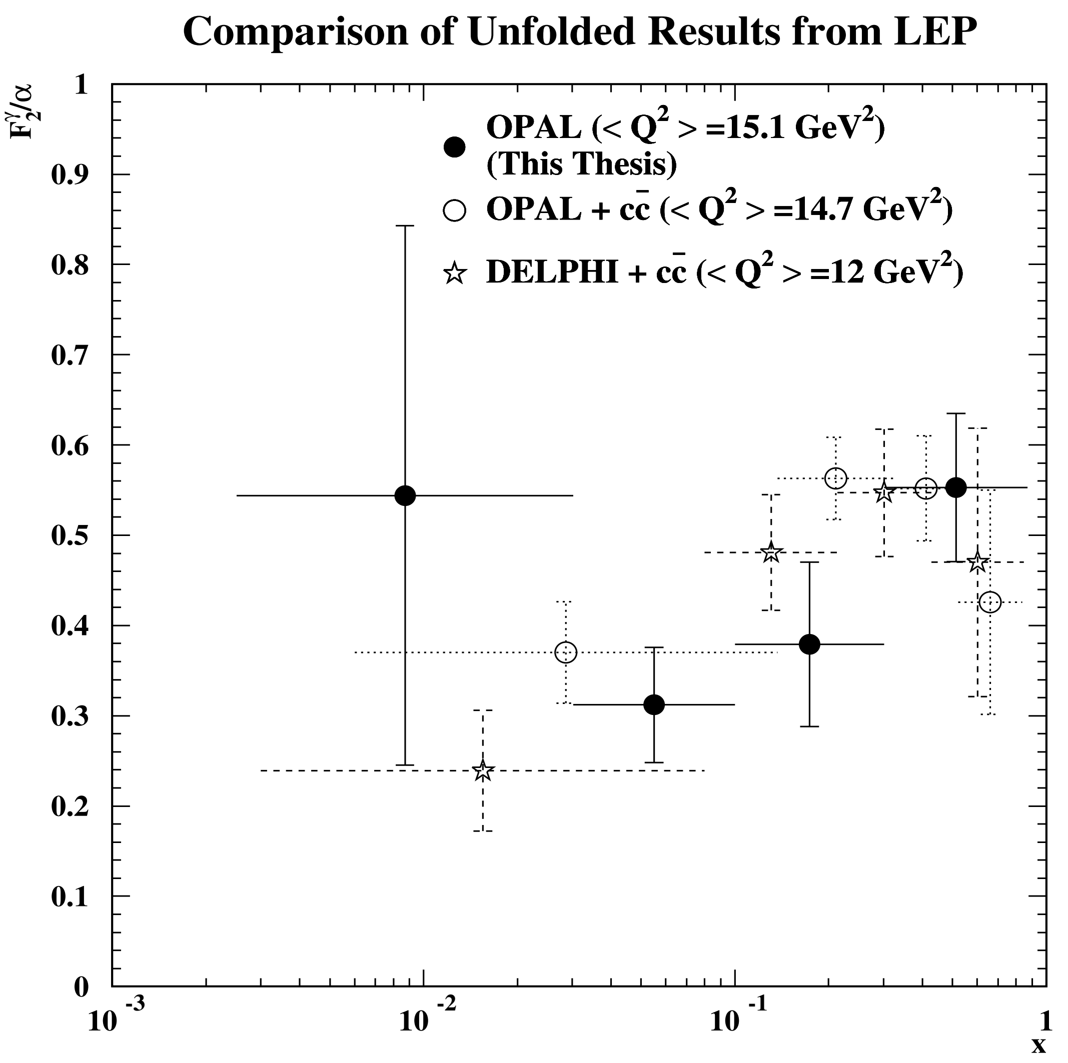

Figure 7.11: Comparison in the high Q^2 region of the combined four–flavour result of this thesis, unfolded on a $\log_{10} x$ scale, with three–flavour OPAL [34] and DELPHI [36] results (with an estimate of the charm contribution added) unfolded on a linear x scale.

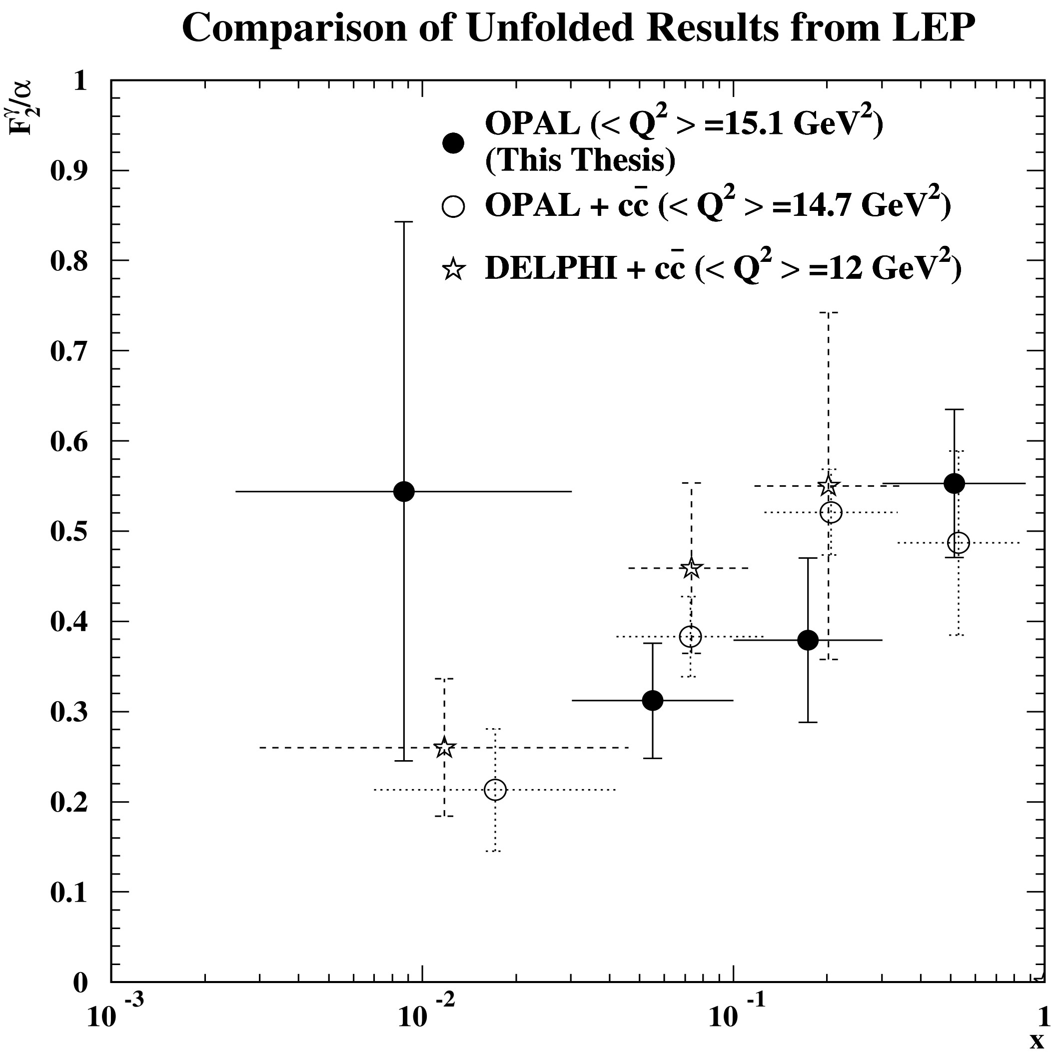

Figure 7.12: Comparison in the high Q^2 region of the combined four–flavour result of this thesis, unfolded on a $\log_{10} x$ scale, with the three–flavour low–x emphasis results of OPAL[35] and DELPHI [36] (with an estimate of the charm contribution added).

the small error bars on the lowest x points. All of the error bars give the statistical and systematic errors added in quadrature.

It is critical for future measurements that try to determine the low-x behaviour of the photon structure function to include in the systematic error the effect of using different $\gamma^*\gamma$ fragmentation models in the unfolding. Secondly, if the error from this effect is to be reduced, attention must be paid to improving the Monte Carlo modelling of the $\gamma^*\gamma$ fragmentation process.

Chapter 8

Summary and Conclusions

This thesis began with an introduction to photon structure and how the photon structure function can be determined from singly–tagged two–photon collisions at an e^+e^- collider.

In the theoretical presentation of $F_2^\gamma(x, Q^2)$ in Chapter 2, it became clear that the interesting region is at low Bjorken-x, where the differences between $F_2^\gamma(x)$ parameterisations differ the most and where the proton structure function is known to start rising. The present set of $F_2^\gamma(x, Q^2)$ parameterisations and models was reviewed and illustrated.

In Chapter 3 a brief description of LEP was given, followed by a more detailed account of the OPAL detector. Emphasis was placed on the Forward Detector where the two–photon collisions were tagged.

Chapter 4 presented the selection of tagged two-photon events. A comparison of the 1990/1991/1992 data showed that the data are self consistent. Backgrounds in the selected sample are small.

The Monte Carlo simulation of tagged two–photon events by F2GEN, HERWIG and Vermaseren was discussed in Chapter 5. A comparison of Vermaseren with F2GEN and F2GEN with HERWIG showed that the cross–sections of the generators are in good agreement.

Chapter 6 looked at the comparison of data and Monte Carlo and Chapter 7 was a study of unfolding. The following conclusions can be drawn from these two chapters:

- The visible cross–section and all final state distributions of the tagged two–photon process are influenced by both the photon structure function and the complete process by which particles are produced from the two–photon collision (the '$\gamma^*\gamma$ fragmentation'). Therefore, any analysis to extract F_2^γ must study the final state as well.

- Unfolding with a Monte Carlo that has not correctly modelled the $\gamma^*\gamma$ fragmentation (i.e. the unfolding Monte Carlo has a different x_{vis}/x_{true} relationship than the data) will result in an unfolded $F_2^\gamma(x)$ that is biased towards lower or higher x.

- The track energy flow distributions (Figures 6.16(d) and 6.17(d)) show features that differ between the Monte Carlo models and the data in the OPAL central detector acceptance, indicating that all of these models provide an inadequate description of the $\gamma^*\gamma$ fragmentation process. Conversely, the same distribution can be used to tune up the $\gamma^*\gamma$ fragmentation of the Monte Carlo models.

- Mis–modelling of the $\gamma^*\gamma$ fragmentation process in an unfolding Monte Carlo is at present a large source of error in an unfolded F_2^γ result, especially at low-x.

- Even with the correct $\gamma^*\gamma$ fragmentation model, in the low Q^2 region it has been demonstrated that the unfolding procedure does not correctly recover a known $F_2^\gamma(x)$ from a mock data set when when using a different $F_2^\gamma(x)$ to unfold with. This remains an outstanding problem.

These conclusions should be accounted for when interpreting the presently available unfolded $F_2^\gamma(x)$ data and when making a new measurement of $F_2^\gamma(x)$.

Bibliography

[1] K. Ahmet et al., OPAL Coll., Nucl. Instr. and Meth. **A305** (1991) 275.

[2] European Committee for Future Accelerators. 'General Meeting on LEP', CERN Publications Group, 1981.

[3] G. A. Schuler and T. Sjöstrand, *Proceedings of the Workshop on Two–Photon Physics from DAΦNE to LEP200 and Beyond*, College de France, Paris, February 2–4 1994, eds. F. Kapusta and J. Parisi, World Scientific (Singapore) 1994, p163.

[4] L. N. Hand, Phys. Rev. **129** (1963) 1834.

[5] Ch. Berger and W. Wagner, Phys. Rep. **146** (1987) 1.

[6] R. Akers et al., OPAL Coll., Z. Phys. **C60** (1993) 593.

[7] H.-J.Behrend et al., CELLO Coll., Phys. Lett. **B126**, (1983) 384.

[8] *Proceedings of PHOTON '95*, Sheffield, England, 8–13 April 1995, eds. B. Cartwright, D. J. Miller and V. A. Khoze.

[9] C. Peterson, T. F. Walsh and P. M. Zerwas, Nucl. Phys. **B229** (1983) 301.

[10] A. Cordier and P. M. Zerwas, *Proceedings of the ECFA Workshop on LEP200*, Aachen, Germany, Vol. 1, eds. A. Böhm and W. Hoogland, CERN 87-08, p242.

[11] M. Glück, E. Reya and A. Vogt, Phys. Rev. **D46** (1992) 1973.

[12] J. R. Forshaw and P. N. Harriman, Phys. Rev. **D46** (1992) 3778.

[13] J. H. Da Luz Vieira and J. K. Storrow, Z. Phys. **C51** (1991) 241.

[14] E. A. Kuraev, L. N. Lipatov, and V. S. Fadin, Phys Lett **60B** (1975) 50.

[15] Ya. Ya. Balitskij and L. N. Lipatov, Sov. J. Nucl. Phys. **28** (1978) 822.

[16] G. Altarelli and G. Parisi, Nucl. Phys. **B126** (1977) 298.

[17] Yu. L. Dokshitzer, Sov. Phys. JETP **46** (1977) 641.

[18] L. N. Lipatov, Sov. J. Nucl. Phys. **20** (1975) 95.

[19] V. N. Gribov and L. N. Lipatov, Sov. J. Nucl. Phys. **15** (1972) 438.

[20] G. Altarelli, Phys. Rep. **81** (1982) 1.

[21] M. Derrick et al., ZEUS Coll., DESY–95–193, submitted to Z. Phys. C., Phys Lett **B316** (1993) 412.

[22] I. Abt et al., H1 Coll., Nucl. Phys. **B407** (1993) 515.

[23] D. J. Miller, B. W. Kennedy, J. J. Ward and J. R. Forshaw, "Deep Inelastic $e\gamma$ Scattering with Beamsstrahlung", *Proceedings of the Workshop on Physics and Experiments at Linear Colliders*, Waikoloa, Hawaii, 26–30 April 1993, ed. Harris, Olsen, Pakvasa and Tata, World Scientific.

[24] Ch. Berger et al., PLUTO Coll., Phys. Lett. **B142** (1984) 111.

[25] Ch. Berger et al., PLUTO Coll., Nucl. Phys. **B281** (1987) 365.

[26] M. Althoff et al., TASSO Coll., Z. Phys. **C31** (1986) 527.

[27] W. Bartel et al., JADE Coll., Z. Phys. **C24**, (1984) 231.

[28] H. Aihara et al., TPC/2γ Coll., Z. Phys. **C34**, (1987) 1.

[29] J. S. Steinman et al., TPC/2γ Coll., UCLA preprint, UCLA–HEP–88–004 (1988).

[30] T. Sasaki et al., AMY Coll., Phys. Lett. **B252**, (1990) 491.

[31] K. Muramatsu et al., TOPAZ Coll., Phys. Lett. **B332**, (1994) 477.

[32] D. J. Miller, "Gamma–gamma Topics and a look at Mesonic Goo", *XVI International Symposium on Lepton and Photon Interactions*, Ithaca, NY, August 1993, eds. P. Drell and D. Rubin, AIP Press 1994; Text submitted to the reviewer.

[33] M. H. Lehto, "A Measurement of the Photon Structure Function $F_2(x)$", Ph.D. Thesis, University College London, 1993.

[34] R. Akers et al., OPAL Coll., Z. Phys. **C61** (1994) 199.

[35] J. J. Ward (for the OPAL Coll.), "Unfolding of the Photon Structure Function F_2^γ with Special Attention to the Low-x Region", *Proceedings of the Workshop on Two–Photon Physics from DAΦNE to LEP200 and Beyond*, College de France, Paris, February 2–4 1994, eds. F. Kapusta and J. Parisi, World Scientific (Singapore) 1994; OPAL internal publication (PN116), February 1994.

[36] P. Abreu et al., DELPHI Coll., Z. Phys. **C69** (1996) 223.

[37] L. E. Gordon and J. K. Storrow, Z. Phys. **C56** (1992) 307.

[38] R. Brandelik et al., TASSO Coll., Phys. Lett. **B107** (1981) 290.

[39] T. H. Bauer, F. M. Pipkin, R. D. Spital and D. R. Yennie, Rev. Mod. Phys. **50** (1978) 261.

[40] J. Badier et al., NA3 Coll., Z. Phys. **C18** (1983) 281.

[41] C. T. Hill and G. G. Ross, Nucl. Phys. **B148** (1979) 373.

[42] R. L. Kingsley, Nucl. Phys. **B60** (1973) 45.

[43] E. Witten, Nucl. Phys. **B120** (1977) 189.

[44] W. A. Bardeen and A. J. Buras, Phys. Rev. **D20** (1979) 166.

[45] R. J. De Witt et al., Phys. Rev. **D19** (1979) 2046.

[46] C. H. Lewellyn–Smith, Phys. Lett. **B79** (1978) 83.

[47] W. R. Frazer and J. F. Gunion, Phys. Rev. **D20** (1979) 147.

[48] J. H. Field, F. Kapusta and L. Poggioli, Phys. Lett. **B181** (1986) 362.

[49] J. H. Field, F. Kapusta and L. Poggioli, Z. Phys. **C36** (1987) 121.

[50] B. R. Webber, "Hadron Production and Structure at Small Distances" *Techniques and Concepts of High Energy Physics VIII*, ed. T. Ferbel, NATO ASI Series B: Physics Vol. 351, Plenum Press 1995.

[51] A. H. Mueller, Nucl. Phys. **B415** (1994) 373.

[52] M. Glück, E. Hoffmann and E. Reya, Z. Phys. **C13** (1982) 119.

[53] E. Laenen, S. Riemersma, J. Smith and W. L. van Neervan, Stony Brook preprint, ITP–SB–93–1 (1993); ITP–SB–93–46 (1993).

[54] K. Hagiwara, M. Tanaka, I. Watanabe and T. Izubuchi, Phys. Rev. **D51** (1995) 3197.

[55] V. Budnev et al., Phys. Rep. **C15** (1975) 182.

[56] E. Gotsman, A. Levy and U. Maor, Z. Phys. **C40** (1988) 117.

[57] M. Glück, E. Reya and A. Vogt, Z. Phys. **C53** (1992) 127.

[58] M. Glück, E. Reya and A. Vogt, Z. Phys. **C53** (1992) 651.

[59] J. F. Field, *Proceedings of the VIII Int. Workshop on Photon–Photon Collisions*, Shoresh, Isreal, 1988, U. Karsdon (ed.) p.349 (World Scientific, 1988).

[60] W. Bartel et al., JADE Coll., Phys. Lett. **B121**, (1983) 203.

[61] J. F. Owens and E. Reya, Phys. Rev. **D17** (1978) 3003.

[62] M. Drees and K. Grassie, Z. Phys. **C28** (1985) 451.

[63] M. Glück and E. Reya, Phys. Rev. **D28** (1983) 2749.

[64] Ch. Berger, Intern. Symp. on Lepton and Photon Interactions at High Energy (Cornell University, Ithaka, NY, 1983).

[65] H. Abramowicz, K. Charchula, and A. Levy, Phys. Lett. **B269** (1991) 458.

[66] A. Vogt, *Proceedings of the Workshop on Two–Photon Physics at LEP and HERA*, Lund, May 26–28 1994, eds. G. Jarlskog and L. Jönsson, Lund University 1994, p141.

[67] P. Aurenche et al., Z. Phys. **C56** (1992) 589.

[68] P. Aurenche et al., Phys. Lett. **B233** (1989) 517.

[69] M. Glück et al., Phys. Rev. **D30** (1984) 1447.

[70] F. Kapusta, Z. Phys. **C42** (1989) 225.

[71] G. A. Schuler and T. Sjöstrand, Z. Phys. **C68** (1995) 607.

[72] D. C. Imrie et al., Nucl. Instr. and Meth. **A238** (1989) 515.

[73] B. E. Anderson et al., Nucl. Instr. and Meth. **A238** (1989) 650.

[74] P. R. Hobson and J. J. Ward, "Using the Electromagnetic Clusters from the Gamma Catcher", OPAL internal publication (TN254), September 1994.

[75] M. Z. Akrawy et al., OPAL Coll., "The Trigger System of the OPAL Experiment at LEP", CERN-PPE/91-32.

[76] S. Weisz et al., "ROPE Users' Guide", OPAL internal publication.

[77] G. Hanson et al., "OPAL User's guide for the SHIFT project", OPAL internal publication.

[78] A. Buijs, "Management of Analysis on Workstations", OPAL internal publication.

[79] A. M. Lee (IV), "Anatomy of a Mawsel", OPAL internal publication.

[80] J. A. Lauber, "Using FD to Measure Hadronic Energy in the Forward Region", OPAL internal publication (TN348), February 1996.

[81] S. Jadach et al., CERN–TH 7075/93.

[82] R. Akers et al., OPAL Coll., Z. Phys. **C61** (1994) 19.

[83] J. Hilgart, R. Kleiss and F. Le Diberder, Comp. Phys. Commun. **75** (1993) 191.

[84] C. Peterson, T. F. Walsh and P. M. Zerwas, Nucl. Phys. **B174** (1980) 424.

[85] B. W. Kennedy, "Radiative backgrounds to the tagged two–photon process $\gamma\gamma \rightarrow$ hadrons", OPAL internal publication (TN164), May 1993.

[86] G. Alexander et al., OPAL Coll., Z. Phys. **C52** (1991) 175.

[87] P. Acton et al., OPAL Coll., Z. Phys. **C58** (1993) 219.

[88] J. Allison et al., Nucl. Instr. and Meth. **A317** (1992) 47.

[89] R. Bhattacharya, G. Grammer Jr. and J. Smith, Phys. Rev. **D15**, (1977) 3267.

[90] G. Grammer Jr., J. Smith, and J. A. M. Vermaseren, Phys. Rev. **D15**, (1977) 3280.

[91] G. Grammer Jr., J. Smith, and J. A. M. Vermaseren, Phys. Rev. **D19**, (1979) 137.

[92] A. Buijs, W. G. J. Langeveld, M. H. Lehto and D. J. Miller, Comp. Phys. Commun. **79** (1994) 523.

[93] HERWIG 5.8; G. Marchesini et al., Comp. Phys. Commun. **67** (1992) 465.

[94] W. G. J. Langeveld, "Pion and Kaon Pair–Production in Photon–Photon Collisions", Ph.D. Thesis, University of Utrecht, 1985.

[95] G. Bonneau, M. Gourdin and F. Martin, Nucl. Phys. **B54** (1973) 573.

[96] J. H. Field, Nucl. Phys. **B168** (1980) 477; Nucl. Phys. **B176** (1980) 545 (E).

[97] H. Kolanoski, "Two Photon Physics at e^+e^- Storage Rings", Springer–Verlag, Berlin (1984).

[98] S. J. Brodsky, T. Kinoshita and H. Terazawa, Phys. Rev. **D4** (1971) 1532.

[99] M. Bengtsson and T. Sjöstrand, Phys. Lett. **B185** (1987) 435; Nucl. Phys. **B289** (1987) 810.

[100] T. Sjöstrand, Comp. Phys. Commun. **47** (1987) 347.

[101] M. Bengtsson and T. Sjöstrand, Comp. Phys. Commun. **43** (1987) 357.

[102] G. Marchesini and B.R. Webber, Nucl. Phys. **B238** (1984) 1.

[103] G. Marchesini and B.R. Webber, Nucl. Phys. **B310** (1988) 461.

[104] B. R. Webber, Nucl. Phys. **B238** (1984) 492.

[105] G. Marchesini and B.R. Webber, Phys. Rev. **D38** (1988) 3419.

[106] M. H. Seymour, *Proceedings of the Workshop on Two–Photon Physics at LEP and HERA*, Lund, May 26–28 1994, eds. G. Jarlskog and L. Jönsson, Lund University 1994, p215; LU-TP-94/11 (1994).

[107] P. Kessler, *Proceedings of the Workshop on Two–Photon Physics at LEP and HERA*, Lund, May 26–28 1994, eds. G. Jarlskog and L. Jönsson, Lund University 1994, p183.

[108] T. Sjöstrand, Phys. Lett. **B157** (1985) 321.

[109] V. Blobel, *Proceedings of the CERN School of Computing* Aiguablava, Spain, September 1984, CERN 85-09, ed. C. Verkerk, (1985).

[110] G. D. Lafferty and T. R. Wyatt, Nucl. Instr. and Meth. **A355** (1995) 541.

[111] B. W. Kennedy, "Use of a Neural Network to Estimate the Hadronic Invariant Mass in Two–Photon Interactions", OPAL internal publication (TN355), February 1996.

[112] H. Plothow-Besch, Comp. Phys. Commun. **75** (1993) 396.